Springer Theses
Recognizing Outstanding Ph.D. Research

Yu-Pin Lin

Isotropic and Anisotropic Seismic Tomography Using Active Source and Earthquake Records

Springer

Springer Theses

Recognizing Outstanding Ph.D. Research

Aims and Scope

The series "Springer Theses" brings together a selection of the very best Ph.D. theses from around the world and across the physical sciences. Nominated and endorsed by two recognized specialists, each published volume has been selected for its scientific excellence and the high impact of its contents for the pertinent field of research. For greater accessibility to non-specialists, the published versions include an extended introduction, as well as a foreword by the student's supervisor explaining the special relevance of the work for the field. As a whole, the series will provide a valuable resource both for newcomers to the research fields described, and for other scientists seeking detailed background information on special questions. Finally, it provides an accredited documentation of the valuable contributions made by today's younger generation of scientists.

Theses are accepted into the series by invited nomination only and must fulfill all of the following criteria

- They must be written in good English.
- The topic should fall within the confines of Chemistry, Physics, Earth Sciences, Engineering and related interdisciplinary fields such as Materials, Nanoscience, Chemical Engineering, Complex Systems and Biophysics.
- The work reported in the thesis must represent a significant scientific advance.
- If the thesis includes previously published material, permission to reproduce this must be gained from the respective copyright holder.
- They must have been examined and passed during the 12 months prior to nomination.
- Each thesis should include a foreword by the supervisor outlining the significance of its content.
- The theses should have a clearly defined structure including an introduction accessible to scientists not expert in that particular field.

More information about this series at http://www.springer.com/series/8790

Yu-Pin Lin

Isotropic and Anisotropic Seismic Tomography Using Active Source and Earthquake Records

Doctoral Thesis accepted by
National Taiwan University, Taipei, Taiwan

Springer

Author
Dr. Yu-Pin Lin
Department of Earth Sciences, Southern California Earthquake Center
University of Southern California
Los Angeles, CA
USA

Supervisors
Prof. Li Zhao
Institute of Earth Sciences
Academia Sinica
Taipei
Taiwan

Prof. Shu-Huei Hung
Department of Geosciences
National Taiwan University
Taipei
Taiwan

ISSN 2190-5053 ISSN 2190-5061 (electronic)
Springer Theses
ISBN 978-981-10-5067-1 ISBN 978-981-10-5068-8 (eBook)
DOI 10.1007/978-981-10-5068-8

Library of Congress Control Number: 2017943094

Printed on acid-free paper

This Springer imprint is published by Springer Nature
The registered company is Springer Nature Singapore Pte Ltd.
The registered company address is: 152 Beach Road, #21-01/04 Gateway East, Singapore 189721, Singapore

Supervisor's Foreword

One of the major goals of seismology is to gain knowledge on the internal structures of the Earth from seismic signals recorded by instruments deployed on the surface of the globe. Ever since the introduction of digital seismometers in the late 1970s, a huge amount of data has been collected which, with the availability of increasingly powerful and affordable computers, has led to the creation of numerous tomography models, allowing us to peek into the Earth's global, regional and local structures. In keeping with the improvement in seismic tomography models, our perception of the Earth's internal constitution and dynamics has been constantly shaped and reshaped.

However, at the same time we have also seen attempts that are little more than straightforward applications of an established method to a more or less the same old dataset (sometimes with additions of a number of earthquakes and/or stations). The outcome of this practice is a simple accumulation of models for the same region with little discernible advance in science. Take Taiwan as an example: an incomplete search of literature in the past two decades yields at least eight different tomography models covering roughly the same area of Taiwan and its immediate surroundings. They share some common large-scale features, but have drastic differences in details. This situation is by no means unique to Taiwan. As "new" models are created, there has clearly been a lack of (1) rigorous, objective and quantitative assessments on the validity of the models and (2) exploration of new techniques to qualitatively improve the robustness of tomography models. The research presented in this thesis represents two efforts in those two aspects.

The first part of this thesis (Chaps. 2 and 3) describes the research in which a dataset of the first (P-wave) arrival times from active sources were used to make quantitative assessments of existing tomography models for Taiwan. These P-wave arrival times are regarded as "ground truth" because they are from active sources (explosions) whose locations and origin times are exactly known. Through tedious manual picking from waveforms recorded at nearly 1400 sites all over Taiwan, the author acquired more than 6000 P-wave arrival times, which were then compared with predictions by existing tomography models to evaluate the performance of the models. Indeed, different levels of performance can be seen not only in different

tomography models but also in different parts of the same model. This "ground truth" dataset was also used to conduct a tomography study for the shallow crustal structure in Taiwan. The resulting model (presented in Chap. 3) has much lower residual and good correlation with surface geology. It was nevertheless turned down for publication at an international journal due to the objection by an anonymous but "well-known expert in active-source seismology". Shunryu Suzuki, founder of the San Francisco Zen Center, once wrote, "In the beginner's mind there are many possibilities, in the expert's mind there are few".

The second part of this thesis (Chaps. 4 and 5) deals with the development and application of a new, full-wave approach to imaging the three-dimensional anisotropic structures using the widely available shear-wave splitting measurements. Traditional modelling and interpretation of shear-wave splitting in terms of anisotropy have been largely based on ray theory which presumes a uniform distribution of anisotropy. The full-wave approach based on normal-mode theory developed here leads to spatially varying sensitivities of shear-wave splitting on anisotropic structures. The application of this approach to data collected at a seismic network in Southern California, coupled with a multi-scale inversion practice, demonstrates that this new approach is very effective in imaging the three-dimensional variations of anisotropy, which in turn provides strong seismic constraints on the state of stress and strain in the lithosphere and the dynamics of the mantle flow in the asthenosphere.

At the present time, full-wave seismic tomography is one of the most active research frontiers in seismology. Another new generation of Earth models are being created offering new insights into the inner workings of our planet. I am confident that the author of this thesis has much to contribute in her future endeavours.

Taipei, Taiwan Li Zhao
February 2017

Abstract

This thesis involves two regional seismic tomography studies: One for the isotropic P-wave velocity in the upper crust beneath Taiwan using first-arrival times from active sources; the other for the shear-wave anisotropy structure under Southern California using SKS splitting intensity measurements. In the isotropic tomography for Taiwan, we use waveform records from the 10 explosions in 2008 conducted by the TAiwan Integrated GEodynamics Research (TAIGER) project. A large dataset of high-quality ground-truth first-arrival times are hand-picked from the active-source records at $\sim$1400 sites throughout Taiwan, which greatly enhance our capability to determine the crustal velocity beneath Taiwan with unprecedented accuracy and resolution, especially along the two north-south and two east-west island-wide linear transects with densely deployed receivers. At first, these first-arrival times are used to evaluate the existing tomography models for Taiwan. Results show that tomography models obtained from traditional travel time inversions provide consistent and qualitatively correct locations of larger-scale velocity perturbations. However, small-scale features are inconsistent among different models, and their velocity perturbations are mostly underestimated. Then we use our ground-truth first-arrival times to refine the P-wave velocity model. With a trial-and-error procedure, we acquire the best 2D models along a number of shot-to-station profiles by fitting the first-arrival times. Finally a partition modelling approach is employed to invert for a 3D model in northern Taiwan based on a collection of the crisscrossing 2D models that densely transect across the region. The resulting structural variations in our 3D model correlate remarkably well with the surface geological features that are distinctly shaped by the orogenic and tectonic history in Taiwan.

In the anisotropic tomography for Southern California, our purpose is to resolve the spatial variation of anisotropy in the upper mantle which plays an important role in our understanding of the Earth's internal dynamics. Shear-wave splitting has always been a key observable in the investigation of upper-mantle anisotropy. However, the interpretation of shear-wave splitting in terms of anisotropy has been largely based on the ray-theoretical modelling of a single vertically incident plane SKS or SKKS wave. In our study, we use sensitivity kernels of shear-wave splitting

to anisotropic parameters calculated by the normal-mode theory, which automatically accounts for the full-wave effects including the interference of SKS with other phases of similar arrival times, the near-field effect, and multiple reflections in the crust. These full-wave effects can lead to significant variations of SKS splitting with epicentral distance and are neglected in ray theory. We image the upper-mantle anisotropy in Southern California using nearly 6000 SKS splitting data and their 3D full-wave sensitivity kernels in a multiscale inversion enabled by a wavelet-based model parameterization. We also appraise our inversion by estimating the spatial resolution lengths using a statistical resolution matrix approach, which shows the finest resolution length of $\sim$25 km in regions with better path coverage. The anisotropic model we obtain displays the structural fabrics in relation to surface geologic features such as the Salton Trough, the Transverse Ranges and the San Andreas Fault. The depth variation of anisotropy does not suggest a strong decoupling between the lithosphere and asthenosphere. At long wavelengths, the orientations of the fast axis of anisotropy are consistent with the absolute plate motion in the interiors of the Pacific and North American plates.

Keywords TAIGER project · Active sources · First-arrival times · Seismic tomography · Taiwan · Shear-wave splitting · Anisotropy · Multiscale tomography · Full-wave sensitivity kernels · Southern California

Parts of this thesis have been published in the following journal articles:

1. Lin, Y.-P., Zhao, L., Hung, S.-H. (2014b) Full-wave multiscale anisotropy tomography in Southern California, *Geophys. Res. Lett.,* 41, doi:10.1002/2014GL061855. (Reproduced with Permission)
2. Lin, Y.-P., Zhao, L., Hung, S.-H. (2014a) Full-wave effects on shear wave splitting, *Geophys. Res. Lett*., 41, 799-804, doi:10.1002/2013GL058742. (Reproduced with Permission)
3. Lin, Y.-P., Zhao, L., Hung, S.-H. (2011) Assessment of tomography models of Taiwan using first-arrival times from the TAIGER active-source experiment, *Bull. Seism. Soc. Am.*, 101(2), 866–880, doi:10.1785/0120100244. (Reproduced with Permission)

Acknowledgements

First and foremost, I would like to show the deepest gratitude to my research supervisor Dr. Li Zhao for providing me guidance, sharing his great ideas with me, and his patience to instruct my writing and presentation skills. I could not have imagined completing the thesis without this perfect advisor. Second, I would like to thank Dr. Shu-Huei Hung as my co-supervisor. She always encourages me when I am struggling and provides me much advice on my research. I am also grateful to my committee, including Dr. Ling-Yun Chiao, Dr. Yuancheng Gung, Dr. Ban-Yuan Kuo, and Dr. Wen-Tzong Liang for their insightful comments and encouragements which incited me to widen my research from various perspectives.

Last but not least. I must express my very profound gratitude to my parents, to my sisters, and to my husband for supporting me spiritually throughout writing this thesis and my life.

I thank the Bulletin of the Seismological Society of America for permission to include copyrighted article and pictures as Chap. 2 of this book. I also thank the journal Geophysical Research Letters for permission to include Chaps. 4 and 5 of this book.

Contents

List of Figures

List of Tables

Chapter 1
Introduction

Understanding the velocity structure in the Earth's interior is one of the fundamental aspects of seismology research. Robust and realistic velocity models ensure the accuracy and reliability of the strong ground motion estimations, which leads to effective seismic hazard assessments. In order to investigate the structural features in the Earth, we analyze the phase and amplitude details of seismic waveforms from active sources or natural earthquakes. This dissertation involves two distinct approaches to probing the Earth's velocity structures: by means of ray-theory and full-wave methods to model the first-arrival times from explosion experiments and the splitting intensities of shear waves from earthquakes, respectively.

1.1 Isotropic Seismic Tomography in Taiwan

The first part of this research is the study of the isotropic P-wave velocity in the upper crust beneath Taiwan using first-arrival times from active-source records.

In order to resolve some of the long-standing issues on the regional tectonics of Taiwan and offshore area, the TAiwan Integrated GEodynamics Research (TAIGER) project carried out a series of efforts during 2004–2009, including land explosions, marine air-gun blasts, and magnetotelluric, and petrophysical observations, to collect various kinds of geophysical data (Wu et al. 2014). The focus in Chap. 2 is to use the first-arrival times obtained in the explosion records of the TAIGER project to evaluate the existing tomography models for Taiwan (Rau and Wu 1995; Ma et al. 1996; Kim et al. 2005; Wu et al. 2007; Kuo-Chen et al. 2012). High-quality first-arrival times are manually-picked from the active-source records and compared with model predictions calculated by finite-difference simulations (Olsen 1994). Results showed that tomography models obtained from traditional travel time inversions provide consistent and qualitatively correct locations of larger-scale velocity perturbations. However, small-scale features are inconsistent

Y.-P. Lin, *Isotropic and Anisotropic Seismic Tomography Using Active Source and Earthquake Records*, Springer Theses, DOI 10.1007/978-981-10-5068-8_1

among the different models, and the velocity perturbations in tomography models are mostly underestimated.

In Chap. 3, we utilize the observed ground-truth first-arrival times from the active sources to determine the structural features of the crust, the topmost layer beneath Taiwan which is also the region with relatively poor resolution in all tomography models. To avoid underestimating the velocity perturbations caused by the regularization in the inversion, we adopt the forward modelling approach (Zelt and Ellis 1988; Zelt and Smith 1992) to deriving the 2D seismic profiles along several linear transects across Taiwan with numerous closely-spaced instruments and in northern Taiwan where broadband stations are densely deployed by various projects. The crisscrossing 2D seismic profiles in northern Taiwan allow us to construct a 3D model by the partition modelling method (Bodin et al. 2009), which provides a stable and smoothly varying velocity pattern without any explicit regularization. The results show that the lateral variation of P-wave speed in Taiwan can be as large as $\sim$50%, much stronger and more realistic than the existing tomography models obtained by traditional travel time inversions.

1.2 Anisotropic Seismic Tomography in Southern California

The second part of this research is a study on the shear-wave anisotropy structure under Southern California using SKS splitting intensity measurements. Our purpose is the development and application of a full-wave approach to regional anisotropy tomographic inversion of shear-wave splitting measurements obtained from regional and global seismic records in Southern California.

In Chap. 4, we discuss the full-wave interpretation of shear-wave splitting in terms of anisotropy based on the strain Green tensor (SGT) approach (Zhao and Chevrot 2011a, b). Full-wave modelling of shear-wave splitting, which automatically accounts for the interference among multiple arrivals within the SKS window and the near-field effect, not only broadens the range of source-receiver geometry in making splitting measurements, but also enables us to resolve the spatial variation of anisotropy structure.

The full-wave approach to shear-wave splitting modelling is applied in Chap. 5 in conjunction with a wavelet-based inversion in a multi-scale anisotropic tomography for the upper mantle under Southern California. The multiscale inversion enabled by a wavelet-based spatial parameterization of the model achieves naturally data-adaptive spatial resolutions. The resolution length of 25–50 km achieved in our 3D anisotropy model for Southern California reveals detailed variations of the strength and fast-axis orientation of anisotropy. Locally small-scale anisotropic fabrics may be associated with surface geologic features such as the possible upwelling beneath the Salton Trough and the ongoing orogeny in the Transverse Ranges. The patterns of anisotropy in our model with weak depth dependence do

not support the notion that the lithosphere is decoupled from the underlying mechanically weaker asthenosphere under Southern California. The longer-wavelength anisotropic structure suggests that the fast axes in both the Pacific Plate and North American Plate are aligned with the absolute plate motion, whereas in the vicinity of the major plate boundary or the SAF system the anisotropy tends to be affected by the motion of both plates.

References

Bodin T, Sambridge M, Gallagher K (2009) A self-parameterising partition model approach to tomographic inverse problems. Inverse Prob 25:055009

Kim KH, Chiu JM, Pujol J, Chen KC, Huang BS, Yeh YH, Shen P (2005) Three-dimensional Vp and Vs structural model associated with the active subduction and collision tectonics in the Taiwan region. Geophys J Int 162:204–220

Kuo-Chen H, Wu F, Roecker S (2012) Three-dimensional P velocity structures of the lithosphere beneath taiwan from the analysis of TAIGER and related seismic datasets. J Geophys Res 117: B06306. doi:10.1029/2011JB009108

Ma K-F, Wang J-H, Zhao D (1996) Three-dimensional seismic velocity structure of the crust and uppermost mantle beneath Taiwan. J Phys Earth 44:85–105

Olsen KB (1994) Simulation of three-dimensional wave propagation in the Salt Lake Basin, Ph.D. thesis, University of Utah, Salt Lake City, Utah, 157 pp

Rau R-J, Wu FT (1995) Tomographic imaging of lithospheric structures under Taiwan, Earth Planet. Sci Lett 133:517–532

Wu FT, Kuo-Chen H, McIntosh KD (2014) Subsurface imaging, TAIGER experiments and tectonic models of Taiwan. J Asian Earth Sci 90:173–208

Wu Y-M, Chang C-H, Zhao L, Shyu JBH, Chen Y-G, Sieh K, Avouac J-P (2007) Seismic tomography of Taiwan: Improved constraints from a dense network of strong motion stations. J Geophys Res 112:B08312. doi:10.1029/2007JB004983

Zelt CA, Ellis RM (1988) Practical and efficient ray tracing in two-dimensional media for rapid traveltime and amplitude forward modeling. Can J Geophys 24:16–31

Zelt CA, Smith RB (1992) Seismic traveltime inversion for 2D crustal velocity structure. Geophys J Int 108:16–34

Zhao L, Chevrot S (2011a) An efficient and flexible approach to the calculation of three-dimensional full-wave Fréchet kernels for seismic tomography: I-Theory. Geophys J Int 185:922–938

Zhao L, Chevrot S (2011b) An efficient and flexible approach to the calculation of three-dimensional full-wave Fréchet kernels for seismic tomography: II–Numerical results. Geophys J Int 185:939–954

Chapter 2
Assessment of Tomography Models of Taiwan Using First-Arrival Times from the TAIGER Active-Source Experiment

In 2008, the TAIGER project conducted an active-source experiment in which seismic records from 10 explosions were collected at nearly 1400 locations on the island of Taiwan. In this study, we manually pick the first-arrival times from the explosion records to ensure reliable and accurate travel time observations, and use them to examine the complex P-wave structural variations in the crust beneath Taiwan. Aided by numerical simulations, we compare the observed first-arrival times with those predicted from a one-dimensional (1D) model and three three-dimensional (3D) tomography models for Taiwan which portray the underlying variations in seismic wave speeds frequently utilized to decipher the regional tectonic framework in Taiwan. We evaluate the quality of the four models by the goodness of fit between the observed and model-predicted travel times. Statistical distributions of the differential travel time residuals allow us to inspect quantitatively the overall effectiveness of these models in replicating the observed 'ground-truth' first-arrival times so as to make an assessment of the strength and deficiency of the resolved velocity structures that agree with or contradict the travel time observations from the explosion experiment.

2.1 Introduction

Taiwan is situated at the boundary zone between the Eurasian Plate (EP) and Philippine Sea Plate (PS). Most of the island is bracketed by two different types of subduction systems. Off the northeast coast of Taiwan the oceanic PS subducts northwestwardly under the continental EP along the Ryukyu Trench, whereas to its south the EP plunges eastward under the PS (Fig. 2.1). The oblique convergence

Originally published in [Bulletin of the Seismological Society of America April 2011 vol. 101 no. 2 866-880].

Y.-P. Lin, *Isotropic and Anisotropic Seismic Tomography Using Active Source and Earthquake Records*, Springer Theses, DOI 10.1007/978-981-10-5068-8_2

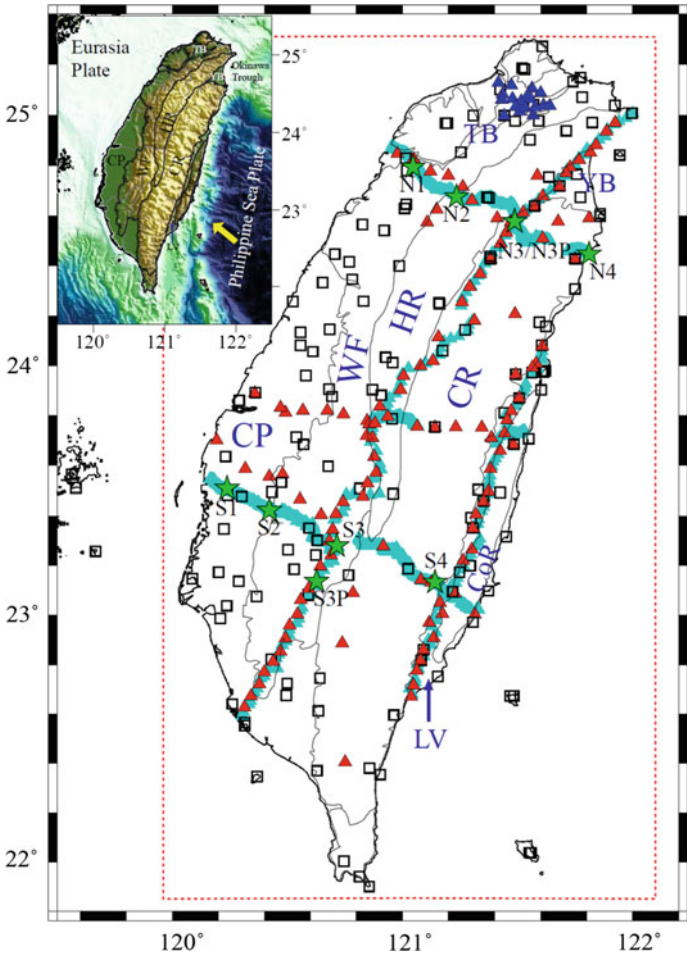

Fig. 2.1 Locations of the TAIGER explosions (*stars*) and stations. Open squares show the stations of permanent CWBSN and BATS networks. *Red* and *cyan triangles* are portable broadband/short-period and TEXAN instruments, respectively, deployed by the TAIGER project. *Blue triangles* indicate portable array stations in the Taipei Basin. Inset map shows the regional tectonic setting. Tectonic divisions in Taiwan shown in this and subsequent figures are: Central Range (CR), Hsueshan Range (HR), Coastal Range (CoR), Western Foothills (WF), Longitudinal Valley (LV), Coastal Pain (CP), Taipei Basin (TB), and Yilan Basin (YB). *Yellow arrow* indicates the current movement direction of the Philippine Sea Plate. The *red-dashed box* indicates the horizontal extent of the finite-difference simulations. Reprinted from Lin et al. (2011) with permission Bulletin of the Seismological Society of America

between these two plates has resulted in the collision of the Luzon Arc with the Chinese continental margin and subsequent orogeny in Taiwan (Teng 1996). Nowadays, the island of Taiwan continuously undergoes a northwest-southeast compression with a convergence rate of about 8 cm/year (Yu et al. 1997; Bird 2003).

The active collision, orogeny, and subduction cause very high rates of deformation (Yu et al. 1997) and seismicity (Wang 1998; Wang and Shin 1998) in the Taiwan region, which provides abundant geological and geophysical observables for studying regional structures and tectonics. Over the past two decades, networks of densely-distributed seismic stations have been deployed across Taiwan and nearby islands as well as offshore on the sea floor. These networks have accumulated a tremendous amount of high-quality seismic data from worldwide earthquakes. Primarily based on P- and S-wave arrival times from local earthquakes, a number of tomography models have been constructed for the seismic velocity structures in the crust and uppermost mantle beneath Taiwan, which are often used to interpret the complex tectonic processes in the region. Rau and Wu (1995) manually picked P-wave arrival times recorded by short-period instruments of the Central Weather Bureau Seismic Network (CWBSN) to image the 3D lithospheric structure beneath Taiwan. Ma et al. (1996) employed the P- and S-wave arrival times reported in the Central Weather Bureau (CWB) earthquake catalog to investigate both the velocity structure and the variation in crustal thickness. Shin and Chen (1998) obtained a layered 1D model suitable for the Taiwan region, which has since been used by the CWB for routine determinations of earthquake hypocenters and origin times. More recently, Kim et al. (2005) combined the augmented dataset from the CWBSN and two temporary seismic arrays in east-central and southern Taiwan to simultaneously determine 3D models of P and S velocities in the crust and uppermost mantle and relocate earthquake hypocenters. Wu et al. (2007) included additional S-P differential arrival times from the Taiwan Strong Motion Instrumentation Program (TSMIP) network and the CWBSN data to construct 3D models of Vp and Vp/Vs ratio beneath Taiwan.

In order to further advance our understanding of regional tectonics, the TAIGER project carried out a series of comprehensive geophysical experiments which collected a large amount of data useful for the accurate determination of earthquake locations and mechanisms as well as the construction of multi-scale images of the crust and upper-mantle structures. One of them was an active-source seismic experiment conducted in the spring of 2008, with a total of 10 controlled-source explosions being shot across the island of Taiwan. The recorded seismic data and scientific outcomes are extraordinary in that the source locations and origin times are exactly known and the observed P-wave arrival times can thus be applied directly to assess the robustness of existing tomography models and alleviate their possible deficiencies. Furthermore, they allow us to explore alternative structural models and geodynamic interpretations consistent with the new data.

In this study, we pick the onset times of the first arrivals from the TAIGER explosion records to examine the crust and uppermost mantle structure beneath Taiwan. We also compare the observed first-arrival times with those predicted by the tomography models in order to evaluate their efficacy in travel time estimation. Although ultimately these active-source first-arrival times can be used as constraints in a future 3D seismic tomography study, their immediate application is in the assessment of currently available tomography results. The rationale for this undertaking is two folds: (1) Coming from controlled experiments almost entirely

free of source uncertainties, these highly accurate first-arrival times provide the "ground truth" that must be satisfied by all structural models, and (2) given the variety of tomography models derived from different datasets and modelling techniques, there is clearly a need for a careful examination of the available models in order to understand their strengths and weaknesses so that these models can be used more effectively and appropriately, and the first-arrival times from active sources provide an accurate and objective ground-truth criterion. Systematic, careful and quantitative assessment of the available regional models is also helpful in selecting the optimal 3D model to serve as the starting model for non-linear iterative full-wave tomography approaches developed in recent years (e.g. Chen et al. 2007; Tape et al. 2009).

For predicting first-arrival times in 3D models, many algorithms based on ray tracing have been developed in the past four decades (e.g. Julian and Gubbins 1977; Červený 1987; Um and Thurber 1987; Vidale 1990; Moser 1991; Podvin and Lecomte 1991). These algorithms provide efficient tools in predicting first-arrival times in 3D structures. However, for the entire Taiwan region we consider in this study, most of the algorithms are either non-parallel thus require expensive shared-memory computers to allow for small spatial grid spacing, or lack the flexibility to switch models easily. Therefore, we adopt the 4th-order staggered-grid finite-difference method (e.g. Olsen 1994; Graves 1996) to compute synthetic seismograms from individual explosive sources. We obtain the first-arrival times from the synthetic seismograms for the 1D model of Shin and Chen (1998) and the 3D models of Rau and Wu (1995), Kim et al. (2005), and Wu et al. (2007), and compare them with the observations to evaluate the reliability of their resolved Vp structures.

2.2 Observations of First-Arrival Times

The first-arrival time data used in our study were measured from the waveform records of the 10 TAIGER explosion shots. Table 2.1 lists the basic information of each explosion source including the GMT time, location, yield, and site condition. Figure 2.1 shows distributions of the stations and explosion sites, among which five shots are located along the Northern Cross-Island Highway and the other five are along the Southern Cross-Island Highway. The recording stations belong to a number of permanent and portable networks which include: (1) the Broadband Array in Taiwan for Seismology (BATS), a permanent network operated by the Institute of Earth Sciences (IES), Academia Sinica; (2) the CWBSN, a permanent network consisting of a real-time monitoring system of short-period, strong-motion and broadband stations; (3) a portable array of broadband seismographs in the Taipei Basin (TBBN) operated by IES; (4) a portable array of 47 IRIS PASSCAL broadband instruments deployed by the TAIGER project along three approximately east-west lines; (5) portable arrays composed of 48 broadband and 20 short-period

Table 2.1 Primary information of the 10 TAIGER explosions

Shot	Yield (kg)	Date mm/dd/year	Time (GMT)	M_L	Longitude (°E)	Latitude (°N)	Elev. (m)	Site class	α (km/s)
S1	1000	02/27/2008	17:01:49	3.02	120.2380	23.50886	6	D1	1.60
S2	750	02/27/2008	17:30:57	2.62	120.4213	23.42339	20	D2	1.67
S3	500	02/26/2008	18:02:46	1.89	120.7147	23.28013	650	B	4.10
S3P	1500	02/26/2008	17:32:43	1.78	120.6267	23.13699	335	B	4.10
S4	750	02/28/2008	17:02:09	2.30	121.1417	23.13288	390	B	4.10
N1	750	03/06/2008	17:03:23	2.56	121.0459	24.79356	55	C2	2.00
N2	750	03/06/2008	17:34:56	1.55	121.2358	24.67563	590	B	4.10
N3	750	03/04/2008	18:01:18	2.10	121.4879	24.57694	405	B	4.63
N3P	3000	03/04/2008	17:01:18	2.67	121.4879	24.57694	405	B	4.63
N4	1000	03/05/2008	17:03:40	2.43	121.8117	24.44690	6	D3	1.74

Note M_L is the magnitude for the explosions determined by the Central Weather Bureau of Taiwan, α is the P-wave speed either given from Vs30 (for Classes C, D and E) or estimated from TAIGER explosion records (for Class B)

instruments deployed by the IES, the National Chung Cheng University, and the National Central University; and (6) an array of TEXAN geophones distributed at a spacing of about 200 m along the Northern and Southern Cross-Island Highways. The geophones were also deployed along the Central Range at a spacing of 2 km in between the portable instruments in (5). The sampling intervals of the records are 0.004 s for the TEXAN instruments and 0.01 s for the rest.

2.2.1 Picking Onset Times from Waveform Records and Removing Elevation Effect

We collected the explosion waveforms from a total of about 1400 recording sites. Most of the records are in good quality, as shown in Fig. 2.2. Figure 2.2a, b exhibit a suite of vertical-component records at a number of stations (Fig. 2.2a) along the Central Range from Shot N3P. In the raw waveform records in Fig. 2.2a, the first motions are sharp and their arrival times can be very accurately determined. In Fig. 2.2b, bandpass filtered version of these records around 1 Hz show that coherent converted surface waves from the explosion can be seen even beyond about 80-km epicentral distance. These short-period Rayleigh waves can be used in dispersion and waveform inversions to investigate both P- and S-wave structures at very shallow depth (1–2 km).

We manually picked the onset times of the first-motions in the raw vertical-component explosion records. The procedure for the onset-time picking is illustrated in Fig. 2.2d. We first zoom in around the emergence of the first motion to a duration of only a few sampling intervals of a seismic record. For instance,

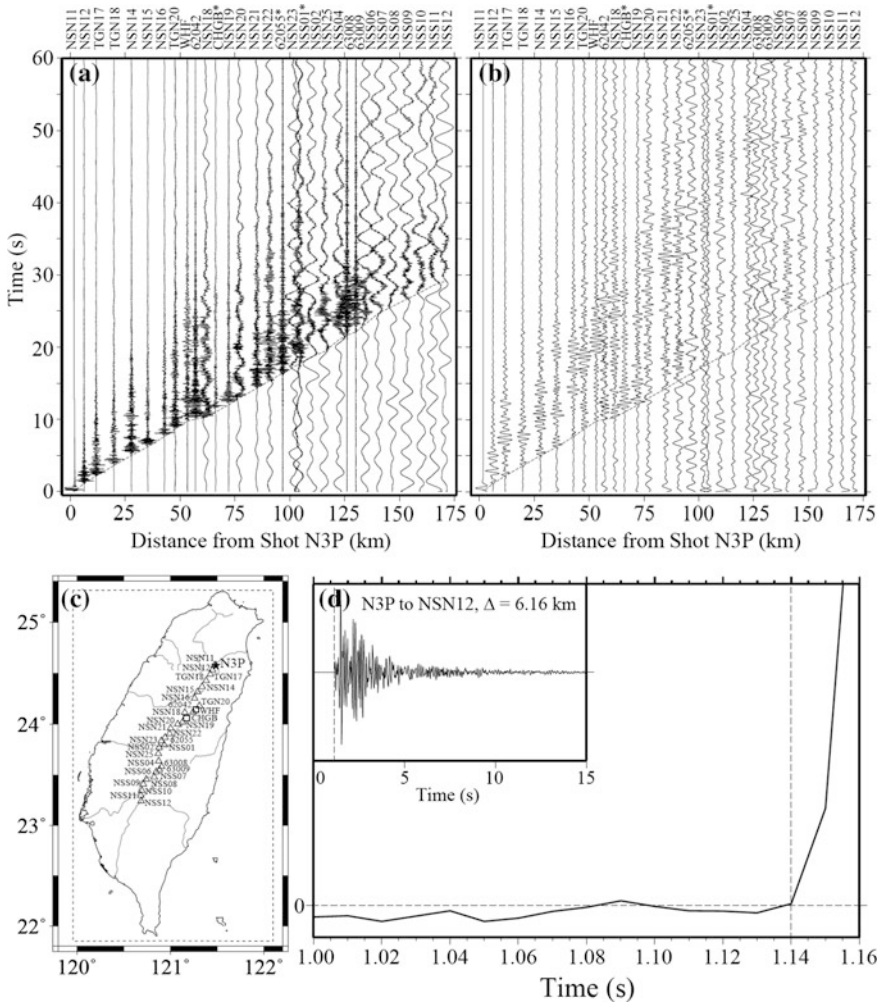

Fig. 2.2 **a** A suite of vertical-component raw seismograms recorded by instruments located along a linear trend from Shot N3P. The dashed line indicates the manually picked first-arrival times. Station names are given at the end of each trace, and stations with no first-arrival time picks are identified by a star. **b** Bandpass filtered versions of the records in (**a**) with cutoff frequencies of 0.8 and 1.5 Hz. **c** Locations of Shot N3P and the instruments whose records are shown in (**a**) and (**b**). **d** An illustration of picking the first-arrival time shown by the record at station NSN12 from Shot N3P. The *dashed line* indicates the first-arrival time pick. Reprinted from Lin et al. (2011) with permission Bulletin of the Seismological Society of America

Fig. 2.2d shows the zoom-in record of a 0.16-s long time window equivalent to 16 sampling intervals. Since the first motion from an explosion is always upward, we choose the onset time of the first motion at the instant of a sudden increase in the slope of the waveform (vertical dashed line in Fig. 2.2d). All of our first-arrival

time picks have been obtained following a set of stringent standards to ensure the consistency, reliability and accuracy. In the end a total of 6029 first-arrival times were obtained from fewer than half of all TAIGER explosion records, most of which have picking errors well below 0.1 s.

The observed first-arrival times from the active-source experiment provide a ground-truth dataset of P-wave travel times, which can be applied to evaluate 3D tomography models by comparisons with model predictions. However, before making this comparison careful consideration must be taken to account for the effect of topography and shallow structure on the first-arrival times which are usually poorly modeled in tomography inversions. The effect of topography on first-arrival times is mainly caused by the elevations of shots and stations relative to the sea level. Since the elevations of shots and stations are exactly known, consideration of the topography effect on first-arrival times boils down to the estimation of the near-surface seismic wave speed.

Current tomography models for Taiwan are confined to the structures below sea level and topography of the region is not taken into account. The shots and stations in the TAIGER active-source experiment are all located at different elevations with a variation range of over 3 km. Therefore, the observed first-arrival times reflect shortest travel times not between two points at sea level, but between two points at different altitudes. To compare the observed and model-predicted first-arrival times, we can make adjustment to either observed or model-predicted arrival times to account for the elevation effect.

In travel time tomography, a quantity called 'station correction' is often used to account for the travel time anomaly associated with the station elevations, strong, small-scale structural heterogeneity, and sharp, discontinuous velocity changes at shallow depths under the stations. These features are usually considered as nuisance in tomography inversions which implicitly assume that the imaged velocity perturbations are weak and smooth. As a result, it is unreliable to use 'station corrections' or near-surface velocities in tomography models to estimate the contributions of the source and station elevations to an observed first-arrival time. Instead, we make use of the results from decades of thorough geological mappings and geophysical surveys in Taiwan (Ho 1988) to determine the near-surface P-wave speed consistent with the geological units at the sites of stations and explosions. Then, for each shot-receiver pair, we estimate the difference in travel time taken along two P-wave ray paths: one being the true ray path from the actual location of the shot to the receiver and the other from the projection of the shot on the sea level to that of the receiver. The geometry is shown by the diagram in Fig. 2.3. The sub-surface portion of the true ray path from S_1 to R_1 has approximately the same length as the portion of the ray path from the sea-level source to the sea-level receiver from S_2 to R_2. From the geometry we have the relation

$$T_{SR} = T_{SS_1} + T_{S_1R_1} + T_{R_1R}, \quad \text{and} \quad T_{S_0R_0} = T_{S_0S_2} + T_{S_2R_2} + T_{R_2R_0}, \tag{2.1}$$

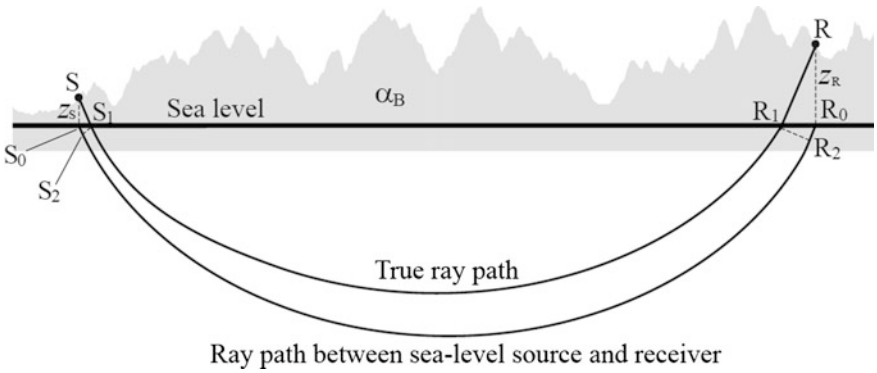

Fig. 2.3 Diagram showing the geometry in making first-arrival time adjustment for elevation travel time. S and R are the actual positions of the shot and receiver, respectively, and S_0 and R_0 are their vertical projections on the sea-level. Solid curves are ray paths from S to R and from S_0 to R_0. S_1 and R_1 are intersections between the ray path from S to R and the sea-level. α_B is the assumed constant P-wave speed of the Class B material between the topographic surface and the sea level. Reprinted from Lin et al. (2011) with permission Bulletin of the Seismological Society of America

Thus we have

$$T_{S_0R_0} = T_{SR} - (T_{SS_1} - T_{S_0S_2}) - (T_{R_1R} - T_{R_2R_0}). \tag{2.2}$$

From the geometrical relations between the sides of Δ SS_0S_1 and Δ $S_1S_2S_0$ and between the sides of Δ RR_1R_0 and Δ $R_1R_0R_2$ shown in Fig. 2.3, we know that

$$T_{SS_1} - T_{S_0S_2} = \frac{z_S}{\alpha_0}\sqrt{1 - p^2\alpha_0^2}, \quad \text{and} \quad T_{R_1R} - T_{R_2R_0} = \frac{z_R}{\alpha_0}\sqrt{1 - p^2\alpha_0^2}, \tag{2.3}$$

where z_S and z_R are the elevations of the shot and receiver, respectively, and p is the ray parameter of the first-arriving P wave. For a given shot, the ray parameter varies with the receiver elevation and the shot-receiver distance. Therefore we can write

$$T_{S_0R_0} = T_{SR} - \delta t_{SR}, \tag{2.4}$$

where

$$\delta t_{SR} = (T_{SS_1} - T_{S_0S_2}) + (T_{R_1R} - T_{R_2R_0}) = \frac{z_S + z_R}{\alpha_0}\sqrt{1 - p^2\alpha_0^2} \tag{2.5}$$

is the difference between the travel time T_{SR} from the actual locations of the shot to receiver and the travel time $T_{S_0R_0}$ between sea-level source and sea-level receiver. Here we assume that the P-wave speed α_0 between the surface and the sea-level is homogeneous.

The source and station elevations z_S and z_R in Eq. (2.5) are known quantities. Therefore, if we also know the topographic surface P-wave speed α_0 and the ray parameter p, we can estimate δt_{SR}, and Eq. (2.4) provides a straightforward means to adjust the travel times T_{SR} from actual locations of the shots to receivers that are manually picked on the records, to $T_{S_0R_0}$, the travel times from sources to receivers on the sea level, which can be compared directly with the model-predicted first-arrival times to assess the validity of the models. After the adjustment to all first-arrival time picks for the elevation-induced time differences, the resulting P-wave travel time anomalies can be used not only for evaluating the quality of the regional tomography models, but also for constraining the heterogeneous structures in the crust and uppermost mantle.

In this study, we estimate the near-surface P-wave speeds by the in situ conditions at the source and station sites. Lee et al. (2001) classified the site conditions in Taiwan into four categories, B, C, D and E, corresponding to Classes S_B, S_C, S_D and S_E, respectively, in the 1997 UBC provisions (ICBO 1997). Lee and Tsai (2008) assigned the site categories of 711 free-field strong-motion stations distributed in Taiwan and estimated the shear velocity values of these four categories. We adopt their classification and determine the site class for each source and station by choosing the same site category as that for the nearest strong-motion station. These four site classes are distinguished by age and rock type (Classes B and C) or engineering soils (Classes D and E). Class B refers to igneous and metamorphic rocks, limestones, and hard volcanic intrusions. Miocene or older rocks may be classified as Class B, with an average shear-wave velocity of 760 m/s to 1500 m/s in the uppermost 30-m layer (Vs30). Sandstones, shales and conglomerates in the Pliocene and Pleistocene, and soft rocks or very compact soils are classified as Class C. Class C has a Vs30 value ranging in 360–760 m/s, and is divided into three subclasses C1, C2 and C3 (Lee and Tsai 2008). Late Quaternary loose sands, silts, clays, gravel deposits or stiff soils like fluvial terrace, and stiff clays are classified as Class D, which is also divided into three subclasses D1, D2, and D3 with Vs30 values varying in 180–360 m/s (Lee and Tsai 2008). Class E, with Vs30 <180 m/s, contains Holocene alluvium flood plains and recent fills. The site classes determined for all the sources and stations used in this study are shown in Fig. 2.4.

In the active-source experiment of the TAIGER project, the sources and stations associated with the site classes of C, D and E are all at low altitudes of a few tens of meters or less. Therefore, for all stations of C, D and E classes, we adopt the Vs30 values in Lee and Tsai (2008) for shear-wave speeds, β, at the sites associated with these three categories, and estimate the corresponding P-wave speed, α, by the so-called Castagna mud-rock equation (Castagna et al. 1985):

$$\alpha = 1.16\beta + 1.36, \tag{2.6}$$

where α and β have the unit of km/s. The estimated P-wave velocities for site classes C, D and E are shown in the inset table in Fig. 2.4.

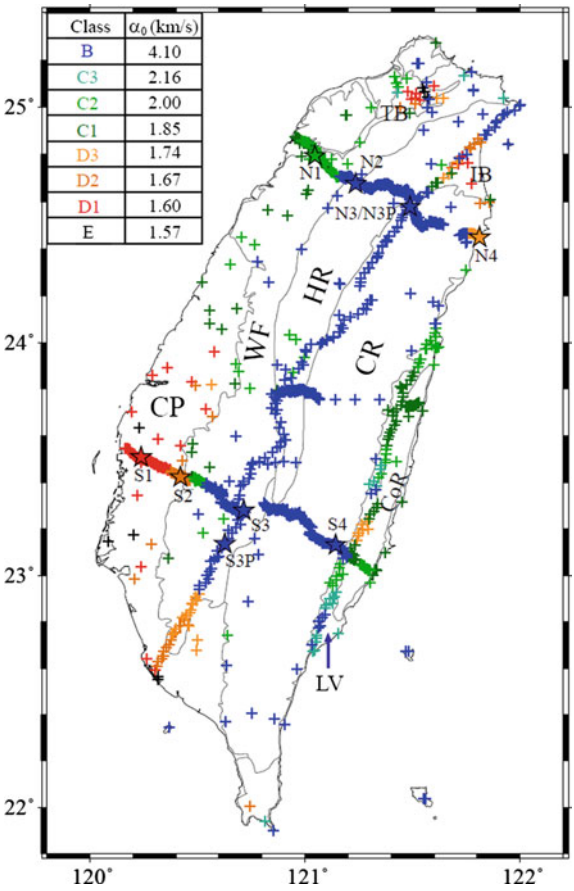

Fig. 2.4 Site classes of all stations and explosions used in this study. The inset table on the top-left corner lists the P-wave velocities for Classes C, D and E estimated directly from the Vs30 values (see text) and the Castagna mud-rock equation. The P-wave speed for Class B is determined by a linear regression between first-arrival times and travel distances at stations within 6 km from Shots N2, S3 and S3P. Reprinted from Lin et al. (2011) with permission Bulletin of the Seismological Society of America

The sources and stations associated with Class B are all located at higher elevations where the velocities above sea level are no longer available from the local Vs30 model. Shots N2, N3P, S3 and S3P are all classified as Class B, and fortunately each of these shots has a number of stations located within a few kilometers. It is worth mentioning that in addition to the TEXAN geophone records, we incorporate data from 13 and 8 accelerometers deployed by IES (Lin et al. 2009) and located less than 1 km away from Shots N3P (N3) and S3P, respectively. The integrated dataset provides a far more accurate estimate of both the origin times and the P-wave velocities near the explosion sites. Assuming that the structural column above sea level at each shot is relatively homogeneous, we estimate the uniform P-wave speed within the column by the linear relation between the first-arrival times and travel distances from the stations less than 6 km to the shot. Figure 2.5 shows the first-arrival times increasing with distances which give the P-wave speed

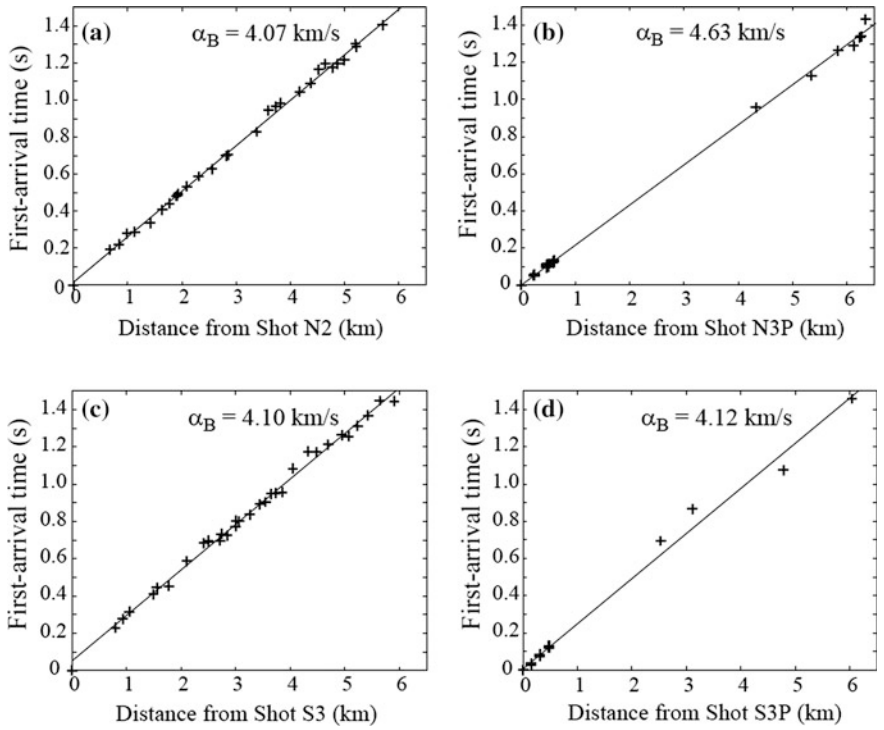

Fig. 2.5 P-wave velocities for Class B estimated directly by least-squares linear regressions between the first-arrival times and distances observed at stations within 6 km from Shots N2, N3P, S3 and S3P. Crosses clustered near the origin in **b** and **d** denote the first-arrival times observed at several accelerometers deployed within 1 km from Shots N3P and S3P, respectively. Reprinted from Lin et al. (2011) with permission Bulletin of the Seismological Society of America

for the metamorphic rock of Class B at each shot by the inverse of the slope of the best-fitting line. The P-wave speeds near Shots N2, S3 and S3P are similar, about 4.1 km/s (Fig. 2.5a, c, d), but is higher near Shot N3P, about 4.63 km/s (Fig. 2.5b), indicating that the material property in the vicinity of Shot N3P significantly differs from that at the other shots. Therefore, we determine the P-wave velocity to be 4.10 km/s for Class B by averaging the estimates at Shots N2, S3 and S3P, and use the value of 4.63 km/s for Shot N3P and the stations within 1 km from the shot. Details of the site classes for the 10 explosions are listed in Table 2.1.

After obtaining the surface P-wave speeds for all site classes for the shots and stations, we use Eq. (2.5) to estimate δt_{SR}, the time differences due to source and station elevations needed to adjust the first-arrival time picks T_{SR} to those between sea-level source and stations $T_{S_0R_0}$ (Fig. 2.3). For stations of site classes C, D and E, they are located above low-velocity sediments with low elevation (a few tens of meters), we thus make the approximations

$$\delta t_{SR} = \frac{z_S + z_R}{\alpha_0}\sqrt{1 - p^2\alpha_0^2} \approx \frac{z_S}{\alpha_0} + \frac{z_R}{\alpha_0}\sqrt{1 - p^2\alpha_0^2}, \quad \text{for C, D or E class explosion site,} \tag{2.7}$$

$$\delta t_{SR} = \frac{z_S + z_R}{\alpha_0}\sqrt{1 - p^2\alpha_0^2} \approx \frac{z_S}{\alpha_0}\sqrt{1 - p^2\alpha_0^2} + \frac{z_R}{\alpha_0}, \quad \text{for C, D or E class station site,} \tag{2.8}$$

$$\delta t_{SR} = \frac{z_S + z_R}{\alpha_0}\sqrt{1 - p^2\alpha_0^2} \approx \frac{z_S + z_R}{\alpha_0}, \quad \text{for C, D or E class explosion and station,} \tag{2.9}$$

Ray tracing tests using realistic structures show that Eqs. (2.7)–(2.9) are very good approximations with only a maximum error of ~ 0.025 s. For stations in class B, the elevations may be too high and we must estimate the ray parameter p more accurately. The first-arrival time picks from the nearly linear array of stations along the five southern shots enable us to derive an average 1D model which can be considered as a representative of the average 1D structure of class B, and then we determine the ray parameter p from the actual locations of the shot to the station by ray tracing in this 1D model. Figure 2.6 shows the elevations of the TAIGER

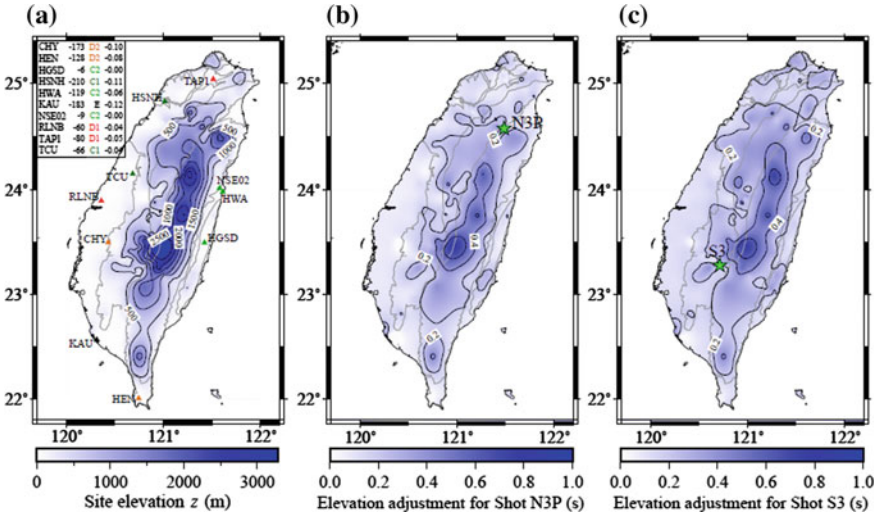

Fig. 2.6 **a** Elevations of stations and explosions. The ten down-hole stations with negative elevations are shown by the *triangles* with the corresponding color for their site classes used in Fig. 2.4. Their elevations in meters, site classes, and the station part of elevation effect (z_R/α_0 in Eqs. 2.8 and 2.9) in sec are listed in the inset box. **b** and **c** Distributions of the travel time adjustment δt_{SR} due to source and receiver elevations (Eq. 2.5) to P-wave travel times from Shots N3P and S3, respectively. Reprinted from Lin et al. (2011) with permission Bulletin of the Seismological Society of America

explosions and stations and the estimated time adjustments δt_{SR} for Shots N3P and S3. The highest station is located at an elevation of 3845 m in the Jade Mountain, which yields the largest travel time adjustment of $\sim$0.71 s. The travel time adjustments for all shot are shown in Fig. 2.7.

2.2.2 *Elevation-Adjusted First-Arrival Times*

After the time delays owing to the elevation effects at the stations and explosion sites are removed, we obtain the adjusted first-arrival times, $T_{S_0R_0}$, which retain only the P-wave travel times accrued within the sub-sea level structures. These in situ measured travel times are then employed to interpolate the variations of the observed first-arrival times emanating from the shots using a minimum-curvature interpolation scheme built in the GMT plotting software (Wessel and Smith 1998). The resulting P-wave travel time distributions from 10 explosions are displayed in Fig. 2.8, where white corresponds to the zero travel time at the shot locations and red color represents the travel time of 50 s and longer. In the vicinity of the shot sites, the P waves only travel a small distance through the region near the surface and therefore the travel time patterns are characterized by the variations of shallow velocity structures near the explosions. As the traveling distance increases, the P waves penetrate deeper and the travel time patterns reflect structural variations at greater depths. Convex and concave geometries of the travel time contours indicate P waves traveling at higher and lower speeds, respectively, along their propagation paths than those along neighboring paths. For example, the contours are slightly convex south of the northern shots, N2, N3 and N3P (Fig. 2.8b–d), and north of the southern shots, S3 and S4 (Fig. 2.8h, j). This indicates that the P waves travel faster at shallower depths beneath the Central Range than the surrounding regions. On the other hand, the concave patterns northwest and southwest of Shot S3 (Fig. 2.8h) are, respectively, related to the presence of the low velocity zones at shallow depth in Chiayi and Kaohsiung regions. We note that the travel time contours may exhibit fictitious patterns introduced by the interpolation scheme, particularly in places where the spatial sampling is sparse. For example, travel time variations from two co-located shots, N3 and N3P, shown in Fig. 2.8c, d, respectively, should be very much alike. However, they are actually quite different in central and southern Taiwan. In particular, in southern Taiwan the travel time contours from N3P are very irregular, whereas those from N3 are almost flat. Because of the much smaller yield for Shot N3, there are fewer first-arrival time picks available for the travel time interpolation than N3P, and as a result the two travel time patterns are similar only in regions near Shots N3 and N3P, where the sampling of the first-arrival times (denoted by solid blue triangles in Fig. 2.8c, d) is dense. Because of this reason, it is important to remember that contours in regions with few observations must be taken with a grain of salt.

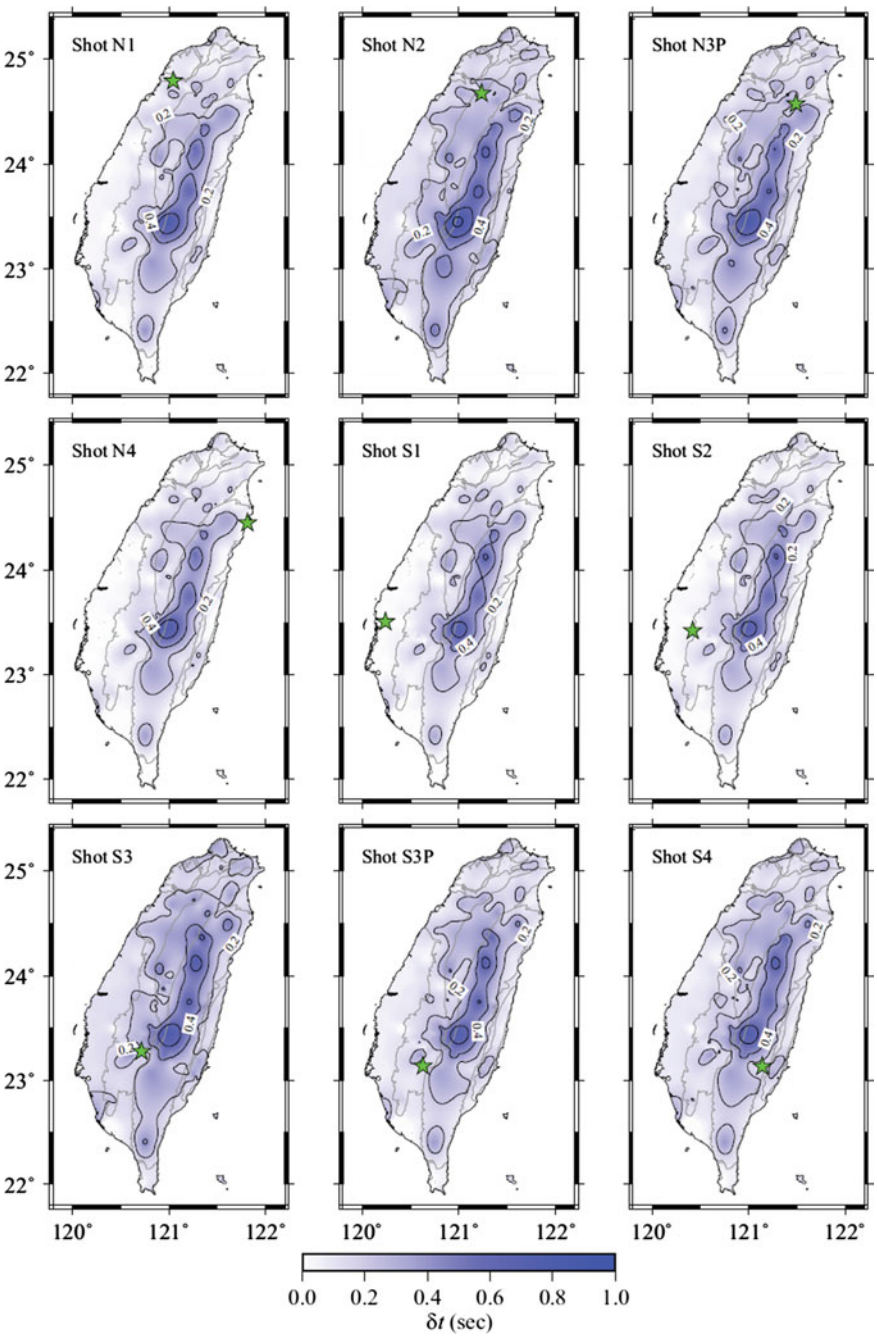

Fig. 2.7 Plots similar to those in Fig. 2.6b, c but for all shots. Shot N3P and N3 are collocated, so only nine plots are shown. Reprinted from Lin et al. (2011) with permission Bulletin of the Seismological Society of America

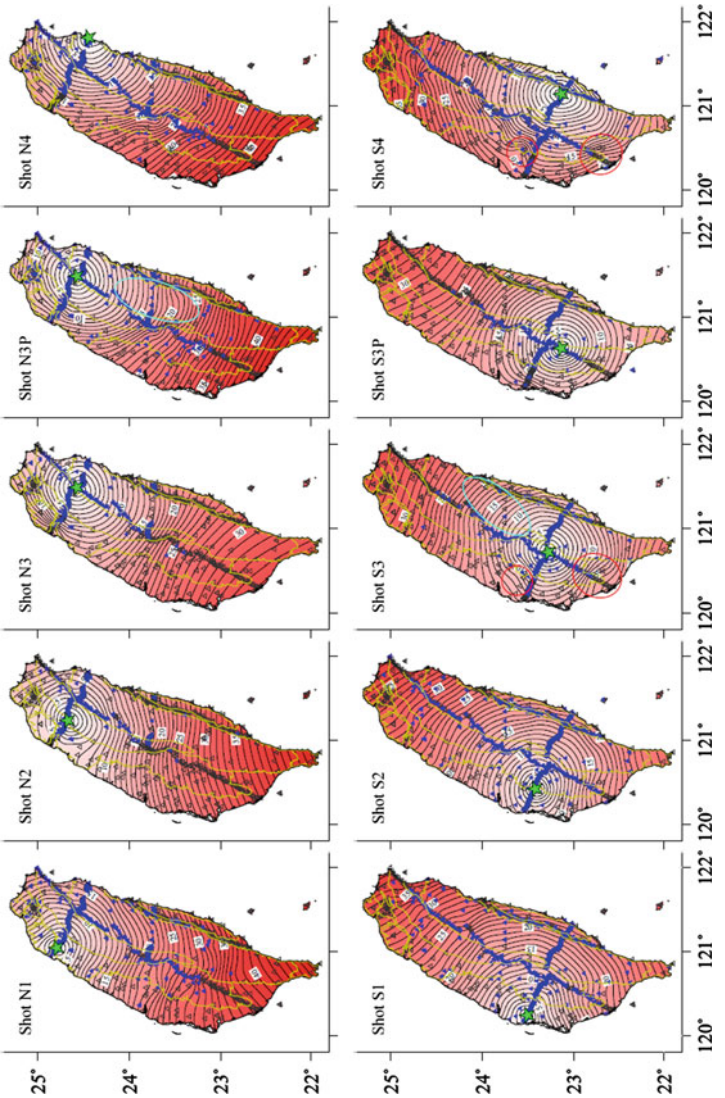

Fig. 2.8 Observed P-wave travel times from the 10 TAIGER explosions. *Stars* indicate shot locations. Stations are denoted by *triangles*, with *solid blue* ones indicating those at which accurate first-arrival times can be obtained. *Cyan ellipses* enclose regions of convex-shaped contours near Shots N3P and S3 indicating a higher P-wave speed at shallow depth beneath the Central Range, while *red ellipses* mark the concave contours indicating a low velocity zones at shallow depth in Chiayi and Kaohsiung regions. Reprinted from Lin et al. (2011) with permission Bulletin of the Seismological Society of America

2.3 Model Predictions of First-Arrival Times

Since the 1990s, the CWBSN stations have provided a good coverage on the Taiwan island to monitor seismic activities occurring in the region. The CWB catalog which routinely reports earthquake source information and P and S arrival times has helped produce a number of tomography models of the crust and uppermost mantle structures beneath Taiwan to improve our understanding of regional tectonics. In this study, we want to evaluate the validity of the resolved heterogeneous structures by comparing the first-arrival times predicted by the tomography models with the ground-truth data obtained from the TAIGER explosion records.

2.3.1 Regional Models for Taiwan

Many P and S velocity models for the crust and uppermost mantle beneath Taiwan have been published in the past two decades. In this study we consider four models that span the entire region, including a regional 1D model (Shin and Chen 1998, hereafter referred to as 1D) and three 3D models (Rau and Wu 1995; Kim et al. 2005; Wu et al. 2007, hereafter referred to as R95, K05, and W07, respectively). Figure 2.9 displays the map views of P-wave speed perturbations of the three 3D models with respect to the 1D model at the depths of 5, 13, 25, and 35 km. Model R95 (Rau and Wu 1995) was obtained using arrival times from 1197 regional earthquakes. The model was discretized into a 3D grid with 8 points vertically down to 80-km depth and a non-uniform horizontal grid spacing of 20–35 km. In contrast, model K05 (Kim et al. 2005), based on ~27,000 arrival times of P and S waves from 1218 earthquakes, was parameterized uniformly with a 8-km horizontal grid spacing and a 2-km vertical spacing down to 148-km depth. Model W07 was derived from an even more extensive dataset: ~300,000 P arrival times and ~174,000 S-P differential times from 17,206 regional earthquakes. The 3D model grid is also non-uniform, with horizontal grid spacing of 7.5–20 km and 17 grid points vertically down to a depth of 200 km. The long-wavelength features are generally in good agreement among the 3D models such that they all reveal a region of low Vp in the western coastal plain and a high Vp at shallow depth (see the maps for 5-km depth in Fig. 2.9), but significantly lower Vp than in the surrounding region at great depths beneath the Central Range (see the maps for 25- and 35-km depths in Fig. 2.9). Model R95 has the smoothest structure while W07 yields the strongest lateral variations with many short-wavelength anomalies superimposed on the long-wavelength structures. All the models use the contour of a subjectively-chosen velocity at the base of the crust to delineate the Moho depth, inferring that the maximum Moho depth reaches to 50–60 km beneath the Central Range.

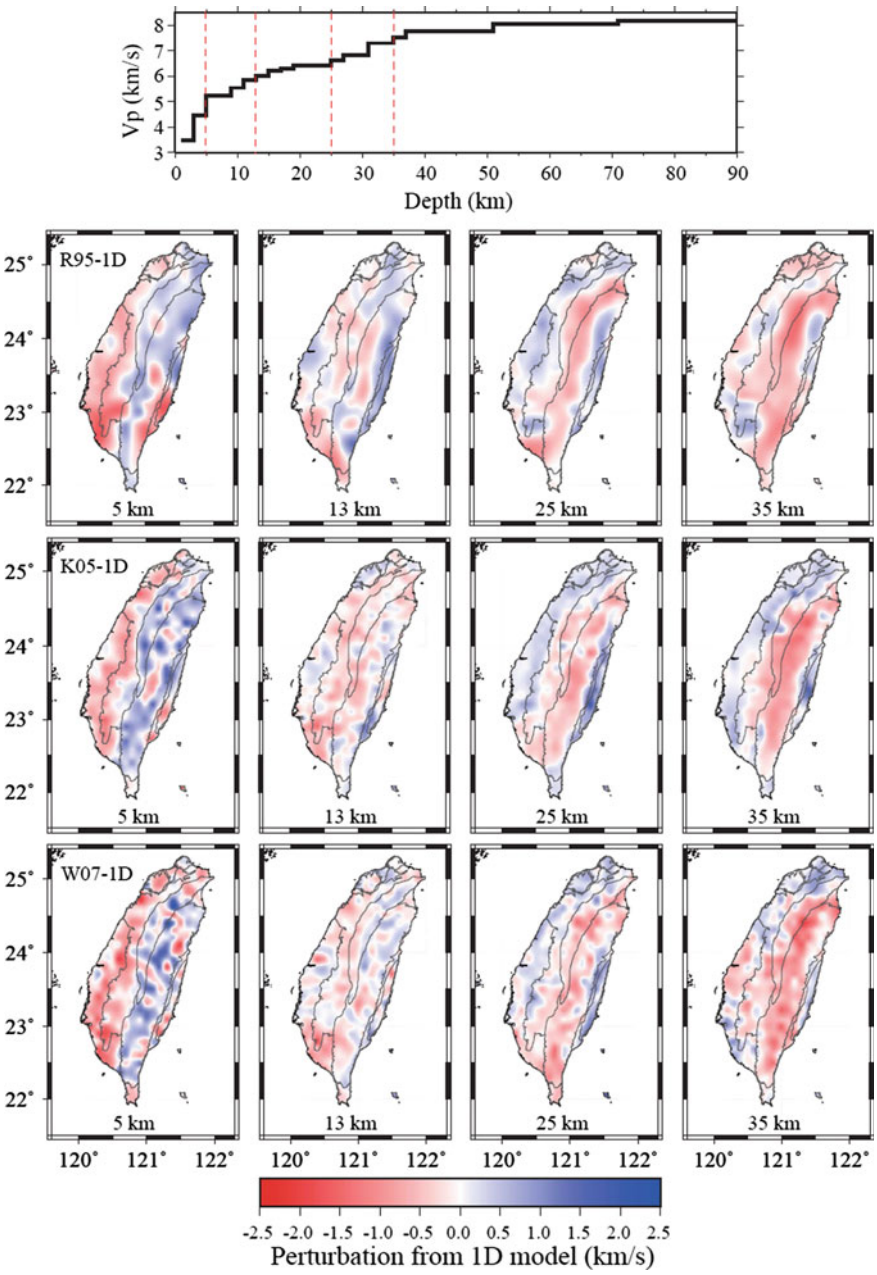

Fig. 2.9 P-wave velocity models considered in our study. *Top* panel shows the 1D model, and the *bottom* three rows show, from *top* to *bottom*, the perturbations of the 3D models R95, K05 and W07 relative to the 1D model at four different depths. In each row, the depths from *left* to *right* are 5, 13, 25 and 35 km, with P-wave speeds of 5.25, 6.02, 6.62 and 7.53 km/s, respectively, in the 1D model. Reprinted from Lin et al. (2011) with permission Bulletin of the Seismological Society of America

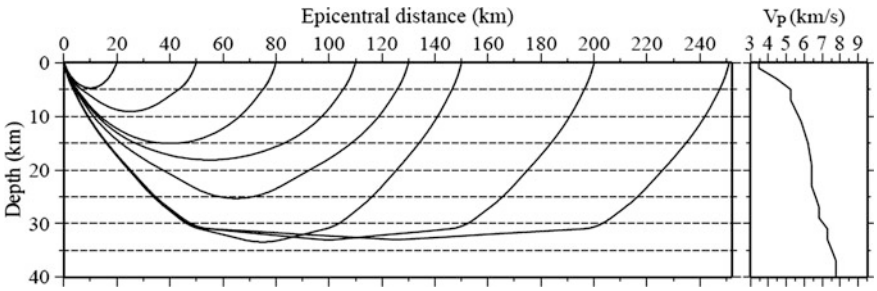

Fig. 2.10 *Left* Typical ray paths for the first arrivals at several epicentral distances. Note that there is a factor of 2 vertical exaggeration. *Right* The 1D model used in the ray tracing. It is a smoothed version of the 1D model shown in Fig. 2.9. Reprinted from Lin et al. (2011) with permission Bulletin of the Seismological Society of America

In order to establish an intuition between the first-arrival times and the depth distribution of wave speed, a few first-arrival ray paths are displayed in Fig. 2.10. These ray paths are calculated by the ray tracing algorithm of Zelt and Smith (1992) in a smoothed version of the 1D model in Fig. 2.9. Ray paths in 3D models are apparently dependent not only on epicentral distance, but also on the specific locations of source and station. However, except for stations close to the explosions, almost all first-arriving P waves propagate through the structure beneath the Central Range, where the Moho is relatively deep. Therefore, the typical ray paths in Fig. 2.10 suggest that almost all of our first-arrival time picks are obtained from Pg waves with a maximum penetration depth of about 35 km.

2.3.2 Numerical Simulations

We employ a staggered-grid finite-difference algorithm (Olsen 1994) with an accuracy of fourth order in space and second order in time to simulate 3D seismic wave propagation through the four models we consider here and calculate the synthetic seismograms from 10 explosions recorded at sea level. Although the recently developed spectral-element method (SEM) provides an accurate approach to model the topography effect on seismic wave propagation (e.g. Komatitsch and Tromp 1999, 2002; Chaljub et al. 2003; Lee et al. 2008), it is a major task to implement a different structural model in the SEM simulation. Therefore, it is not appropriate for this study because of our need to analyze multiple structural models.

The structural volume in our numerical simulations covers an area of 3.5° in latitude by 2.14° in longitude and extends from sea level down to a depth of 80 km. The entire model is discretized into a total of 2240 × 1304 × 458 nodes with a uniform grid spacing of 175 m, resulting in the synthetic P waveforms with

accuracy up to about 4 Hz. To ensure numerical stability, the time step needed to advance the wavefield is 0.008 s.

For the four Taiwan regional models, the model parameters at each finite-difference grid point is obtained by a linear interpolation using the values at the 8 surrounding points in the model grid. For the 10 explosion shots, two of which (N3 and N3P) are co-located, a total of 36 simulations were carried out. A first motion detection program is used to automatically pick the onset times of first arrivals predicted by the four models.

In Fig. 2.11, we present the model-predicted first-arrival times by displaying the differential travel times between 3D and 1D models for Shots N3P (Fig. 2.11a–c) and S3 (Fig. 2.11d–f), since they are the most representative explosion shots in northern and southern Taiwan, respectively. As mentioned previously, interpolation of sparsely sampled travel times may generate artificial patterns caused by interpolation. Since the numerical simulation can provide seismograms and first-arrival time picks at all grid points in the model, we use samples of first-arrival times obtained at a large number of closely-spaced grid points (black dots in Fig. 2.11a, d) that more uniformly cover the study region to obtain lateral variations of the differential travel times between the 3D and 1D models shown in Fig. 2.11.

As seen in Fig. 2.9, the deviations of P-wave velocities of the 3D models from the 1D model are positive at shallow depth and negative at greater depth beneath the Central Range. Effects of these velocity perturbations on the variations of differential travel times between 3D and 1D model are evident in Fig. 2.11. Near Shot N3P in northern Taiwan (Fig. 2.11a–c), the differential times are negative (blue), consistent with higher P-wave velocities at shallow depth beneath the Central Range, whereas further south they become positive (red), caused by lower P-wave velocities at greater depth. Such depth-dependent velocity structure beneath the Central Range has similar effects on the predicted first-arrival times for Shot S3 in southern Taiwan (Fig. 2.11d–f), leading to an opposite distribution of the differential travel times varying from negative in the south to positive in the north. The differential travel times for 3D models K05 and W07 have positive values in the western foothills (WF) and coastal plain (CP), where the Vp anomaly relative to the 1D model is negative at shallow depth. All 3D models yield positive differential travel times localized in the Kaohsiung region in the southwest from Shot S3, where the P-wave speeds at depth less than 10 km are significantly lower than the surrounding regions (see Fig. 2.9). In addition, the differential travel times in Models K05 and W07 for Shot S3 are positive in Hengchun Peninsula at the southern tip of Taiwan, in contrast to those in R95. This difference is directly related to the different near-surface velocity perturbations beneath Hengchun Peninsula (see the maps for 5-km depth in Fig. 2.9), which are negative or slower in K05 and W07 relative to the 1D model, but positive or faster in R95.

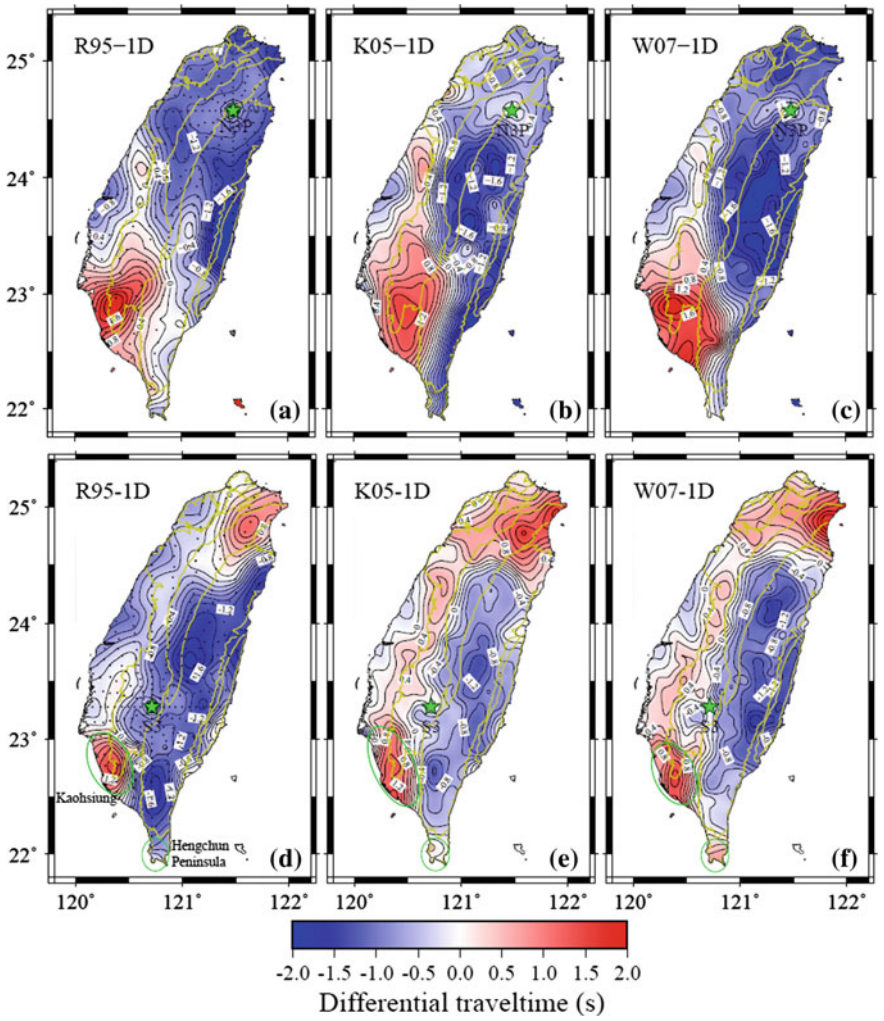

Fig. 2.11 Differential P-wave travel times for Shots N3P (*top* row) and S3 (*bottom* row) obtained by subtracting the first-arrival times predicted by the 1D model from those by individual 3D models, with Model R95 in (**a**) and (**d**), K05 in (**b**) and (**e**), and W07 in (**c**) and (**f**). *Stars* indicate the locations of the shots. The color scheme assigns a cool (warm) color for a negative (positive) differential travel time observed at a given location on sea level, implying that the arriving P-wave takes a shorter (longer) time in the 3D model than in the 1D; that is, it travels from the shot to the given location with a higher (lower) wave speed in the 3D models than in the 1D model. Reprinted from Lin et al. (2011) with permission Bulletin of the Seismological Society of America

2.4 Comparisons Between Observed and Model-Predicted First-Arrival Times

In order to evaluate the capability of the 1D and 3D models in predicting the 'ground-truth' first-arrival times obtained from the explosion records, we conduct a systematic comparison between the observed and model-predicted P-wave travel times. The distributions of the travel time residuals for Shots N3P and S3 obtained by subtracting the model-predicted first-arrival times from the observed ones are shown in Fig. 2.12. As noted before, the interpolation of travel time variations may introduce artificial patterns in places where the samples of first-arrival times are sparse. Therefore, if we perform a point-by-point subtraction of the model-predicted first-arrival times from the observed ones at all of the interpolated locations, the residual distribution can be falsely represented by fictitious residuals. We therefore divide the island of Taiwan into $0.13^\circ \times 0.13^\circ$ squares, with each square having an overlap with each of the adjacent square, and the width of each overlap is one-fifth of the side of the square. For each square, we calculate the average of the residuals from all the samples obtained in that square. The square size is chosen to simultaneously prevent artifacts arising from interpolation and retain robust, small-scale features in the residual distributions.

The residuals of travel times in the 1D and 3D models from Shots N3P and S3 are shown in Fig. 2.12. It is obvious that all the 3D models yield smaller travel time residuals than the 1D model, indicating a significant improvement in the fit of the observed travel times by the tomography models. The residuals in the three 3D models from Shot N3P (Fig. 2.12b–d) are all negative (blue) in northern and central Taiwan closer to the shot site and positive (red) further south. These patterns suggest that the current 3D tomography models are not fast enough at shallower depth and not slow enough at greater depth under the Central Range. Even though the 3D models have predicted a higher Vp at shallow depth and a lower Vp at great depth than the 1D model under the Central Range, they still underestimate the amount of velocity perturbations. Similarly, the residuals from Shot S3 shown in Fig. 2.12f–h are positive (red) in Chiayi and Kaohsiung regions, indicating that the 3D models are not slow enough at shallow depth there. The positive (red) residuals in the northwest corner of the island are found in Models R95 and W07 (see Fig. 2.12b, d), which suggests that these two models are too fast at shallow depth in northern Taiwan. The overall residual patterns for the different models from the other 8 shots are similar and they are presented in the same way in Fig. 2.13. Notwithstanding that all 3D models are superior to the 1D model in predicting the observed travel times, there are still rooms for improvements.

We compare the statistical distributions of the travel time residuals for the four models to quantitatively assess their effectiveness in replicating the observed 'ground-truth' travel times. Figure 2.14a shows the plot of the number of picks vs. residual values for the entire dataset. The number of picks for a residual value is counted from the total number of picks whose residuals are within a ± 0.1 s bin around the given residual value. To further investigate the contribution to the

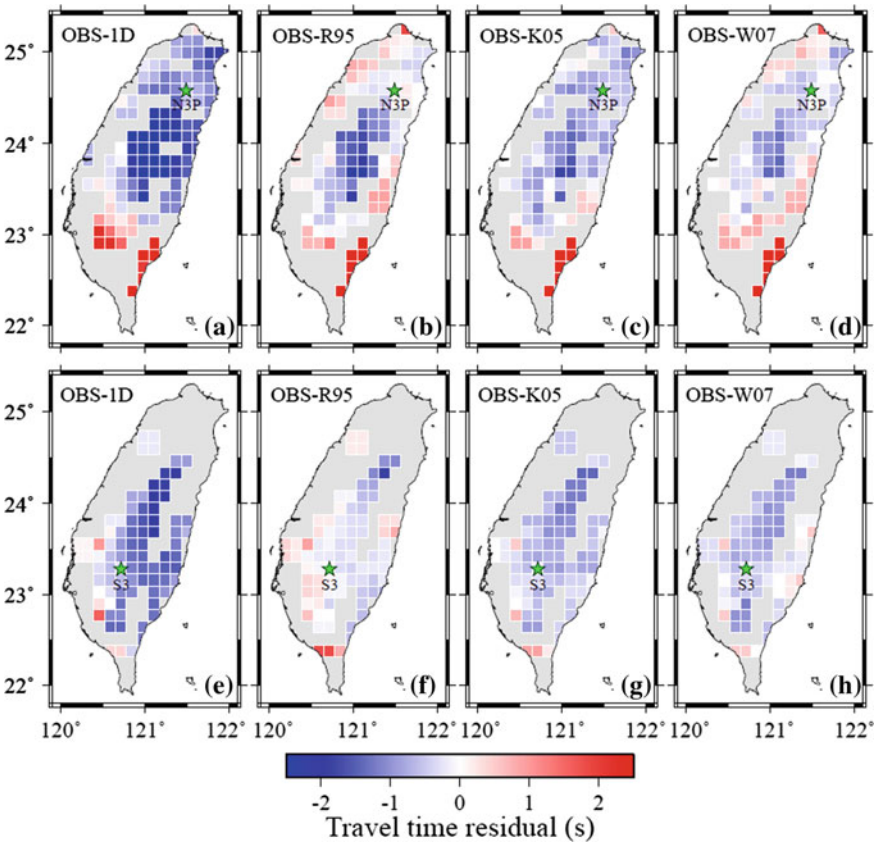

Fig. 2.12 Travel time residuals for Shots N3P (**a**–**d**) and S3 (**e**–**h**) obtained by subtracting individually the model-predicted first-arrival times from the observed ones. *Stars* indicate the locations of the shots. The entire island is divided into 0.13° × 0.13° squares, with each square having an overlap with each of the adjacent square, and the width of each overlap is 1/5 of side of the square. The residual in each square is estimated by averaging all the residuals obtained at the stations within the square. The color scheme assigns a cool (warm) color for an average negative (positive) residual within a given square, implying that on average a P wave arriving within the square would take a shorter (longer) time than the model-predicted times; that is, it actually travels with a higher (lower) P-wave speed from the shot to the specific square than that suggested by the four models. *Squares* with no observed first-arrival times are masked out with *gray color*. Reprinted from Lin et al. (2011) with permission Bulletin of the Seismological Society of America

residuals from the structure under the tectonic units, WF and CP, we separate the dataset into two groups: one for the first-arrival picks associated with P waves only traversing WF and CP, and the other for the remaining picks. The statistical distributions of the residuals for the two groups are plotted in Fig. 2.14b, c. In Table 2.2, we also compare the statistical values of the mean, root-mean-square (RMS), variance (VAR), and skewness of the four models for the three sample sets with different path combinations as in Fig. 2.14a–c.

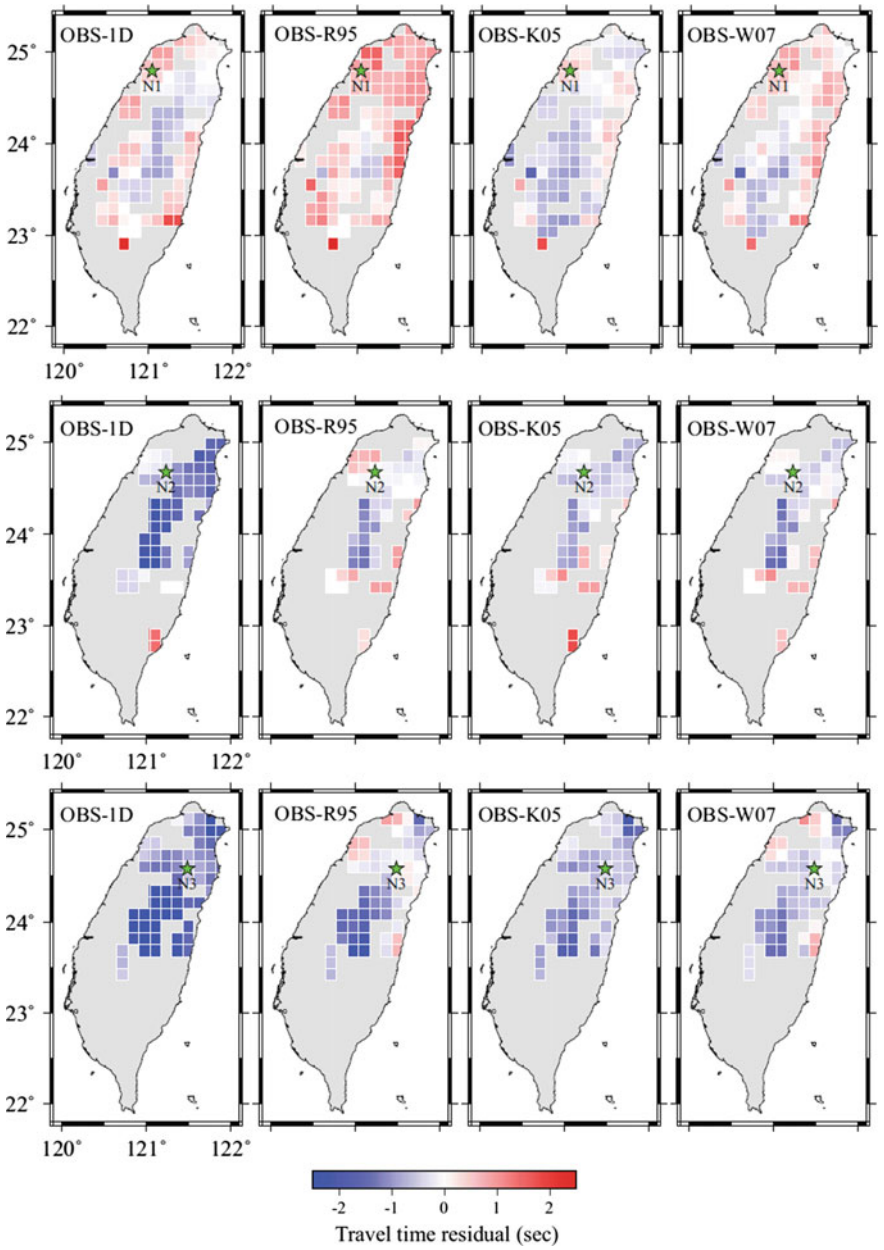

Fig. 2.13 Travel time residuals of the observed first-arrival times relative to the model predictions for Shots N1, N2, N3, N3P, N4, S1, S2, S3, S3P and S4. *Stars* indicate the shot locations. Plots for Shots N3P and S3 are the same as in Fig. 2.12. Reprinted from Lin et al. (2011) with permission Bulletin of the Seismological Society of America

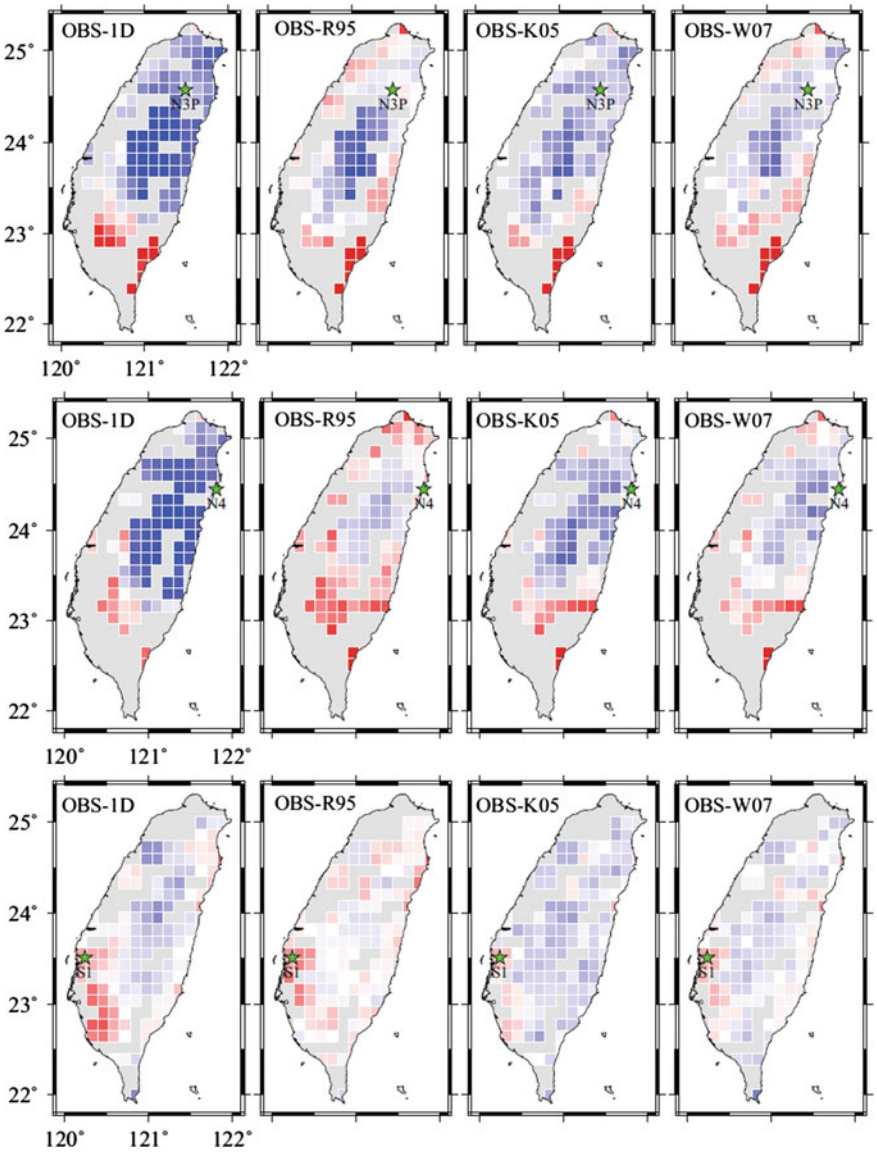

Fig. 2.13 (continued)

The 1D model represents the average velocity structure in the Taiwan region. Even though the resulting travel time residuals have the largest mean (negative), variance, and RMS values among all the four models, their distributions are the most symmetric with the smallest skewness values. The large negative spike near −2 s for the 1D model (black lines in Fig. 2.14a, c) is mostly due to the fast anomaly at

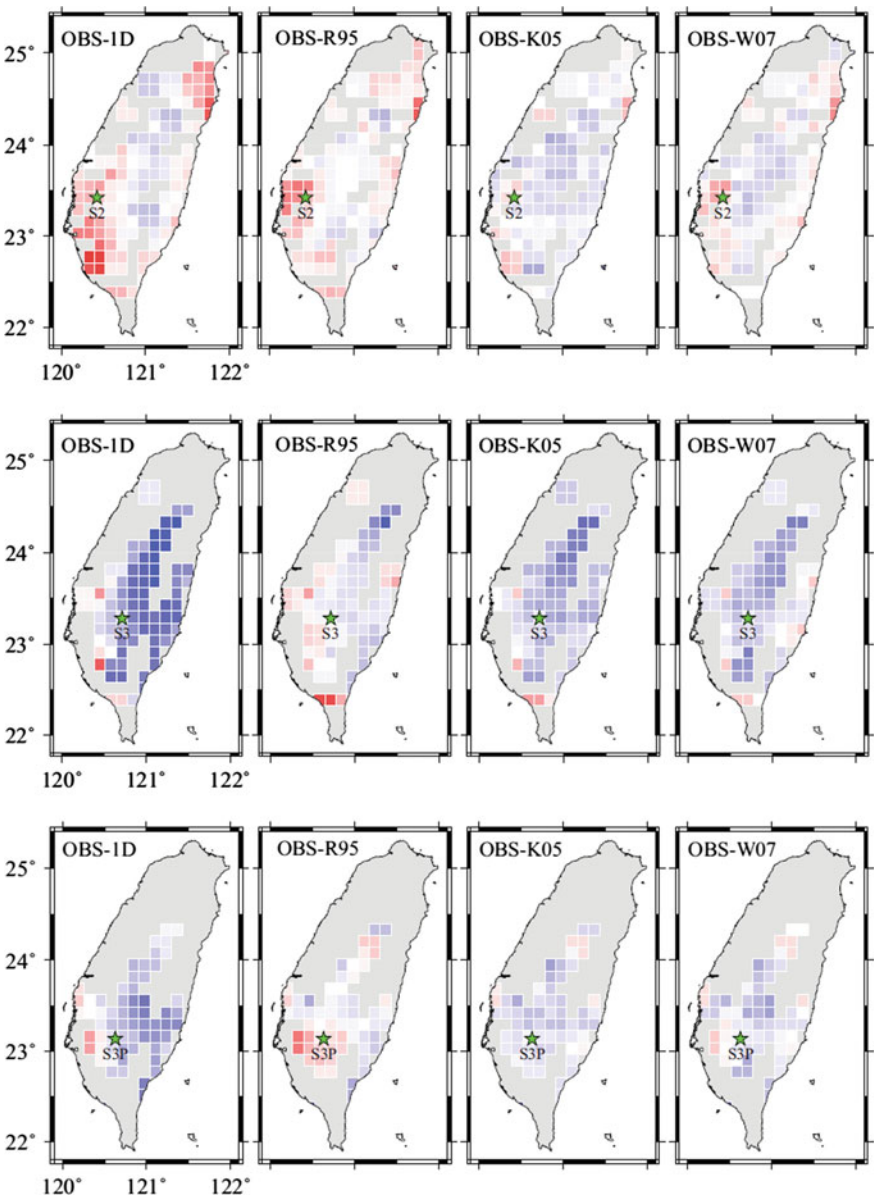

Fig. 2.13 (continued)

relatively shallow depth under the Central Range, which can also be observed in Fig. 2.12a, e. Since the residual distributions for the whole dataset and those excluding the paths through WF and CP are almost indistinguishable, we thus discuss the results from these two sets of the residuals together (see Cases a and c in

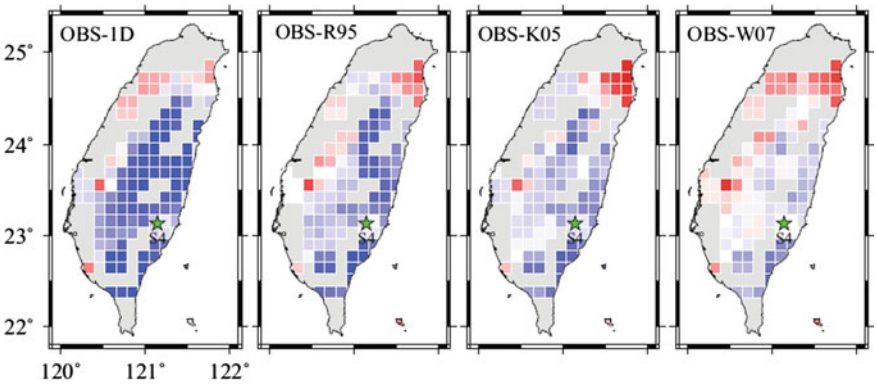

Fig. 2.13 (continued)

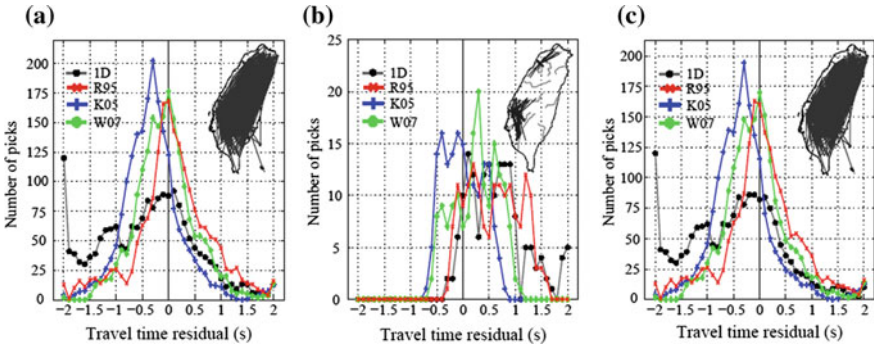

Fig. 2.14 Statistical distributions of travel time residuals for the 1D model (*gray line*) and the 3D models R95 (*red*), K05 (*blue*) and W07 (*green*). The three panels correspond to the residual distributions **a** from all first-arrival time picks; **b** from the picks with propagation paths (*black lines* in the inset map) only traversing the shallow depths under the western foothills and coastal plain; and **c** from all picks except for those in (**b**). In all three panels, the number of picks for a specific residual value is counted from the total number of picks whose residuals are within a ±0.1 s bin around the given residual value. Inset maps illustrate the corresponding ray path distributions. In **a** and **c**, the large negative spike near −2 s for the 1D model (*black lines*) is mostly due to the fast anomaly at relatively shallow depth under the Central Range, which can also be observed in Fig. 2.12a and e. Reprinted from Lin et al. (2011) with permission Bulletin of the Seismological Society of America

Fig. 2.14 and Table 2.2). It is evident that the residuals of Models R95 and W07 have mean values very close to zero and display symmetric distributions. This suggests that the resolved velocity perturbations are less biased toward either the positive (fast) or negative (slow) anomaly. The means of the residuals for the other two models are shifted to negative values, implying that on average they are too slow, particularly for Model K05 which is the slowest among the four models. The spreads or variances of the residuals for the 3D models are clearly smaller than that

Table 2.2 Statistics of residuals for three types of paths in the four models

Case		Statistics	1D	R95	K05	W07
(a)	Picks for all paths	Mean (s)	−0.53	0.08	−0.27	−0.03
		RMS (s)	1.16	0.79	0.75	0.66
		VAR (s^2)	1.07	0.62	0.49	0.44
		Skewness	−0.01	0.02	2.29	1.24
(b)	Picks for paths traversing WF and CP only	Mean (s)	0.66	0.59	0.01	0.24
		RMS (s)	0.86	0.77	0.37	0.49
		VAR (s^2)	0.30	0.24	0.14	0.18
		Skewness	0.68	0.05	0.20	−0.21
(c)	Picks for all paths except for those in (b)	Mean (s)	−0.60	0.05	−0.29	−0.05
		RMS (s)	1.18	0.79	0.77	0.67
		VAR (s^2)	1.03	0.62	0.51	0.45
		Skewness	0.03	0.09	2.38	1.32

for the 1D model, so are the RMS values. As such, the 3D models provide a much improved fit to the observed travel times when lateral velocity heterogeneities are properly taken into account. The residuals for Model W07 yield the smallest mean, variance and RMS values, about 12% smaller than those for R95 and K05, indicating that it has the best overall performance in predicting observed P-wave travel times.

A positive skewness value indicates that the residual distribution has a longer tail to the right of the mean than to its left, and vice versa. Both the skewness values of the residuals for Models K05 and W07 are significantly greater than zero. Besides using the CWBSN data, these two models employed more data recorded by the dense but highly unevenly-distributed stations from temporary seismic arrays and the strong-motion network, respectively. Although more data constraints in K05 and W07 yield a better fits to the observed travel times than Models R95 and 1D, such non-uniform path coverage may cause a skewed residual distribution.

While considering the residuals from the P waves only traversing WF and CP (Case b in Table 2.2 and Fig. 2.14), the residuals of Model K05 instead lead to the smallest RMS and variance, and has the mean closest to zero, indicating that the shallow velocity structures under WF and CP are best represented by those revealed in Model K05. We note here that the numbers of picks in Case (b) are far fewer than those in Cases (a) and (c). More data may be needed to make the inference from Case (b) statistically significant.

2.5 Summary

More than 6000 first-arrival times have been carefully and manually picked from seismic records of an active-source experiment in the TAIGER project, with an accuracy of ± 0.01 s or less for most of the measurements. This ground-truth dataset

of P-wave travel times provides the most reliable criterion against which all tomography models in the Taiwan region can and should be tested.

The observed first-arrival times reveal our long-held understanding of lateral structural variations in the crust and uppermost mantle beneath Taiwan. At shallow depth, P-wave speed is higher under the Central Range than the surrounding regions, but the pattern is reversed at greater depth. Furthermore, regions of strong low-velocity anomalies exist at shallow depth in Chiayi and Kaohsiung regions. Comparisons of the differences between the observed and model-predicted first-arrival times demonstrate that the 3D tomography models R95, K05 and W07 all yield smaller travel time residuals than the 1D model, indicating significant improvements of the 3D models over the 1D model. Despite the fact that overall the 3D models predicted the correct distributions of high and low wave-speed regions, they do actually underestimate the amplitudes of lateral velocity heterogeneities, leaving plenty of rooms for further improvement in the 3D structural images beneath Taiwan. Statistical analysis of the residuals calculated by subtracting the model-predicted first-arrival times from the observed ones shows that the 3D model W07 (Wu et al. 2007) has a mean closest to zero, a RMS residual value about 12% smaller than the other 3D models R95 and K05, and thus provides the best fit to the ground-truth travel times. Among the three 3D models, Models R95 and W07 yield the most symmetric residual distribution with the mean closest to zero, while the residual distributions for Model K05 has negative mean and positive skewness, implying that the velocity structures resolved in Model K05 is on average biased to be too slow. Considering a small sample of travel time residuals obtained from the P waves only traversing the western foothills and coastal plain, the statistical results suggest that the residuals for Model K05 lead to the smallest RMS and variance values, and provide potentially the best fit to the observed first-arrival times in the western foothills and coastal plain regions. In the next chapter, we utilize the same dataset of the accurate first-arrival times from the active-source experiment of the TAIGER project to investigate the isotropic velocity structure in the crust beneath Taiwan.

References

Bird P (2003) An updated digital model of plate boundaries. Geochem Geophys Geosyst 4 (3):1207. doi:10.1029/2001GC000252

Castagna JP, Batzle ML, Eastwood RL (1985) Relationships between compressional-wave and shear-wave velocities in clastic silicate rocks. Geophysics 50(4):571–581

Červený, V. (1987). Ray tracing algorithms in three-dimensional laterally varying layered structures. In: G. Nolet G (ed) Seismic Tomography. Reidel, Dordrecht, pp 99–133

Chaljub E, Capdeville Y, Vilotte JP (2003) Solving elastodynamics in a fluid-solid heterogeneous sphere: a parallel spectral element approximation on non-conforming grids. J Comput Phys 187:457–491

Chen P, Zhao L, Jordan TH (2007) Full 3D seismic waveform tomography for the Los Angeles Basin area. Bull Seismol Soc Am 97:1094–1120. doi:10.1785/0120060222

Graves Robert W (1996) Simulating seismic wave propagation in 3D elastic media using staggered-grid finite differences. Bull Seism Soc Am 86(4):1091–1106

Ho CS (1988) An introduction to the geology of Taiwan: Explanatory text of the geologic map of Taiwan, Central Geological Survey, Ministry of Economic Affairs, Taipei, R. O. C., 192 pp

International Conference of Building Officials (ICBO) (1997) Uniform building code. Whittier, California 492 pp

Julian BR, Gubbins D (1977) Three-dimensional seismic ray tracing. J Geophys Res 43:95–114

Kim KH, Chiu JM, Pujol J, Chen KC, Huang BS, Yeh YH, Shen P (2005) Three-dimensional *Vp* and *Vs* structural model associated with the active subduction and collision tectonics in the Taiwan region. Geophys J Int 162:204–220

Komatitsch D, Tromp J (1999) Introduction to the spectral element method for three-dimensional seismic wave propagation. Geophys J Int 139:806–822

Komatitsch D, Tromp J (2002) Spectral-element simulations of global seismic wave propagation—II. Three-dimensional models, oceans, rotation and self-gravitation. Geophys J Int 150:303–318

Lee CT, Tsai BR (2008) Mapping Vs30 in Taiwan. Terr Atmos Ocean Sci 19:671–682

Lee S-J, Chen H-W, Liu Q, Komatitsch D, Huang B-S, Tromp J (2008) Three-dimensional simulations of seismic wave propagation in the Taipei basin with realistic topography based upon the spectral-element method. Bull Seism Soc Am 98:253–264

Lee C-T, Cheng C-T, Liao C-W, Tsai Y-B (2001) Site classification of taiwan free-field strong-motion stations. Bull Seism Soc Am 91:1283–1297

Lin CJ, Liu CC, Lee WHK (2009) Recording rotational and translational ground motions of two TAIGER explosions in Northeastern Taiwan on 4 March 2008. Bull Seism Soc Am 99 (2B):1237–1250

Lin Y-P, Zhao L, Hung S-H (2011) Assessment of tomography models of Taiwan using first-arrival times from the TAIGER active-source experiment. Bull Seism Soc Am 101 (2):866–880. doi:10.1785/0120100244

Ma KF, Wang JH, Zhao D (1996) Three-dimensional seismic velocity structure of the crust and uppermost mantle beneath Taiwan. J Phys Earth 44:85–105

Moser TJ (1991) Shortest path calculation of seismic rays. Geophysics 56:59–67

Olsen KB (1994) Simulation of three-dimensional wave propagation in the Salt Lake Basin, Ph.D. thesis, University of Utah, Salt Lake City, Utah, 157 pp

Podvin P, Lecomte I (1991) Finite difference computation of travel times in very contrasted velocity models: a massively parallel approach and its associated tools. Geophys J Int 105:271–284

Rau R-J, Wu FT (1995) Tomographic imaging of lithospheric structures under Taiwan. Earth Planet Sci Lett 133:517–532

Shin T-C, Chen Y-L (1998) Study on the earthquake location of 3-D velocity structure in the Taiwan area. Metoerol Bull 42:135–169

Tape C, Liu Q, Maggi A, Tromp J (2009) Adjoint tomography of the southern California crust. Science 325:988–992

Teng LS (1996) Extensional collapse of the northern Taiwan mountain belt. Geology 24:949–952

Um J, Thurber CH (1987) A fast algorithm for two-point seismic ray tracing. Bull Seism Soc Am 77:972–986

Vidale JE (1990) Finite-difference calculation of traveltimes in three dimensions. Geophysics 55:521–526

Wang J-H (1998) Studies of earthquake seismology in Taiwan during the 1897–1996 period. J Geol Soc Chin 41:291–336

Wang C-Y, Shin T-C (1998) Illustrating 100 years of Taiwan seismicity. Terr Atmos Ocean Sci 9:589–614

Wessel P, Smith WHF (1998) New, improved version of the Generic Mapping Tools Released. EOS Trans Am Geophys Un 79:579

Wu Y-M, Chang C-H, Zhao L, Shyu JBH, Chen Y-G, Sieh K, Avouac J-P (2007) Seismic tomography of Taiwan: improved constraints from a dense network of strong motion stations. J Geophys Res 112:B08312. doi:10.1029/2007JB004983

Yu SB, Chen HY, Kuo LC, Lallemand SE, Tsien HH (1997) Velocity field of GPS stations in the Taiwan area. Tectonophysics 274:41–59

Zelt CA, Smith RB (1992) Seismic traveltime inversion for 2D crustal velocity structure. Geophys J Int 108:16–34

Chapter 3
Crustal Velocity Variations in Taiwan Revealed by Active-Source Seismic Observations

In this chapter, we use the manually picked first-arrival times from the closely-spaced receivers sub-linearly deployed by the TAIGER project along island-wide transects and the pre-existing stations distributed in northern Taiwan to examine the underlying velocity profiles. Through a trial-and-error procedure, we fit the first-arrival times by ray tracing and acquire the best-fit 2D models along a number of shot-station profiles. An optimization approach by partition modelling is then employed to construct a 3D model in northern Taiwan based on a collection of densely-distributed crisscrossing 2D profiles in the region. The final stable and smooth 3D model is achieved through the ensemble average of a multitude of partition modelling realizations, without the need for explicit regularization as commonly imposed in tomography inversions. In comparison with recent tomography models in Taiwan, our 2D models along the four main transects and 3D model in northern Taiwan provide much better fit to the observed ground-truth first-arrival times.

3.1 Introduction

The very first images of the three-dimensional (3D) seismic structure under Taiwan were obtained by Roecker et al. (1987) using P and S arrival times from limited numbers of local earthquakes and recording seismographs operated by the Taiwan Telemetered Seismic Network (TTSN). Since then, numerous models have been developed owing to the continued growth in island-wide seismic networks and increase in earthquake locations and phase arrival-time readings routinely reported by the Central Weather Bureau (CWB) of Taiwan (e.g. Shin and Chen 1998; Rau and Wu 1995; Ma et al. 1996). Besides massive amounts of the short-period arrival-time data accumulated in the CWB catalog over two decades, recent tomographic studies have attempted to incorporate complementary datasets from broadband and strong motion networks as well as from temporary seismic

Y.-P. Lin, *Isotropic and Anisotropic Seismic Tomography Using Active Source and Earthquake Records*, Springer Theses, DOI 10.1007/978-981-10-5068-8_3

experiments available in the Taiwan region. Wang et al. (2006) included additional travel time data from both local and teleseismic events recorded by broadband stations in Taiwan and China to image the upper mantle structure at greater depths. To further enhance resolution, Kim et al. (2005) and Wu et al. (2007) incorporated arrival times of regional earthquakes from local seismic arrays with densely spaced stations and an island-wide network of strong motion accelerographs, respectively.

Built on the previous achievements, the TAIGER project carried out joint passive and active source seismic experiments both on-land and offshore around Taiwan. A new set of high-quality, high-density data with accurate GPS timing was acquired mainly for increasing the quality and resolution of tomographic images for the lithospheric structure in and around Taiwan. The latest study of Kuo-Chen et al. (2012) used arrival times of both local and teleseismic events at permanent as well as TAIGER-deployed temporary stations to achieve a much improved resolution in the crust and upper mantle beneath Taiwan and its eastern offshore region.

One of the extremely valuable datasets produced by the TAIGER project is the seismic records from 10 onshore explosions conducted in 2008, which were simultaneously recorded by permanent and temporary stations distributed throughout Taiwan as well as numerous closely-spaced portable broadband and short-period instruments deployed along several linear transects across Taiwan. The impulsive P phase arrivals associated with the precisely-known source locations and origin times enable us to explore the details of the shallow subsurface structures and further understand the geodynamic origin for the active Taiwan orogeny. As described in the previous chapter, we obtained high-quality first-arrival times from the TAIGER explosions and used these ground truth data to make assessment of existing seismic velocity models for Taiwan. The comparative results between the observed and model-predicted first-arrival times demonstrated that the up-to-date 3D models in general provide the correct large-scale features of fast and low velocity anomalies, but yet they all underestimate the amplitudes of lateral variations, leaving plenty of rooms for further improvement in the 3D structures beneath Taiwan.

The study discussed in this chapter is an attempt to fill in the gaps in understanding the shallow crustal structure of Taiwan and enhancing the accuracy and resolution of the lateral velocity perturbations by using the ground-truth first-arrival times from the TAIGER project. In constraining the crustal structure by the active-source first-arrival times, we adopt a forward modelling approach to derive the two-dimensional (2D) seismic profiles along several sub-linear deployments of extremely densely distributed instruments. In addition, taking advantage of the relatively high-density of existing instruments in northern Taiwan, we are also able to derive 2D models along a number of linear profiles there. Based on these crisscrossing 2D seismic profiles in northern Taiwan, we further construct a 3D model by the partition modelling method, which results in robust and smoothly varying velocity structures without the need for explicit regularization.

In what follows, we start with a brief introduction of the active-source data and a presentation on the derivation of the 2D seismic profiles, followed by a discussion of the 4 island-wide transects and the 22 dense profiles in northern Taiwan, and the comparison with existing tomography models. Then, we discuss our

implementation of the partition modelling technique in which the crisscrossing 2D seismic profiles in northern Taiwan are used to obtain a smooth and stable regional 3D model. Features in our 3D model for northern Taiwan are explained within the context of the geological and tectonic framework and a comparison with the existing tomography models.

3.2 Data: Active-Source First-Arrival Times

We use the first-arrival times manually picked from the records of the active-source experiments conducted by the TAIGER project in 2008. There are a total of 10 explosions shot along two east-west (E-W) transects, with five across north Taiwan and another five across south Taiwan. More than 6000 first-arrival times were manually picked from records at about 1400 sites equipped with different kinds of instruments. Most of the receivers in northern Taiwan belong to permanent broadband and short-period networks. The receivers temporarily deployed by the TAIGER project comprise two groups arranged in four linear arrays across Taiwan. The first group involves the portable broadband and short-period seismometers (inverted triangles in Fig. 3.1) deployed along two north-south (N-S) transects running through the Central Range and the Coastal Range in eastern Taiwan, and two E-W transects along the Northern and Southern Cross-Island Highways and roughly coincide with the two transects of the 10 explosions. The second group comprises a large number of TEXAN geophones (upward triangles in Fig. 3.1) inserted between the seismometers in the first group. In the end the instrument spacing is about 200 m along the two E-W transects and about 2 km along the two N-S transects. The sampling intervals of the records are 0.004 s for the TEXAN instruments and 0.01 s for the rest.

All of our first-arrival time picks have been obtained following a stringent standard to ensure the reliability and accuracy. These arrival-time data, the vast majority of which have picking errors well below 0.1 s, have been used to assess the quality and validity of the existing tomography models (Lin et al. 2011). An effective use of these active-source data is of course to conduct a regularized tomography inversion jointly with a large passive-source dataset (e.g. Kuo-Chen et al. 2012). In this study, however, we use the first-arrival times only by taking advantage of their high accuracy as well as their certainty in the location and timing of sources. The confidence in the accuracy of our data demands us to maximize the fit to the ground-truth first-arrival times, which leads to a more realistic strength of velocity perturbations in the resulting models.

To maintain sufficient resolution with the relatively small set of active-source data, we focus on the 2D profiles covered by the densely-distributed receivers during the TAIGER active-source experiments, which include the four long transects across Taiwan and a number of shorter linear profiles around the greater Taipei metropolitan area in northern Taiwan. The shorter profiles are formed by connecting each of 5 explosions along the northern E-W transect with stations

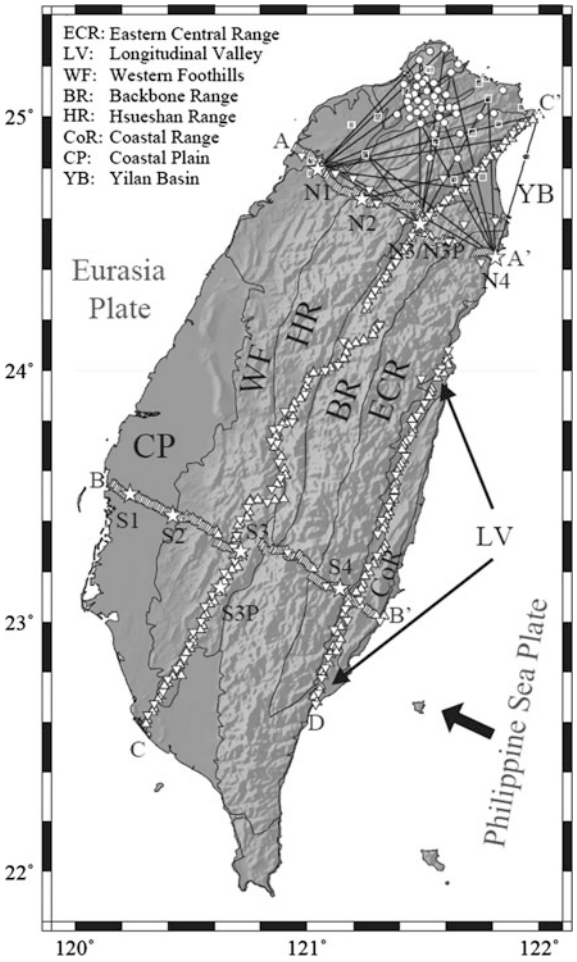

Fig. 3.1 Locations of the TAIGER explosions (*stars*) and receivers. Note that Shot N3 and N3P are co-located. *Open squares* show the stations of the permanent CWBSN and BATS networks. *Regular* and *inverted triangles* denote portable broadband/short-period and TEXAN instruments, respectively, deployed by the TAIGER project. Due to very close spacing between receivers along two east-west transects, we only plot a triangle for every 10 stations. *Circles* indicate the receivers of temporal seismic networks in and around the Taipei Basin. *Thin curves* delineate the boundaries between geological provinces. The *thick arrow* indicates the current direction of motion of the Philippine Sea Plate. Locations of the pseudo-2D (P2D) profiles along the four cross-island transects AA', BB', CC' and DA' are portrayed by the densely distributed receivers (regular and inverted triangles), whereas the P2D profiles in northern Taiwan are shown by the *black lines*

distributed within a narrow azimuthal range. Owing to the high density of instruments in northern Taiwan including broadband and short-period seismometers and closely-spaced geophones, we are able to obtain 2D velocity models for a total of 23 profiles (including Profile AA').

Ray tracing results show that the maximum bottoming depths of the ray paths involved in our first-arrival time picks are ~35 km for the longest path along the central N-S transect and less than 20 km for the shorter paths in northern Taiwan. Therefore, our dataset will provide constraints to P-wave speed mainly in the shallow crust. Nevertheless, owing to the sub-linear deployments of densely-spaced receivers and unambiguous identification of phase arrivals from precisely-known sources, our highly accurate first-arrival time picks provide us an excellent opportunity to conduct detailed analyses of 2D structures along multiple cross sections in throughout Taiwan. Furthermore, the availability of densely-distributed and crisscrossing 2D seismic profiles in northern Taiwan allows us to construct a 3D model of the shallow crust in the region, which has been relatively poorly constrained in the existing tomography models.

3.3 2D Profiles of P-Wave Velocity Structure

Taking advantage of the sub-linearly deployed and closely-spaced receivers, we first estimate the 2D subsurface velocities along the four cross-island transects (AA' and BB', CC', and DA' in Fig. 3.1). Each of these four profiles is covered not only by closely-spaced instruments but also involves two or more explosions. As such, the recorded first-arrival times provide sufficient ray crossings to well-constrain the lateral velocity variations. Since the two E-W transects across north and south Taiwan span all the major orogeny-caused geological divisions, and the other two N-S transects run along the orogenic belts, i.e. the Central Range and the Coastal Range, the resulted 2D models enable us to characterize the seismic features of individual geological provinces of Taiwan.

3.3.1 Ray Tracing Modelling for Constructing 2D Models

To derive the 2D models along the strike and depth of all the linear transects as shown in Fig. 3.1, we examine the variation of the ground-truth first-arrival times with the offset distances between every explosive source and the almost linearly aligned receivers. As shown in Fig. 3.2, for a given transect, we fit all the available travel time versus distance curves simultaneously by a 2D velocity profile composed of multiple segments of depth-dependent one-dimensional (1D) models pieced together.

As the onset times of the first arrivals were manually picked from the waveforms with a predominant period of about 0.2 s, we adopted a ray-theoretical approach exclusively for high-frequency wave propagation to model and interpret the observed first-arrival times. A computationally-efficient algorithm developed by Zelt and Ellis (1988) and Zelt and Smith (1992) is employed to trace various rays through general 2D models and calculate the theoretical travel times of

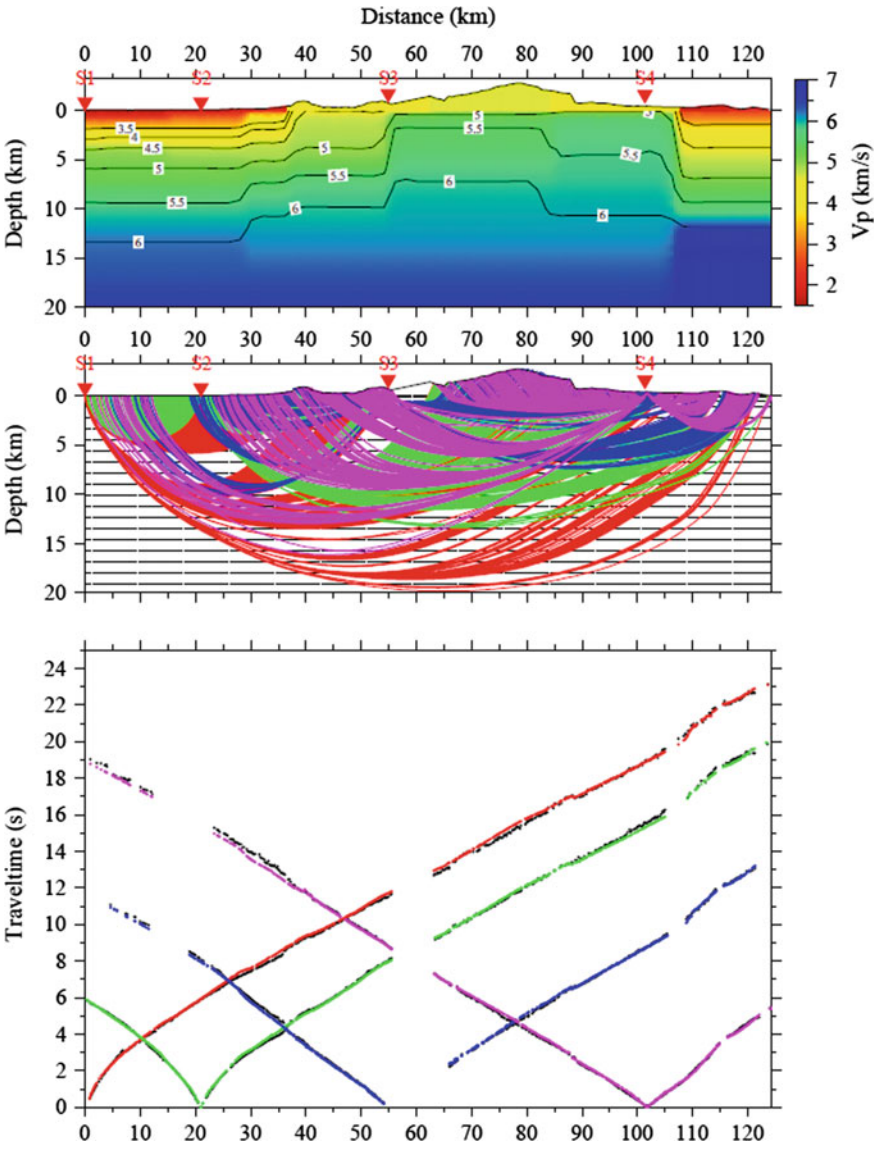

Fig. 3.2 An example showing the fitting of travel time-versus-distance curves predicted by a Pseudo-2D (P2D) model. Shown here is the modelling of travel times of the first arrivals emanating from the explosions and recorded at a linear array of closely-spaced stations along the southern E-W transect (Profile BB' in Fig. 3.1). The three panels from top to bottom show respectively the P2D model, ray paths associated with the first arrivals, and comparison of first-arrival time observations (*black* dots) with those predicted by the P2D model (dots with the same colors as used to draw the ray paths)

corresponding phase arrivals. The algorithm numerically solves a pair of ordinary differential equations in a 2D Cartesian coordinate system by invoking the zero-order, high-frequency asymptotic ray approximation (Červený et al. 1977). Besides ensuring the high accuracy and stability of the numerical solver, the algorithm allows for flexible parameterization of the velocity models and consideration of surface topography as well. This is especially important for Taiwan which is situated in an active orogenic belt with strong heterogeneity and dramatic variation of surface relief. As a result difference in elevations between receivers makes significant contribution to the variations of the observed first-arrival times from local explosions, which must be accurately taken into account in ray tracing modelling.

The high accuracy of our first-arrival times allows us to fit them to the maximum extent without considering the tradeoff between the data fitness and desirable features of the model. We also maintain the modelling accuracy by calculating the first-arrival times using the previously discussed ray tracing algorithm without linearizing the forward problem.

Geologically the Taiwan Island is divided into several distinct regions (see Fig. 3.1), so for each profile a single 1D model would not provide sufficient fit to the first-arrival times, whereas a 2D model capturing the structural contrasts between different geological provinces can do a much better job. Therefore, our target model for each profile is one composed of a number of 1D models pieced together. Hence we refer to them as pseudo-2D (P2D) models. A P2D model can better reflect the geological divisions along its profile. However, the seismic parameters of each P2D model, including the number of constituent 1D models, the depth-dependent velocity structure of each 1D model and the boundary locations between the 1D models, are all determined by fitting the first-arrival times in a trial-and-error process. In each trial, we adjust the seismic parameters of the P2D model intuitively based on the ray paths of the first arrivals and the examination of several features in the predicted and observed travel time curves. These features include, as shown in Fig. 3.2, the absolute values of the arrival times at individual stations, the slopes of the travel time curves, as well as changes in the slopes. In the travel time curve formed by first-arrival times from a particular explosion, the slope is determined by the average velocity between the source and stations, whereas a change in slope indicates a horizontal discontinuity. For example, if the travel time curve is steep with a relatively large slope, the P-wave speed would increase more slowly with depth, leading to a vertically smooth velocity profile. One such case is exemplified in the structure with a small positive velocity gradient at shallow depths beneath the western Coastal Plain near Shot S1, as constrained by the steep travel time curve in the distance range of 0–20 km from Shot S1 (Fig. 3.2). On the other hand, when we line up the travel time curves from several different explosions as in Fig. 3.2, an important feature is a change in the slope at the same horizontal location in the travel time curves, such as the one around 110 km in Fig. 3.2. This is a clear indication that the rays are entering into a region with sharp lateral contrast in wave speed. This gives us the clue as to the need for two different 1D models on the two sides and the locations of the boundaries between the 1D segments can be

adjusted to account for the characteristics of the travel time variations associated with different geological zonations. These subtle features help us determine the configuration of the 1D models in the P2D model. Therefore, the final P2D model is obtained solely by maximizing the fit to the observed ground-truth first-arrival times, not by the well-known geological boundaries on the surface. By adopting this intuitive forward modelling trial-and-error approach, we ensure that in the process of reducing the travel time residual, the models we get do not have wild and physically implausible velocity variations. The final P2D models we obtained have more realistic lateral velocity variations (~ -60 to +40%) and fit the ground-truth seismic data.

3.3.2 2D P-Wave Velocity Profiles Across Taiwan

A typical example of the fit between the observed and predicted first-arrival times associated with the optimal P2D model for the southern E-W transect BB' (See Fig. 3.1 for the location of the profile) is shown in Fig. 3.2. To model the first-arrival times using the 2D ray tracing algorithm of Zelt and Ellis (1988) and Zelt and Smith (1992), the vertical plane below the source-receiver line is divided into multiple vertical segments representing 1D depth-dependent structures. The velocity model within each 1D segment is parameterized by a mesh with the horizontal and vertical grid spacing of 2 and 1.12 km, respectively. To accommodate the high velocity gradient near the surface, the top two layers are further refined in the vertical direction with a half-grid size of 0.56 km. While tracing the rays through the model with the surface topography, the velocity between the grid nodes is determined by linearly interpolating the values assigned at the surrounding nodes. The algorithm provides travel times of the three most common phases: reflected, refracted, and head waves. In this study, the ones with least travel times are always chosen as the predicted first-arrival times.

We start the trial-and-error procedure for each profile with the source-receiver pairs of shorter distance to put good constraints on the shallowest structures first, and gradually move on to pairs with increasing distances to improve the structures at greater depths. As shown in Fig. 3.2 for profile BB', the maximum penetration depth of the first-arrival rays is about 20 km along the ~ 120 km long transect, which imposes a limit on the depth resolution of our P2D model. However, multiple explosions conducted at different locations along the profile and recorded by a linear array of closely-spaced receivers provide large amounts of first-arrival data with intersecting ray paths to cross-check the modelled velocity structures. With the availability of dense ray coverage associated with the accurate first-arrival time data, we are able to illuminate the crustal structure along several key transects across Taiwan with unprecedented clarity and reliability.

All of our resulting P2D models provide first-arrival time predictions in excellent agreement with the observations. In a previous study, we have used the first-arrival times at receivers very close to the TAIGER explosion sites to estimate the

near-surface wave speeds in different geological provinces (Lin et al. 2011). Those values are used to fix the velocities near the surface for our P2D models in this study. As expected, the predicted travel times at the receivers very close to the explosive shots, mainly determined by the near-surface velocity, fit almost perfectly to the observations as shown in the lower panel of Fig. 3.2. After each adjustment of the seismic parameters in a P2D model, the travel time residuals measured by the differences between the observed and predicted first-arrival times are used to assess the goodness of data fit and model quality. The final P2D model is found by a trial-and-error process, though tedious sometimes, to reduce the residuals as much as possible.

The P2D models obtained along the four island-wide transects are displayed together in Fig. 3.3. Table 3.1 lists the statistics of the residuals between the observed and predicted first-arrival times calculated from our P2D models and the corresponding profiles in the three recent tomography models: K05 (Kim et al. 2005), W07 (Wu et al. 2007), and KC12 (Kuo-Chen et al. 2012). Along the northern E-W transect AA', the resulting 2D structure obviously reveals a region of high velocity beneath the Central Range (CR) in the middle and a distinct low

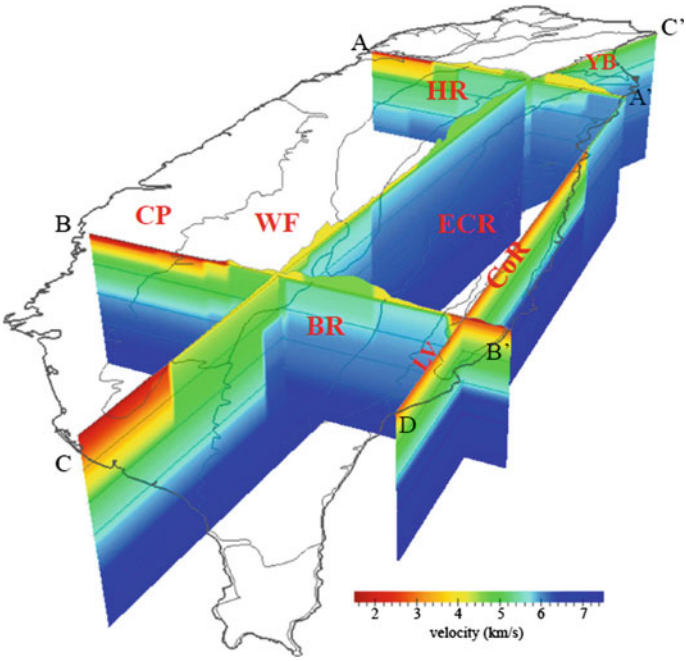

Fig. 3.3 A perspective view of the P2D models along the four main transects across Taiwan Island. There is a factor of 2 vertical exaggeration. The *gray* horizontal lines in each profile are depth contours at every 5 km interval. The tectonic divisions along the profiles across Taiwan are manifested by a number of composite segments with 1D depth-varying velocity structures which form the P2D model

Table 3.1 Statistical comparison of the residuals of first-arrival time predictions by the four models relative to observations along the four cross-island transects

	Mean	RMS	VAR*
P2D	−0.007	0.12	0.02
K05	−0.25	0.45	0.15
W07	0.02	0.45	0.20
KC12	0.34	0.47	0.11

*VAR variance of the residuals

velocity zone at shallow depths of 0–5 km under the Western Foothill (WF) and Coastal Plain (CP) to the west. The tectonic divisions of northern Taiwan are clearly manifested by a series of the segmented 1D models combined to form the P2D model. Under profile BB' parallel to AA' which also cross the major tectonic provinces in southern Taiwan, the resulting structure also shows strong lateral variations, where the velocities under the Eastern Central Range (ECR) appear to be higher in shallow regions and have smaller gradients at greater depths than those under the Backbone Range (BR).

The subsurface structures under the LV and CoR, attributed to parts of the oceanic crust of the Philippine Sea Plate, display strong velocity variations with depth. The velocities under the longest transect CC', which follows mostly the trend of the Central Range, are primarily constrained by the first-arrival times from Shots N3P and S3 to a N-S trending linear array of closely-spaced receivers. The northernmost part of this transect running through the Hsueshan Range (HR) has the same structure as shown in profile AA'. The middle part, mainly located in the CR, has a higher velocity at shallow depth than other tectonic provinces. The southern end of the profile that falls into the WF and CP exhibits a structure similar to that in the westernmost part of Profile BB'. The P2D model along the eastern Profile DA' is constructed based on the first-arrival time data from Shots N4 and S4 to a linear receiver array deployed along the LV. The structure beneath the northernmost part of DA' within the ECR is almost identical to that in the eastern portion of AA'. We use a single 1D model to represent the average structure under the LV and CoR, partly constrained by the shallow velocity under the easternmost part of Profile BB'. The resulting model also shows distinct velocity variations with depth, similar to the structure of an oceanic crust.

In Fig. 3.4, we compare the structures of our four P2D models with those in the same 2D vertical slices of the three recent tomography models. The rays for the first-arrival times used to derive the P2D models reach the maximum penetration depth of about 20 km under the linear transects AA', BB' and DA', and ∼35 km under the longest N-S transect CC'. As a result, we only compare the structures in the resolvable depth range extending down to ∼25 km. Being a patchwork of 1D vertical segments, our P2D model obviously lacks small-scale heterogeneities as those in the tomography models. Despite different degrees of roughness, all the models display the large-scale structural variations along the four profiles in accordance with the geological zonation. Such features are manifested by a region of high velocity under the CR and of very low velocity at shallow depth under the CP. One unique aspect of our P2D models is that the very shallow structure along

the main transects is well constrained by the dense near-surface rays from the TAIGER explosions, which was not possible previously. The lateral velocity perturbations in most shallow regions from the three tomography models are apparently not as strong as those in our P2D models. Particularly under the LV (the easternmost part of Profile BB') and CP (the western and southern end of Profile CC') which have larger velocity variations with depth, the P-wave speeds in the topmost 5 km of the tomography models are in general too high. The shallow region under the northeastern HR (the northernmost part of Profile CC'), however, is too slow compared to our P2D model.

In addition, all the four models show the structure beneath the CR (the middle portions in Profiles of BB' and CC') having a relatively higher speed than in the rest of the geological zones. While the large-scale features revealed at greater depths (>5 km) are very similar, the velocity above 5 km depth is a bit too slow in Models K05 and W07. Model K05 is overall slow enough at shallow depth (e.g. along Profile BB' in Fig. 3.4), with a thick low velocity layer under the CP; it thus provides a better fit to the observed first-arrival times than the other tomography models (Lin et al. 2011). However, its lateral variations near the surface are relatively smooth and the velocity under the CR is too slow. Model KC12 is the only tomography model with the constraints of the TAIGER data. It has on average a high P-wave peed beneath the CR and exhibits the structural variation very

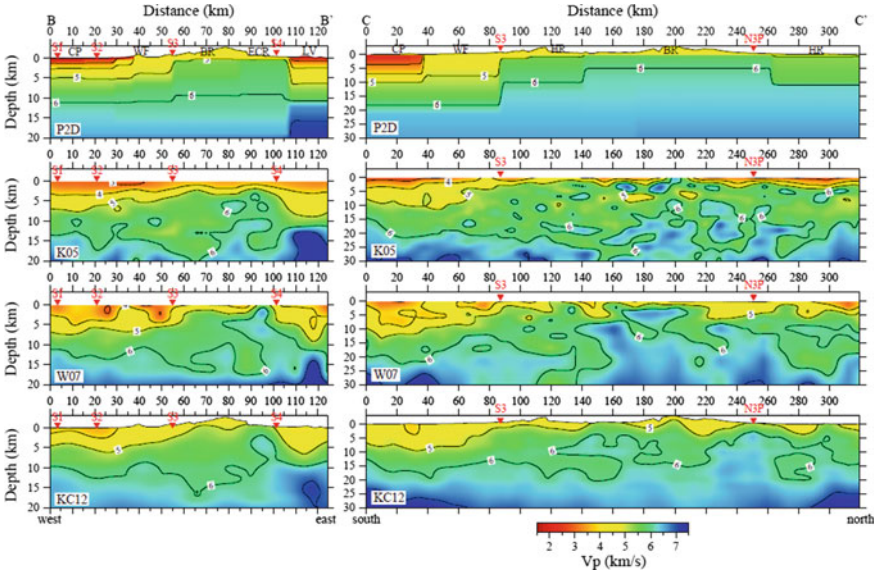

Fig. 3.4 Comparisons between our P2D models along BB' and CC' and the three recent tomography models, K05 (Kim et al. 2005), W07 (Wu et al. 2007), and KC12 (Kuo-Chen et al. 2012). Note that the vertical scales are different for the two cross sections. The large-scale velocity variations are in general similar among the four models. However, in the three tomography models the velocity contrasts between different regions are not strong enough in the shallow crust

consistent with our P2D model, except for the near surface region under the CP and LV where the velocities are not sufficiently low. Model W07 also shows similar features to the other tomography models, characterized by velocities that are too slow beneath the ranges but too fast under the plains. Although all three models derived from regularized travel time inversions resolve reasonably well the locations of high and low velocity anomalies, the resulting strengths of these anomalies are usually too weak in comparison with our P2D models, as can be expected from the damping effect applied in the tomography inversions.

To make a quantitative comparison between the four models, we follow the same approach as in Lin et al. (2011). We first calculate synthetic seismograms from every explosive source in the three tomography models K05, W07 and KC12 using a finite-difference (FD) method (Oslen 1994). Topographic corrections are then made to the predicted first-arrival times obtained from the synthetic P waveforms. Travel time residuals obtained by subtracting the first-arrival time predictions from the observations. The comparison of residuals for the four models shown in Fig. 3.5, where the number of picks refers to all the data used in obtaining the four P2D models shown in Fig. 3.3, and symbols denote the total number of picks whose residuals are within a ±0.1 s bin for different models.

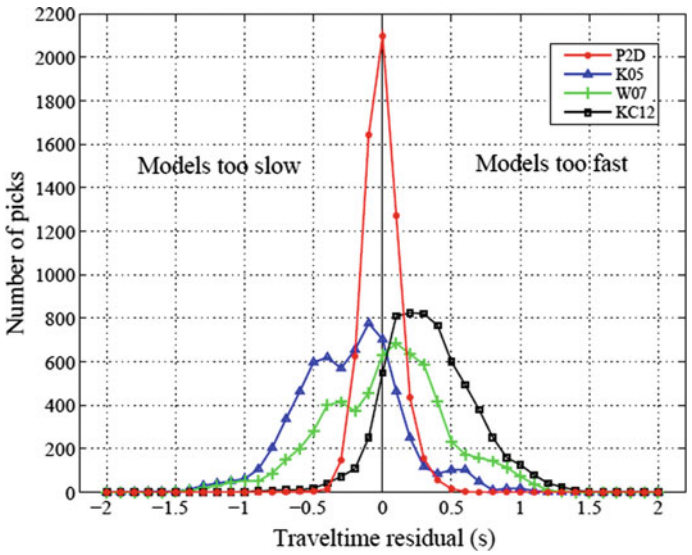

Fig. 3.5 Statistical distributions of travel time residuals associated with the first-arrival time picks along the four cross-island transects for our P2D models (*red* curve) and the other 3D models, K05 (*blue* curve), W07 (*green* curve), and KC12 (*black* curve). The number of picks is counted from all first-arrival time data used to derive the four P2D models, and colored symbols correspond to the total number of picks whose residuals are within a ±0.1 s bin. The residual distribution for our P2D models yields a sharp peak centered around zero, which results in the smallest mean, RMS, and variance among the four models listed in Table 3.1

Table 3.1 compares the statistical mean, root-mean-square (RMS), and variance of the residuals between the four models. The distribution of the residuals of Model K05 is distinctly skewed to negative values, mainly resulting from the low velocity at shallow depth beneath the CR as seen in Fig. 3.4. As opposed to a large negative mean for K05, the residuals for Model KC12 are mostly positive, indicating that its velocity is on average too high. The residuals of our P2D models have the smallest values of RMS and variance with a mean close to zero. This comparison demonstrates that our P2D models provide the best fit to the observed travel time data from the TAIGER explosions and also capture properly the regions of high and low velocities associated with different tectonic provinces and geological zonations.

3.3.3 2D P-Wave Velocity Profiles in Northern Taiwan

Besides a large amount of data collected along the four island-wide profiles, we have also obtained the first-arrival time picks from the five explosions along the northern transect AA' to the receivers distributed in northern Taiwan (Fig. 3.6).

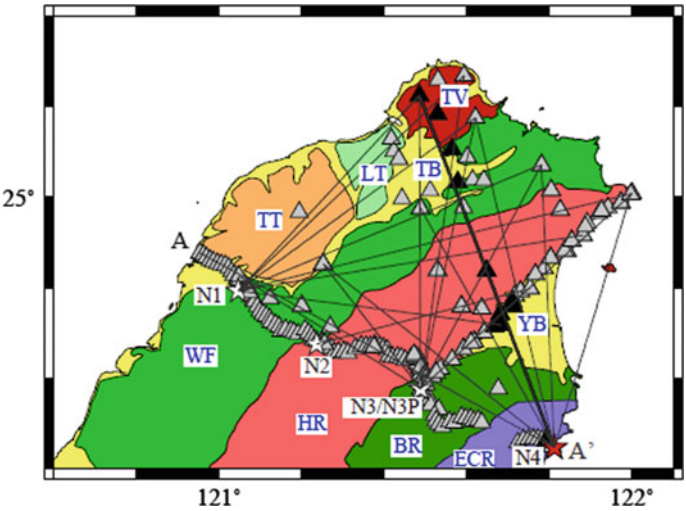

Fig. 3.6 Locations of the 2D profiles in northern Taiwan. In addition to the island-wide W-E transect AA' across northern Taiwan, we define 8 profiles from Shot N1, 1 from N2, 6 from N3P, and 7 from N4. The thick black line shows an example of the 2D profile defined by Shot N4 and several receivers (*black* triangles) in an azimuth range of ±10° across the profile. The background color delineates the physiographic/geological provinces in northern Taiwan, modified from the geologic map published by the Central Geological Survey of Taiwan. Tectonic divisions in northern Taiwan encompass the orogenic belts from the east to west: the Eastern Central Range (ECR), Backbone Range (BR), Hsueshan Range (HR), Western Foothills (WF), Linkou Tableland (LT), Taoyuan Tableland (TT), and the Tatun Volcano Group (TV) that lies at the northern tip of Taiwan. The Taipei Basin (TB) in the west and Yilan Basin (YB) in the east are situated in between these tectonic divisions

This dataset allows us to make an accurate and detailed estimate of the shallow near surface structure, which is essential to earthquake hazard assessment and risk analysis for the greater Taipei metropolitan area in northern Taiwan. Because the receivers in this region are neither linear nor evenly-spaced, we construct a number of linear transects emanating from each of the five explosions to the receivers within a narrow azimuthal range. As a result, we obtain a total of 23 linear transects (including the previous E-W transect AA') crisscrossing northern Taiwan. The travel time variations between the receivers within individual swaths are used to derive the corresponding P2D models under these transects.

All the resulting P2D models in northern Taiwan together in a perspective view are shown in Fig. 3.7, compared with those extracted from the three recent tomography models. Due to the shorter lengths of these profiles, the maximum structural resolution of the P2D models only reaches down to about 15 km depth. A striking feature of our P2D models lies in the strong lateral velocity contrast of almost ±30% between the Taoyuan and Linkou Tablelands (TT and LT) in the west and the mountain ranges (HR, BR, and ECR) to the east. The very low velocity anomalies at shallow depths are seen both in the Taipei and Yilan Basins (TB and YB).

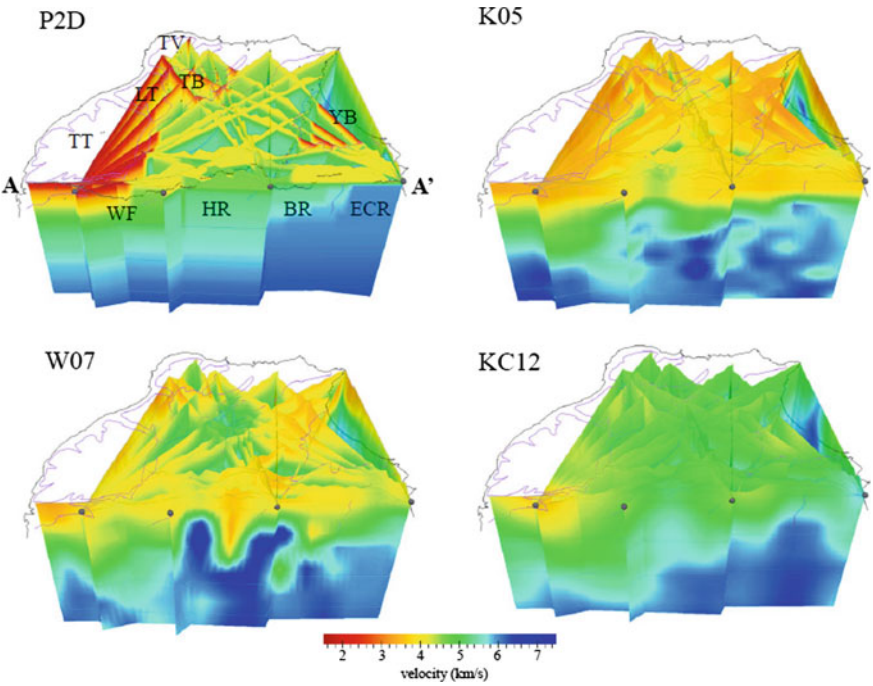

Fig. 3.7 **a** Perspective view of a collection of the P2D models in northern Taiwan plotted with a vertical exaggeration of a factor of 3. Gray horizontal lines are depth contours at every 5 km interval. **b–d** Structures along the same 2D profiles in northern Taiwan as in (**a**) extracted from the three tomography models, K05, W07, and KC12, respectively. Note that the structure along the E-W transect AA' is the same as that shown in Fig. 3.3

The velocities under the mountain ranges appear to be higher and increase steadily from the HR in the west to the ECR in the east. A region of high velocity is also observed under the Tatun Volcano (TV) Group.

The three tomography models show very different patterns of lateral variations in northern Taiwan. Overall, Model K05 has the lowest velocity above 5 km depth among these three models, but seems too slow beneath the eastern Ranges. Even though K05 reveals a more layered structure similar to our P2D models, with a small positive vertical gradient of velocity in the western part of northern Taiwan that helps fit its predicted first-arrival times to the observed ones, the overall velocity in the northwest Taiwan is still not sufficiently low. Model W07 is also too slow at shallow depth beneath the mountain ranges and too fast in the western tablelands and the Taipei Basin. The fastest region also occurs beneath the Ranges at greater depth. Model KC12 is relatively fast in the entire region, where the velocity variations both vertically and laterally beneath the Central Range are comparable to our P2D models. However, the speed at shallow depth is mostly too high in the entire region of northern Taiwan.

The comparisons of the travel time residuals of the four models for the 2D profiles in northern Taiwan only are in Fig. 3.8. Similar to Fig. 3.5, the numbers of picks are counted in every 0.2 s bin of the residuals. The corresponding means, RMS values, and variances are also tabulated in Table 3.2. Obviously, our P2D models provide the best fit to the observed data as demonstrated by the curve of the residual distribution having a strong peak centered at zero residual (Fig. 3.8) and

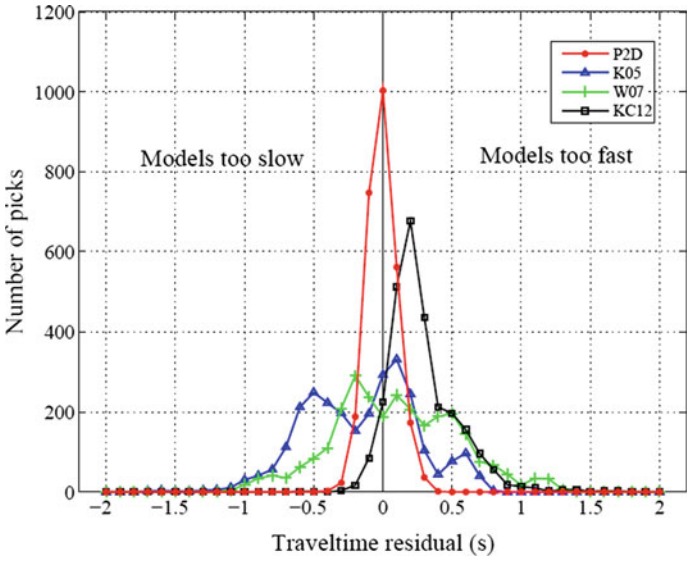

Fig. 3.8 Statistical distributions of travel time residuals from the first-arrival time picks in the northern Taiwan for our P2D models (*red* curve) and the other 3D tomography models, K05 (*blue* curve), W07 (*green* curve), and KC12 (*black* curve). See Fig. 3.5 for detailed description of colored symbols and the counts of the number of picks

Table 3.2 Statistical comparison of the residuals of first-arrival time predictions by the four models relative to observations for the profiles in northern Taiwan

	Mean	RMS	VAR*
P2D	−0.007	0.10	0.01
K05	−0.15	0.43	0.16
W07	0.09	0.46	0.20
KC12	0.28	0.36	0.06

*VAR variance of the residuals

the smallest RMS (Table 3.2). All three tomography models have higher-than-actual velocity in western tablelands which primarily causes the positive residuals, whereas the negative residuals are mostly induced by near surface layers with lower-than-actual velocity beneath eastern Ranges.

As shown in Fig. 3.7a, a collection of the P2D models in the small area of northern Taiwan give us a very clear hint at the lateral structural variations. These densely distributed 2D profiles that crisscross northern Taiwan enable us to construct a local 3D velocity model with sufficient resolution.

3.4 3D Model of Northern Taiwan

Northern Taiwan encompasses the greater Taipei metropolitan area with a high population density and is vulnerable to potential natural disasters such as earthquakes and volcanic eruptions. It is thus vital for us to have good understanding of the detailed crustal structure, especially shallow part of the crust, which has significant effect on seismic ground motion and is thus important in earthquake risk assessment and mitigation. In the previous section, we have described the 2D seismic structures obtained from active-source first-arrival times along several island-wide transects in Taiwan as well as a number of shorter profiles in northern Taiwan. In addition to the excellent fit to the ground-truth travel time data and the more realistic strength of velocity perturbations, the densely-distributed crisscrossing 2D seismic profiles in northern Taiwan displayed in Fig. 3.7 hints at the possibility of an improved lateral resolution. Therefore, an immediate next step will be to use these P2D models as constraints to construct a 3D structural image in northern Taiwan.

Deriving a 3D model from a number of pre-determined 2D profiles is essentially an ensemble search or inversion process in which we seek to obtain the optimal wave speed at each point in 3D space using its relevant information provided by the 2D profiles. The partitioned two-step approach to build a 3D model from sets of 1D or 2D models is the gist of tomography in general and has been widely used in seismic tomography in particular (e.g. Nolet 1990; Meier et al. 1997; Simons et al. 1999; Legendre et al. 2012). In this study, we adopt the partition modelling approach (Denison et al. 2002; Stephenson et al. 2006; Bodin et al. 2009; Dettmer et al. 2010), which allows us to obtain a smooth and stable 3D model with no need to impose additional regularization.

3.4.1 Partition Modelling Tomography

Partition modelling was initially developed for effectively solving nonlinear regression and classification problems (Denison et al. 2002) and has been successfully utilized in biological analysis, disease mapping and applications in a variety of Earth science disciplines (Stephenson et al. 2006; Bodin et al. 2009; Dettmer et al. 2010). Bodin et al. (2009) first applied this strategy to the 2D travel time tomography in which the unknown seismic velocity model is discretized by a given number of non-overlapping polygonal patches (a.k.a. Voronoi cells) whose sizes and boundaries can self-adjust to account for the variability in data coverage and model resolution. The final structure is inferred from an ensemble average over a large set of sample models generated by an efficient 2D Markov chain Monte Carlo method (Green 1995; Gilks et al. 1996). It is inherently smooth and stable as a result from averaging out incoherent features between the models with different parameterizations.

The implementation of our 3D model in northern Taiwan follows a procedure akin to the one presented in Bodin et al. (2009). Given a number of control points (a.k.a. Voronoi nuclei) randomly distributed in the study area, the P-wave velocity field at a fixed depth is partitioned into Voronoi cells, each of which encloses a single nucleus as shown in Fig. 3.9. The borders of each Voronoi cell are defined by the perpendicular bisectors of the lines connecting adjacent pairs of nuclei (Okabe et al. 2000). In our implementation, when drawing samples from the whole space of partitioned models, the locations of the Voronoi nuclei are random while the total number of the nuclei is determined based upon the distribution of the available P2D profiles and unchanged between samples. Since each of the P2D models is composed of multiple segments of depth-dependent 1D models, we allocate the Voronoi nuclei independently in individual segments and maintain one control point in every 10 km interval along the profile to ensure a good lateral resolution. Then the location of each Voronoi nucleus is chosen randomly within its interval along the profile and over an azimuthal range of $\pm 10^{\circ}$ across the profile to account for the sensitivity of the seismic waves in the transverse direction. The velocity in each Voronoi cell is assumed homogeneous with a value determine by taking the weighted average of the velocities of all the P2D profiles passing through the cell. The reliability and resolution of the resulting model will rely on the quality and distribution of the P2D models, and increasing the number of control points will only lead to heavier computational load. Figure 3.9 illustrates one realization (sample) of the partitioned model at a depth of 1.12 km.

3.4.2 Stabilization of the Ensemble Average Model

In the partition modelling process, the model space is sampled by a growing number of random realizations of the partitioned models. In each realization, with

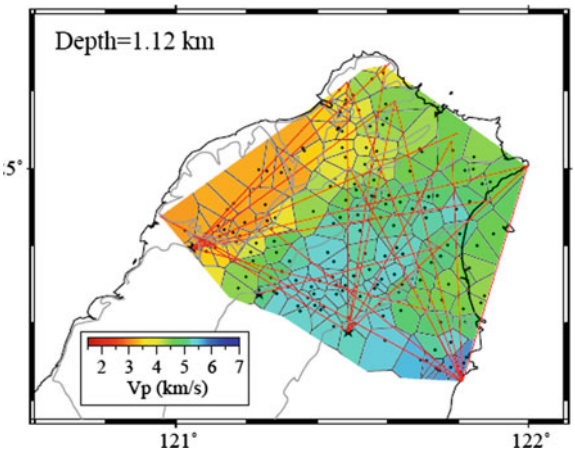

Fig. 3.9 An example of one realization randomly drawn from the partitioned models. The study region is partitioned horizontally into Voronoi cells according to a given number of randomly-generated nuclei (*black* dots). The sizes and borders of the cells are delineated by the perpendicular bisectors of the lines connecting adjacent pairs of nuclei. The velocity in each cell is assumed homogeneous and determined by a weighted average of all the P2D profiles passing through the cell (*red* lines)

the random Voronoi cells set up and the model sample (such as the one in Fig. 3.9) determined, we compute the point-wise average of the velocities over the ensemble of all the realized model samples. Such an ensemble average tends to vacillate in the initial few realizations when the number of model samples is small. However, as the realizations continue, the vacillation becomes weaker and the ensemble-averaged model stabilizes. Figure 3.10a displays the variation of the RMS between two ensemble-averaged models in the N-th and $(N-1)$-th (consecutive) realizations. The RMS value decreases with N and eventually approaches zero for sufficiently large N, indicating that the 3D partitioned model from the ensemble average becomes stable. In Fig. 3.10b–d, we can also observe the change in the spatial pattern of the difference between two consecutive ensemble-averaged models as the number of realizations increases. For a relatively small value $N = 12$ (Fig. 3.10b), the point-wise differences in velocity between the current and previous ensemble-averaged models are obvious, and are particularly large near the structural boundaries and in the transition zones between the slower western and faster eastern regions. With the number of realizations increases, the discrepancies in the areas with sharp velocity contrasts gradually diminish, indicating that the ensemble-averaged models obtained from two consecutive partitioned model realizations are nearly identical and converge to the optimal 3D model. The RMS of the differences in the ensemble-averaged models between $N = 12$ and $N = 11$ realizations is about 0.02 km/s (Fig. 3.10b), whereas after 100 realizations the RMS value has reduced to about 0.002 km/s (Fig. 3.10c). Taking both model stability and computational

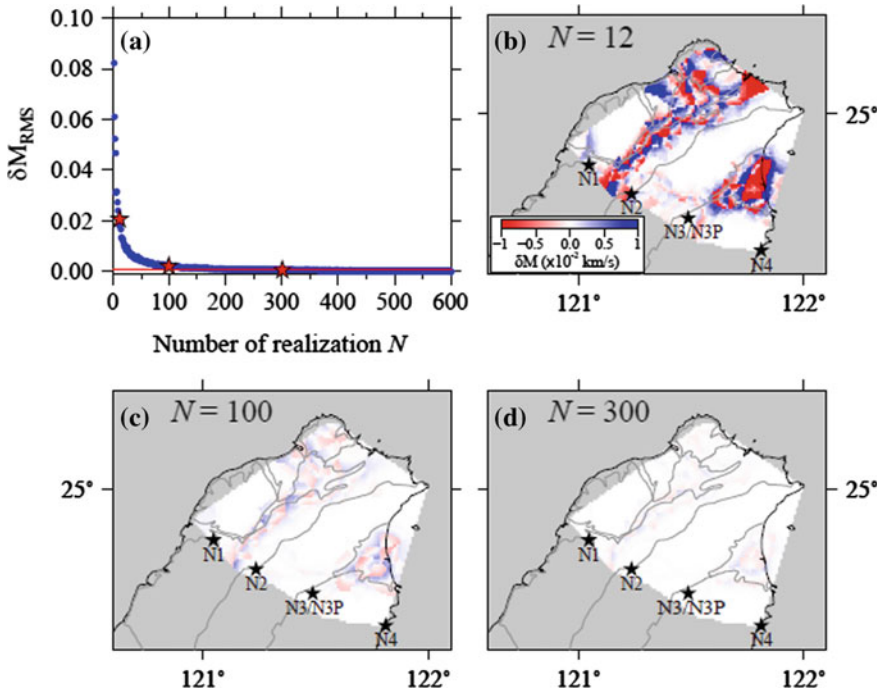

Fig. 3.10 Stability test of the ensemble averaged models. The final model is obtained from the ensemble average over all the realizations of partitioned models. As the number of realizations N increases, the ensemble-averaged model becomes stabilized. **a** The RMS of the differences of the ensemble-averaged velocities (δM_{RMS}) between two consecutive realizations as a function of the number of realizations. The RMS value approaches zero for large N, indicating that the ensemble-averaged model converges to a stable 3D model for northern Taiwan. The lateral variations of the point-wise differences in the velocities between the models drawn with two consecutive realizations are displayed in (**b**), (**c**) and (**d**) for increasing numbers of realizations, N = 12, 100, and 300, respectively. As the ensemble average model stabilizes, the difference becomes smaller. Considering both efficiency and stability, we choose the model with 300 realizations, i.e., N = 300

efficiency into account, we set the threshold of the RMS value at 0.001 km/s which corresponds to a realization number of about 300 (Fig. 3.10d). We therefore choose N = 300 in all our subsequent partition modelling calculations.

3.4.3 Resolution Tests

In our partition modelling tomography for northern Taiwan, the lateral resolution in the resulting 3D model depends heavily on the quality as well as the actual distributions of the P2D models. Therefore, it is important to verify the resolving

capability afforded by the P2D models available to us. For this purpose, we conduct a series of resolution tests using three different models as input, including the two tomography models, K05 and W07, and a third one designed according to local geology zonation. The tests start with extracting from the 3D models K05 and W07 the velocities in the same 2D vertical slices as our P2D profiles, which are then used as predetermined constraints to obtain the ensemble-averaged model by partitioned modelling.

The input and recovered structures at the top layer are illustrated in Fig. 3.11. The P-wave speed of the top layers in K05 (1 km depth) and W07 (0 km depth) are extracted (Fig. 3.11a and c). The model in Fig. 3.11e is designed according to the geological divisions in the region (Fig. 3.1). The input P2D models for the tests are obtained by first sampling the structures in Fig. 3.11a, c, e at the locations of our available P2D profiles and then averaging horizontally over individual 1D segments. Following the same partitioned modelling procedure as previously described and carrying out 300 realizations for each input model, we obtain the recovered ensemble-averaged models. Results in Fig. 3.11 show that the lateral variations in both tomography models K05 and W07 can be well-recovered with the available P2D profiles in northern Taiwan. Small-scale features in W07 near the edges of the study region are not fully recovered due to a lack of 2D profiles. On the other hand,

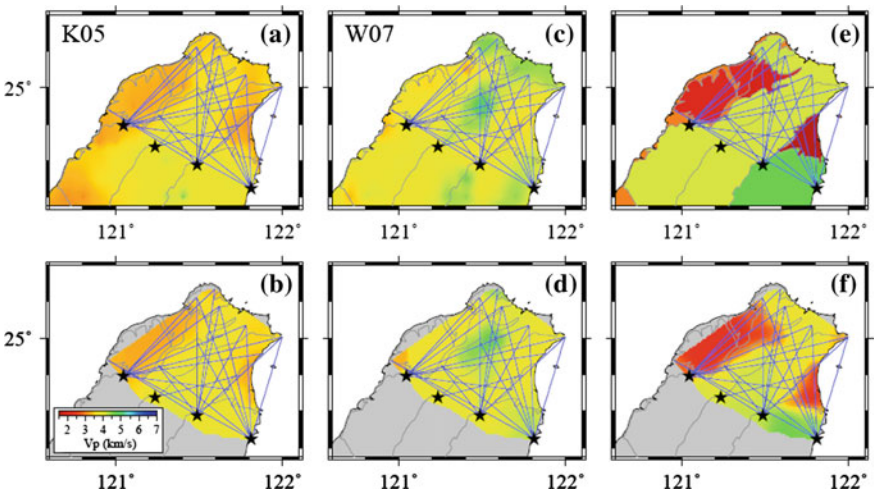

Fig. 3.11 Resolution tests of the ensemble-averaged 3D models in which the two tomography models, K05 and W07, and a synthetic model based on geological zonation are used to extract input structures along the available P2D profiles (*blue* lines) across northern Taiwan. The maps in (**a**), (**c**), and (**e**) show respectively the lateral velocity variations at the top layer for the three test models used to predetermine the P2D models as inputs in partition modelling test, while those in (**b**), (**d**), and (**f**) display the recovered models obtained from the ensemble averages of 300 realizations of model samples. *Gray* shaded area indicates region with no resolution. These tests demonstrate that with the constraints from the available 2D profiles crisscrossing northern Taiwan, we are able to construct a 3D model with sufficient resolution, and the geological boundaries can be well-preserved from the ensemble average of partitioned models

most of the geological boundaries in northern Taiwan can be well-preserved and the strengths of lateral velocity perturbations can be retrieved up to 80% of the initial values (Fig. 3.11f). These resolution tests give us confidence in using our P2D models to construct realistic and robust images for the structures in the shallow crust beneath northern Taiwan.

3.4.4 3D Model for Northern Taiwan

Using the available P2D seismic profiles, we obtain a 3D model for the shallow crustal structure in northern Taiwan, by the partition modelling approach. The map views of the obtained 3D structure at a variety of depths are displayed in Fig. 3.12. The maximum depth of resolution by our partitioned modelling 3D model (hereafter referred to as PM3D) is about 15 km, as indicated by the maximum penetration depths of the ray paths used in obtaining the P2D profiles. As the number of ray paths decreases with depth, so does the resolution. As a result, the lateral resolution in model PM3D degenerates with depth. A distinct change in P-wave speed between the CP and the WF can still be seen at the depth of about 10 km, whereas at 14 km depth there is little lateral variation in the resulting 3D model. As opposed to the nearly homogeneous structure at depth greater than 10 km, model PM3D displays very large lateral variations near the surface, where significant low- and high-velocity anomalies exist in the western and eastern parts of northern Taiwan, respectively. Furthermore, the laterally-varying velocity patterns in PM3D show a good correlation with the structural boundaries, indicating that our P-wave model truthfully accounts for the structural effects of different geological zonations on the observed first-arrival times.

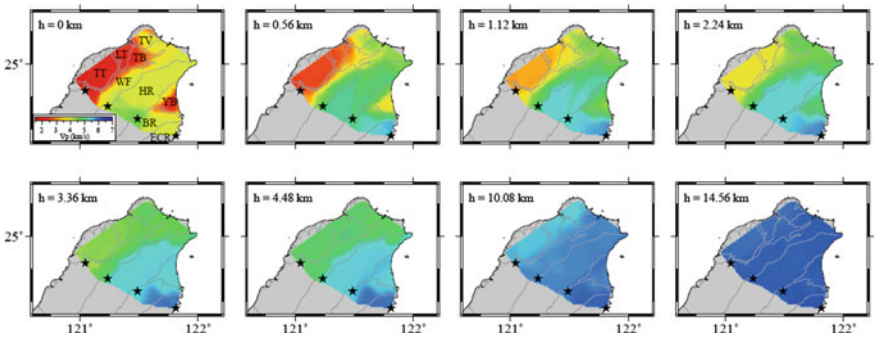

Fig. 3.12 Map views of the resulting 3D model (PM3D) from partitioned modelling at depths of 0, 0.56, 1.12, 2.24, 3.36, 4.48, 10.08, and 14.56 km. *Gray* lines indicate the geological boundaries. The velocities are plotted with the same color scale shown in the first panel. The lateral velocity perturbations are very large near the surface, with a spatial pattern of variation in good agreement with the structural boundaries. Due to the shorter lengths of the profiles, the depth resolution only extends down to 15 km, where the model has little lateral variation

3.4.5 Correlation with Tectonic Provinces

There is an excellent correlation between the velocity pattern in our PM3D model and the geological provinces in northern Taiwan, as illustrated by the slow region associated with the foothills (WF) and tablelands (LT and TT) in the west and the fast region corresponding to the ranges (HR, BR and ECR) in the east. The Taipei and Yilan Basins (TB and YB) also show up as slow anomalies at shallow depth. The Taiwan Island is a product of a relatively young active orogeny where a basement of the pre-Tertiary metamorphic complex is overlain by the deposits of the post-Tertiary sediments (Ho 1988). The metamorphic rocks, originally buried deep, are now exposed at or near the surface in the eastern ranges, leading to the high velocity anomalies in the subsurface structure. The highest P-wave speed at the surface occurs in the western Central Range (including HR and BR) of north Taiwan, where the metamorphic deposits between the Eocene and Miocene are exposed. The pre-Tertiary basement, metamorphosed sedimentary and volcanic rocks, were uplifted in the ECR during the early Pleistocene orogeny (Yui et al. 1990). As a result, the ECR has the highest P-wave speed at shallow depths. To the west of the ranges, the Oligocene to Pleistocene rocks have been severely deformed by folding and faulting, leading to a lower wave speed in the WF than the metamorphosed rocks in the east. The even more recent unconsolidated deposits of lateritic and non-lateritic gravels in the tablelands resulted in even lower speeds as seen in the LT and TT today. Near the northern tip of Taiwan, the Quaternary Tatun volcano group (TV), which erupted during the Pliocene to Pleistocene (Chen and Wu 1971; Song et al. 2000), mainly comprises andesitic and dacitic rocks that give rise to the fast velocity anomaly at shallow depth. The Taipei Basin (TB) is underlain with the deformed Tertiary basement superimposed by Holocene alluviums (Teng et al. 2001) and characterized by a pronounced low velocity anomaly, whereas the Yilan Basin (YB) is situated at the western end of the Okinawa Trough which belongs to a back-arc spreading zone in the Ryukyu subduction system. Likewise, the underlying Eocene-Miocene basement filled with Holocene alluviums mostly composed of unconsolidated silts and gravels also leads to a shallow, low wave-speed structure. As shown in Fig. 3.12, both the laterally and vertically varying structures of high and low velocities in our PM3D model are remarkably consistent with the geological features and tectonic history of northern Taiwan.

3.4.6 Comparisons with Three Recent Tomography Models

In Fig. 3.13, we compare our PM3D model in northern Taiwan with the three recent tomography models. At shallow depth, the overall P-wave speed in model K05 is lower, and the lateral velocity variations from the west to east are relatively weak. There are more small-scale anomalies present in model W07, and their locations are largely uncorrelated with surface geological features. Model KC12 yields the

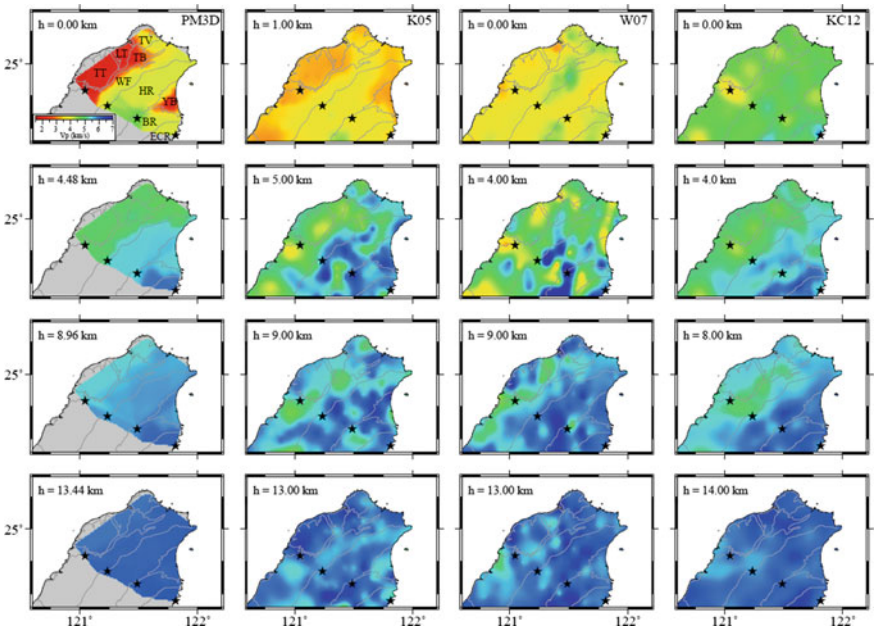

Fig. 3.13 The PM3D model derived from the ensemble average over 300 realizations. The lateral variations at four depths, 0, 4.48, 8.96, and 13.44 km are shown in the first column. The three recent tomography models, K05, W07, and KC12, are shown at similar depths in the other three columns as comparison. The velocities are plotted with the same color scale shown in the first panel. The patterns of velocity structures are very different near the surface between the models but become more consistent at greater depths

smoothest structure in this region, with an overall higher velocity than the other models. It is obvious that the near-surface velocities resolved from the three recent tomography models are not low enough in the LT and TT in northwest Taiwan. Except for the surface layer in the western tableland regions and the two basins covered with sedimentary deposits, Model KC12 shares the highest similarity with our PM3D model. The other two models, K05 and W07, although showing similar large-scale features, namely a region of slow anomaly in the west and fast anomaly in the east, their lateral variations near the surface are too weak, and the numerous small-scale heterogeneities are also inconsistent with the geological divisions and may be artificial. This comparison clearly demonstrates that the tomography models, obtained from a regularized inversion of the travel times of body-wave phase arrivals, underestimate the strength of velocity perturbations. As an alternative, the partitioned modelling approach uses the P2D models derived by maximizing the fit to the ground-truth first-arrival times as a basis to build a 3D model. The ensemble averaging over random realizations of the partitioned modelling samples allows us to obtain a smooth and robust 3D model for the shallow crustal structure without any explicit regularization.

3.5 Conclusion

The ground-truth data obtained from the TAIGER active-source experiments provide excellent and unique constraints on shallow crustal structures beneath Taiwan. By forward modelling and maximizing the fit to these highly accurate first-arrival times at very closely-spaced and almost linearly deployed stations, we are able to obtain the 2D seismic profiles along four transects across the island of Taiwan and 22 shorter profiles in northern Taiwan. The resulting seismic structures along these 2D profiles yield first-arrival time predictions that are in excellent agreement with the observations, and they display clear lateral variations with more realistic amplitudes of velocity perturbation and a spatial pattern consistent with geological zonations of Taiwan. The profiles across northern Taiwan shows strong lateral velocity contrast of nearly $\pm 30\%$ between the western tablelands and eastern ranges, also in good agreement with the near-surface geologic expressions.

Taking advantage of the collection of densely-distributed crisscrossing 2D velocity profiles in northern Taiwan, we construct a smooth and robust 3D model with sufficient resolution based on the partition modelling approach. The velocity anomalies in the resulting PM3D model exhibit remarkable consistency with the geological features at the surface as well as the tectonic history of northern Taiwan. Comparison with three recent tomography models suggests that the amplitudes of high and low velocity anomalies in models obtained by travel time tomography are in general underestimated due to the inevitable tradeoff in regularized inversions. An important utility of our 3D model PM3D is to serve as an effective starting model in a high-resolution regularized tomography inversion using both active- and passive-source data.

In the next two chapters, we switch topic and focus on the development and application of 3D anisotropic tomography with full-wave approach.

References

Bodin T, Sambridge M, Gallagher K (2009) A self-parameterising partition model approach to tomographic inverse problems. Inverse Problems 25:055009

Červený V, Molotkov I, Pšenčík I (1977) Ray Method in Seismology. University of Karlova, Prague, Czechoslovakia

Chen CH, Wu YT (1971) Volcanic geology of the Tatun geothermal area, northern Taiwan. Proc Geol Soc China 14:5–28

Denison DGT, Holmes, CC, Mallick BK, Smith AFM (2002) Bayesian methods for nonlinear classification and regression. Wiley, New Jersy

Dettmer J, Dosso SE, Holland CW (2010) Trans-dimensional geoacoustic inversion. J Acoust Soc Am 128:3393–3405

Gilks WR, Richardson S, Spiegelhalter DJ (1996) Markov chain Monte Carlo in Practice. Chapman and Hall, London, UK

Green P (1995) Reversible jump MCMC computation and Bayesian model selection. Biometrika 82:711–732

Ho C-S (1988) An introduction to the geology of Taiwan: Explanatory text of the geologic map of Taiwan. Central Geological Survey, Ministry of Economic Affairs, Taipei, R.O.C., p 192

Kim KH, Chiu JM, Pujol J, Chen K-C, Huang B-S, Yeh Y-H, Shen P (2005) Three-dimensional *Vp* and *Vs* structural model associated with the active subduction and collision tectonics in the Taiwan region. Geophys J Int 162:204–220

Kuo-Chen H, Wu F, Roecker S (2012) Three-Dimensional P velocity structures of the lithosphere beneath Taiwan from the analysis of TAIGER and related seismic datasets. J Geophys Res

Legendre C.P, Meier T, Lebedev S, Friederich W, Viereck-Götte L (2012) A shear wave velocity model of the European upper mantle from automated inversion of seismic shear and surface waveforms. Geophys J Int 191(1):282–304. doi: 10.1111/j.1365-246X.2012.05613.x

Lin Y-P, Zhao L, Hung S-H (2011) Assessment of tomography models of Taiwan using first-arrival times from TAIGER active-source experiment. Bull Seism Soc Am 101(2):866–880. doi:10.1785/0120100244

Ma K-F, Wang J-H, Zhao D (1996) Three-dimensional seismic velocity structure of the crust and uppermost mantle beneath Taiwan. J Phys Earth 44:85–105

Meier T, Lebedev S, Nolet G, Dahlen FA (1997) Diffraction tomography using multimode surface waves. J Geophys Res 102:8255–8267

Nolet G (1990) Partitioned waveform inversion and two-dimensional structure under the network of autonomously recording seismographs. J Geophys Res 95:8499–8512

Okabe A, Boots B, Sugihara K, Chiu SN (2000) Spatial tessellations—Concepts and Applications of Voronoi Diagrams. 2nd edn. John Wiley, p 671. ISBN:0-471-98635-6

Olsen KB (1994) Simulation of three-dimensional wave propagation in the Salt Lake Basin, Ph.D. thesis, University of Utah, Salt Lake City, Utah, p 157

Rau R-J, Wu FT (1995) Tomographic imaging of lithospheric structures under Taiwan. Earth Planet Sci. Lett. 133:517–532

Roecker SW, Yeh YH, Tsai Y-B (1987) Three-dimensional P and S wave velocity structures beneath Taiwan–deep structure beneath an arc-continent collision. J Geophys Res 92:10,547–10,570

Simons Frederik J, Zielhuis Alet, van der Hilst Rob D (1999) The deep structure of the Australian continent from surface wave tomography. Lithos 48:17–43

Shin T-C, Chen Y-L (1998) Study on the earthquake location of 3-D velocity structure in the Taiwan area. Metoerol Bull 42:135–169

Song SR, Tsao ST, Lo HJ (2000) Characteristics of the Tatun Volcanic eruptions, northern Taiwan: Implications for a cauldron formation and volcanic evolution. J Geol Soc China 43:361–378

Stephenson J, Gallagher K, Holmes C (2006) Low temperature thermochronology and strategies for multiple samples 2: partition modelling for 2D/3D distributions with discontinuities. Earth Planet Sci Lett 241:557–570

Teng LS, Lee CT, Peng CH, Chen WF, Chu CJ (2001) Origin and geological evolution of the Taipei basin, northern Taiwan. Western Pac Earth Sci 1:115–142

Wang Z, Zhao D, Wang J, Kao H (2006) Tomographic evidence for the Eurasian lithosphere subducting beneath south Taiwan. Geophysical Reseach Letters 33:L18306. doi:10.1029/2006GL027166

Wu Y-M, Chang C-H, Zhao L, Shyu JBH, Chen Y-G, Sieh K, Avouac J-P (2007) Seismic tomography of Taiwan: improved constraints from a dense network of strong motion stations. J Geophys Res 112:B08312. doi:10.1029/2007JB004983

Yui T-F, Wu TW, Jahn BM (1990) Geochemistry and plate-tectonic significance of the metabasites from the Tananao Schist Complex of Taiwan. J Southeast Asian Earth Sci 4:357–368

Zelt CA, Ellis RM (1988) Practical and efficient ray tracing in two-dimensional media for rapid traveltime and amplitude forward modeling. Can J Geophys 24:16–31

Zelt CA, Smith RB (1992) Seismic traveltime inversion for 2-D crustal velocity structure. Geophys J Int 108:16–34

Chapter 4
Full-Wave Effects on Shear-Wave Splitting

In this chapter, we develop an approach to the inversion of 3D anisotropy structure using the sensitivity (Fréchet) kernels calculated by an efficient and flexible full-wave algorithm based on the normal-mode theory. Predictions of SKS splitting by these full-wave sensitivity kernels suggest a significant bias in ray-theory treatment caused by the unaccounted interference between the SKS wave and other contaminating phases with similar arrival times. The full-wave sensitivity kernels accurately account for all the interactions of multiple phases for a wide spectrum of source-receiver geometry.

4.1 Introduction

Knowledge on the Earth's anisotropic structure allows us to characterize the deformation and the dynamic processes in the Earth's interior. Shear-wave splitting has been an important observable in the investigation of elastic anisotropy in the crust and upper mantle. Up to the recent past, the interpretation of shear-wave (SKS and/or SKKS) splitting in terms of anisotropy has primarily relied on ray theory under the approximation of a single plane shear wave with nearly vertical incidence angle. Under this scenario, all shear-wave splitting measurements at a given station are reduced to two apparent anisotropy parameters: the splitting time δt between fast and slow quasi-shear waves and the azimuth ϕ_f of the fast axis (the polarization of the fast quasi-shear wave), through a sinusoidal relation:

$$S_i = \delta t \, \sin 2(\phi_f - \phi_b^i), \tag{4.1}$$

Originally published in [Geophysical Research Letters Feb 2014 vol. 41 799-804]. Published with kind permission of © 2014. American Geophysical Union. All Rights Reserved.

Y.-P. Lin, *Isotropic and Anisotropic Seismic Tomography Using Active Source and Earthquake Records*, Springer Theses, DOI 10.1007/978-981-10-5068-8_4

where S_i is the shear-wave splitting measurement at the i-th station whose back-azimuth is ϕ_b^i. The pair of apparent anisotropy parameters then prescribes a uniform layer of anisotropy beneath the station, and the amount of splitting varies with the differential angle $\phi_f - \phi_b^i$ only.

The simple relation in Eq. (4.1) provides a clear and practical approach to the interpretation of shear-wave splitting measurements, and it has been widely applied in studying upper mantle anisotropy (e.g. Ando 1984; Vinnik et al. 1984; Silver and Chan 1988; Silver 1996; Savage 1999; Wüstefeld et al. 2008). However, the assumption of a vertically incident plane wave precludes the resolution of the spatial variation of anisotropy by shear-wave splitting, and the requirement of a single (i.e. isolated) SKS or SKKS wave severely limits the source-station geometry amenable for making splitting measurements.

Chevrot (2000) demonstrated that the optimal measurement of shear-wave splitting in Eq. (4.1), which has since been referred to as the *splitting intensity* (SI), can be obtained by projecting the transverse-component signal onto the time-derivative of the radial-component signal. That recognition enabled Favier and Chevrot (2003) and Favier et al. (2004) to derive the expression for the three-dimensional (3D) sensitivity (Fréchet) kernels of the SI to elastic anisotropic structural parameters. These 3D kernels for the SI were later used by Monteiller and Chevrot (2011) to image the crust and upper-mantle anisotropy in southern California. Sieminski et al. (2008) examined the 3D kernels for the SI using the accurate but numerically demanding adjoint spectral-element method (Tromp et al. 2005; Liu and Tromp 2006), and pointed out the neglected dependence on the incidence angle of SKS wave in the 3D sensitivity kernels of Favier and Chevrot (2003) and Favier et al. (2004). It should be pointed out, however, that Chevrot (2006) has extended their 3D sensitivity kernels to the case of non-vertically incident SKS waves.

In this study, we adopt the more efficient approach of Zhao and Chevrot (2011a, b) for calculating full-wave Fréchet kernels to conduct a thorough and detailed investigation on the 3D sensitivity of the SI to anisotropic structure. We demonstrate that the SI measurements at a given station are affected by not only the back-azimuth of the SKS wave, but also its incidence angle due to variations in epicentral distance and source depth, and the interference between the SKS wave and neighboring phases. As a result, our full-wave kernels enable us to conduct 3D tomography inversions of the anisotropic structure using the SI measurements obtained from a much wider range of source-station geometry.

4.2 Full-Wave Sensitivity of Splitting Intensity to Anisotropy

As shown in Chevrot (2000), the SI measured at a station with recorded radial- and transverse-component signals $u_R(t)$ and $u_T(t)$, respectively, can be expressed as (e.g. Favier and Chevrot 2003; Chevrot 2006; Sieminski et al. 2008):

$$S = -2\frac{\int_{t_1}^{t_2} \dot{u}_R(t) u_T(t) dt}{\int_{t_1}^{t_2} [\dot{u}_R(t)]^2 dt}, \tag{4.2}$$

where the integrals are taken over the time window $[t_1, t_2]$ selected for each shear-wave phase of interest, and the dot above $u_R(t)$ indicates its time-derivative. The interpretation or modelling of the SI data in terms of anisotropy is enabled by the so-called sensitivity or Fréchet kernels through the integral relationship

$$\begin{aligned} S = \int_0^a \left\{ \int_0^\pi \int_0^{2\pi} \left[K_\varepsilon^S(r,\theta,\varphi)\varepsilon(r,\theta,\varphi) + K_\delta^S(r,\theta,\varphi)\delta(r,\theta,\varphi) \right.\right. \\ \left.\left. + K_\gamma^S(r,\theta,\varphi)\gamma(r,\theta,\varphi) \right] r^2 \sin\theta \, d\theta \, d\varphi \right\} \mathrm{d}r, \end{aligned} \tag{4.3}$$

where $(r,\ \theta,\ \varphi)$ is an arbitrary location in the Earth of radius a. $\varepsilon = (C_{11} - C_{33})/2\rho\alpha^2$, $\delta = (C_{13} - C_{33} + 2C_{44})/\rho\alpha^2$, and $\gamma = (C_{66} - C_{44})/2\rho\beta^2$ are dimensionless anisotropy parameters (Mensch and Rasolofosaon 1997; Becker et al. 2006; Chevrot 2006). Here ρ is density, α and β are respectively the isotropic P- and S-wave velocities in the reference model, and C_{ij} are the elements of the elasticity tensor in the Voigt notation (Babuška and Cara 1991; Browaeys and Chevrot 2004).

Equation (4.2) tells us how the SI is measured from radial- and transverse-component waveforms. The expression is remarkably similar to that for a finite-frequency travel time shift (delay) between recorded and synthetic seismograms measured by their cross-correlation (e.g. Eq. (18) in Zhao and Jordan 1998; Eq. (66) in Dahlen et al. 2000). This suggests an alternative interpretation of the causal effect between anisotropy structure and the SI, analogous to that between velocity perturbation and delay time: The transverse-component signal $u_T(t)$ can be viewed as energy scattered from the radial-component signal $u_R(t)$ by anisotropy parameters ε, δ and γ, and the SI is merely the finite-frequency delay time of $u_T(t)$ relative to $u_R(t)$. Therefore, we can expect to see the SI kernels displaying the banana-doughnut features similar to the finite-frequency travel time kernels with zero sensitivity along the ray path (e.g. Dahlen et al. 2000; Zhao et al. 2000).

Zhao and Chevrot (2011a, b) proposed the expressions for the Fréchet kernels of widely used observables in seismic tomography with respect to various of model parameters in terms of the strain Green tensors (SGT). That approach affords both efficiency and flexibility in the calculation of full-wave Fréchet kernels with the help of SGT databases obtained by accurate wavefield modelling algorithms such as the normal-mode theory for one-dimensional (1D) models or numerical simulations for 3D models. Figure 4.1 shows the 3D SI kernels for γ with several source-receiver geometries for the Preliminary Reference Earth Model (PREM) (Dziewonski and Anderson 1981). The spatial pattern of the SI sensitivity to γ changes dramatically with back-azimuth and epicentral distance. For instance, the pattern of the SKS kernel at 100° distance for different azimuths (Fig. 4.1a–h) is

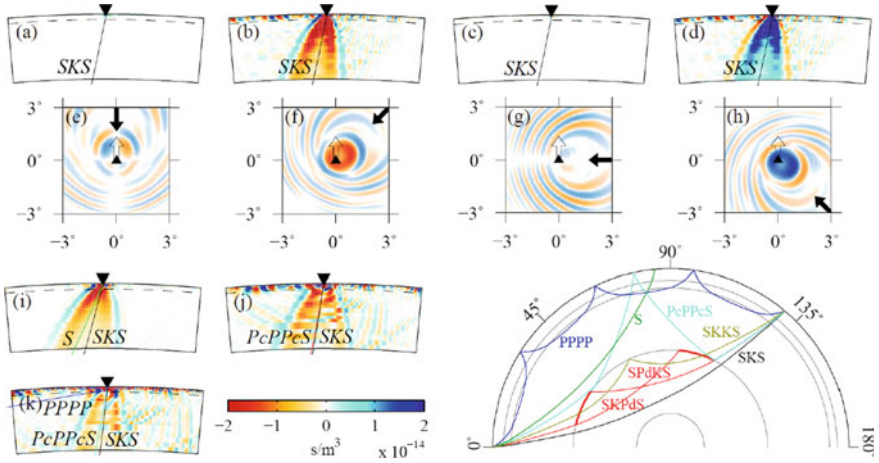

Fig. 4.1 Full-wave Fréchet kernels of the splitting intensity SI for shear-wave anisotropy parameter γ with different source-receiver geometries. These are sensitivities of the SI of the signals in the SKS time window (shaded region in Fig. 4.2b) to γ. The source is always at the surface. The kernels are shown in the source-receiver great-circle plane (**a**–**d** and **i**–**k**) and in map view at 200 km depth (**e**–**h**). In all examples, the fast axis of anisotropy is north-south, i.e. $\phi_f = 0°$, shown by the open arrows in map view plots (**e**–**h**). The paired plots (a,e), (b,f), (c,g) and (d,h) correspond to the incident shear waves at the same epicentral distance of 100° but different back-azimuths ϕ_0 of 0°, 45°, 90° and 135°, respectively, shown by the black arrows in map view plots (**e**–**h**). The kernels for the back-azimuths of 0° (a,e) and 90° (c,g) are weak with negligible integrated sensitivities, whereas those for the back-azimuths of 45° (b,f) and 135° (d,h) are strong with opposite signs. In (i), (j) and (k), the epicentral distances are 85°, 115° and 130°, respectively, while the back-azimuths are all 45°. At these distances, the kernels are more complex due to stronger interference of SKS with other phases. Ray paths for the relevant phases are shown in the bottom-right plot. Reprinted from Lin et al. (2014a) with permission Geophysical Research Letters

similar to that predicted by ray theory, i.e., a simple sinusoidal variation with the differential angle $\phi_f - \phi_b$ as in Eq. (4.1).

Synthetic seismogram calculated for the same distance (Fig. 4.2) indicates that SKS is the dominant phase arriving in the estimated SKS window (shaded zone in Fig. 4.2b). Thus, all the kernels in Fig. 4.1a–h display a single, simple banana-doughnut shape. At distances of 85°, 115° and 130°, however, the sensitivities for the signals in the SKS window are more complex due to increased interference with other phases. At the distance of 85°, a strong mantle-turning S wave (green line in Fig. 4.2b) arrives right at the tail of SKS, making the separation of the two phases impossible. This leads to the broadening of the calculated kernel shown in Fig. 4.1i. At 115°, the phases SPdKS/SKPdS with diffractions along the core-mantle boundary (CMB) and the twice CMB-reflected PcPPcS arrive closely in time to a relatively weak SKS, leading to a stronger interference effect and a more chaotic pattern in the kernel (Fig. 4.1j). Similarly at 130°, contribution from the surface-reflected PPPP makes the kernel even more complicated (Fig. 4.1k).

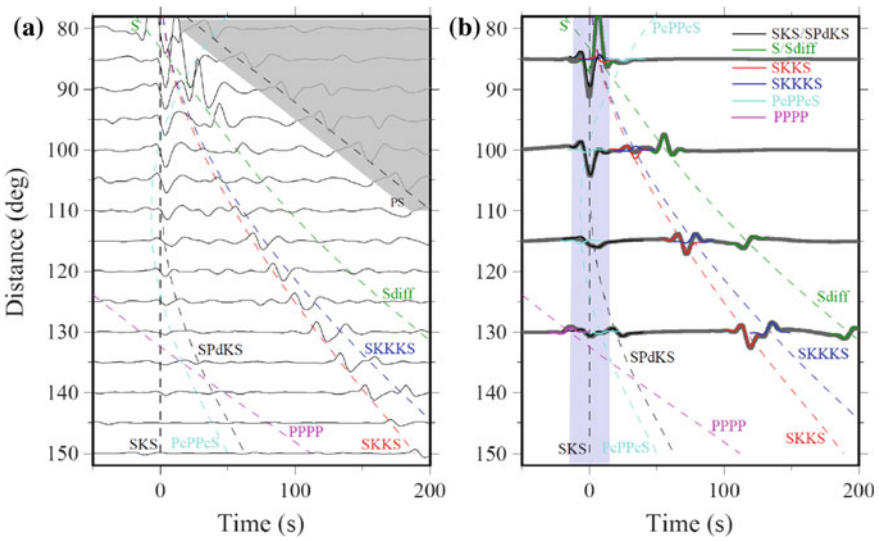

Fig. 4.2 **a** Synthetic seismograms calculated by normal-mode summations in 1D model PREM for epicentral distances between 80° and 150° with an interval of 5°. The sources are all at the surface. All waveforms have been band-pass filtered between 0.008 and 0.12 Hz, and are aligned at $t = 0$ by the predicted SKS arrival times. To avoid distraction by the large-amplitude surface waves, the amplitudes of the waveforms in the shaded zone have been divided by the factor $3\Delta^2$, where Δ is the epicentral distance. **b** Synthetics for individual phases (*thin lines*) calculated by the WKBJ method (Chapman et al. 1988) at the distances of 85°, 100°, 115° and 130°. *Thick lines* are the summation of the individual waveforms. Shaded zone indicates the SKS time window $[t_1, t_2]$ used in the calculation of the kernels in Fig. 4.1. *Thin dashed lines* in (**a**) and (**b**) are travel-time curves for model PREM calculated by the TauP Toolkit (Crotwell et al. 1999). Reprinted from Lin et al. (2014a) with permission Geophysical Research Letters

The effect of these interferences can be seen more clearly when we integrate these 3D kernels for a suite of differential angles $\phi_f - \phi_b$ and compare with the simple relation predicted by Eq. (4.1).

4.3 Full-Wave Effects on SKS Splitting Intensity

As discussed earlier, the simple sinusoidal dependence of the SI on the differential angle $\phi_f - \phi_b$ in Eq. (4.1) is based on the assumption of a single vertically incident plane SKS wave. Therefore, its validity hinges on whether the SKS phase in the time window for measuring the SI is contaminated by other phases. The waveforms in Fig. 4.2b suggest that in the distance ranges of 80°–90° and 110°–130° SKS may be affected by other phases. To quantify the interference effect on the SKS splitting intensity, we integrate the 3D sensitivity kernels assuming a uniform anisotropy of $\gamma = -0.02$ in the top 250 km depth range for a suite of differential angles $\phi_f - \phi_b$

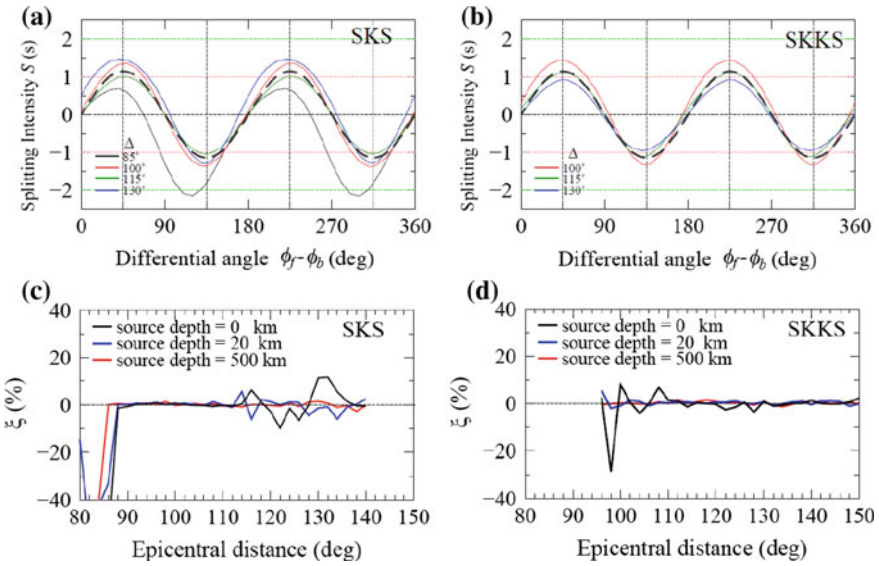

Fig. 4.3 **a** Splitting intensity predictions of SKS as functions of the differential angle $\phi_f - \phi_b$ assuming a uniform anisotropy of $\gamma = -0.02$, $\varepsilon = -0.0189$, and $\delta = -0.0096$ in the top 250 km layer. Solid lines show predictions by the full-wave 3D kernels for surface sources at four epicentral distances (*black*: 85°; *red*: 100°; *green*: 115°; *blue*: 130°). The dashed line is the prediction by the simple relation $S = \delta t \sin 2(\phi_f - \phi_b)$, where $\delta t = 1.15$ s, corresponding to $\gamma = -0.02$. **b** Same as (**a**) but for SKKS at epicentral distances of 100°, 115° and 130°. Variations of the shifting parameter ξ defined in Eq. (4.4) with distance for **c** the SKS time window, and **d** the SKKS time window. Black, blue and red lines are for source depths at 0, 20 and 500 km, respectively. Reprinted from Lin et al. (2014a) with permission Geophysical Research Letters

and compare them with those predicted by the ray-theoretical relation in Eq. (4.1). The result is shown in Fig. 4.3. In obtaining the full-wave SI predictions, contributions from ε and δ are accounted for by adopting the scaling relations among the anisotropy parameters (Becker et al. 2006), i.e. $\varepsilon = -0.0189$ and $\delta = -0.0096$. Zhao and Chevrot (2011b) showed that the sensitivity kernels of the SI for ε and δ are approximately an order of magnitude smaller than that for γ. As a result, the contributions to the SI predictions by ε and δ amount to only 4 and 9.5% of that by γ, respectively.

The prediction of $S = \delta t \sin 2(\phi_f - \phi_b)$ for a single plane SKS or SKKS wave with vertical incidence is a simple sinusoid (black dashed lines in Fig. 4.3a, b), reaching peak values of $\pm\delta t$ at the differential angles $90° \mp 45°$ and $270° \mp 45°$. The predictions from the 3D kernels, however, are quite different depending on the epicentral distance. These 3D kernels are calculated by the accurate normal-mode theory which fully accounts for the interference of all possible waves arriving in the time window used to measure the SI. Also included in these full-wave 3D kernels but neglected in ray theory are the near-field effect in the vicinity of stations and the complex wavefield interactions with near-surface discontinuities.

Since the ray-theoretical curve (dashed sinusoids in Fig. 4.3a, b) has a zero mean, we can use the vertical shifts of the other curves to assess the full-wave effect on the SI predictions. Thus for a given prediction curve we define a shifting parameter

$$\xi = (S_{\max} + S_{\min})/\max(|S_{\max}|, |S_{\min}|), \tag{4.4}$$

where $S_{\max}$ and $S_{\min}$ are respectively the maximum and minimum of a given curve. $\xi = 0$ corresponds to a zero-mean curve, while $\xi > 0$ indicates a positive shift, and vice versa. The shifting parameters are shown in Fig. 4.3c, d for a suite of epicentral distances and for source depths of 0, 20 and 500 km. The pattern is consistent with what we have seen in Fig. 4.2b: $\xi \approx 0$ in the distance range of $\sim$88°–115° in which the SKS is not significantly affected by the interference with other phases (Fig. 4.3c). For distances less than $\sim$88°, there is a large negative shift caused by a strong interference with the mantle-turning S wave which has a very different incidence angle.

As seen in the prediction for 85° distance (black solid curve in Fig. 4.3a), not only are there a negative shift in the SI, but also a shift in the differential angle $\phi_f - \phi_b$. This implies that if one were to use the SI obtained from an earthquake at an epicentral distance of 85°, there would be biases in both splitting time δt and the azimuth of the fast axis ϕ_f. Beyond $\sim$115° the pattern is more complicated because of contributions from interfering phases such as SPdKS/SKPdS, PcPPcS and PPPP. The interference effect becomes weaker for deeper sources. For SKKS (Fig. 4.3d), which is also often used to measure shear-wave splitting, the interference effect is significant only for very shallow sources at distances less than $\sim$100°.

The predictions in Fig. 4.3a, b also show clear discrepancy between the splittings of SKS and SKKS, especially at larges epicentral distances. The reason is obvious: the SKS and SKKS are affected at different distances and by different neighboring phases (Fig. 4.2). The SKS-SKKS splitting discrepancy has been observed and interpreted in terms of complex anisotropy in the D″ region (e.g. Long 2009). Our full-wave result suggests that upper-mantle anisotropy can also contribute to SKS-SKKS splitting discrepancy.

The near-field effect can be clearly seen in the SI prediction for Δ = 100° (*red* curve in Fig. 4.3a). Although it has nearly zero shift (Fig. 4.3c) owing to stronger SKS wave amplitude relative to other interfering phases, the amplitude of the predicted splitting intensity is very different from the ray-theoretical one (black dashed curve) with a discrepancy of $\sim$0.3 s ($\sim$26%) in the estimation of splitting time δt. This is mostly due to the near-field effect and the multiple reflections from near-surface discontinuities as illustrated by the highly concentrated and rapidly oscillating sensitivity (Fig. 4.1b, d) in the vicinity of the station. The effect of these full-wave behaviors can also be seen in the depth-varying (i.e. one-dimensional) sensitivities of splitting intensity for γ as shown in Fig. 4.4 obtained by horizontally integrating the 3D kernels (i.e., the quantity inside the curled bracket in Eq. (4.3) assuming a unity γ and ignoring negligible contributions from ε and δ). At depths in the mantle, the 1D kernels are more or less straight lines with little depth variation.

However, they fluctuate wildly near the surface as well as the mid-crust and Moho discontinuities as a consequence of the combined effects from a strong near-field complexity and the multiple reflections within the two crustal layers.

Favier and Chevrot (2003) demonstrated the near-field behavior of the finite-frequency SI kernel. Their result was, however, not fully representative of the SKS wave in a realistic Earth structure, since they assumed a homogeneous half-space velocity model. All the full-wave 1D kernels for different epicentral distances in Fig. 4.4 show some level of departure from the ray-theoretical kernel (black dashed lines). The full-wave kernel at 100° (red lines) follows the curve of the ray-theoretical kernel most closely in the mantle, but has a much larger value

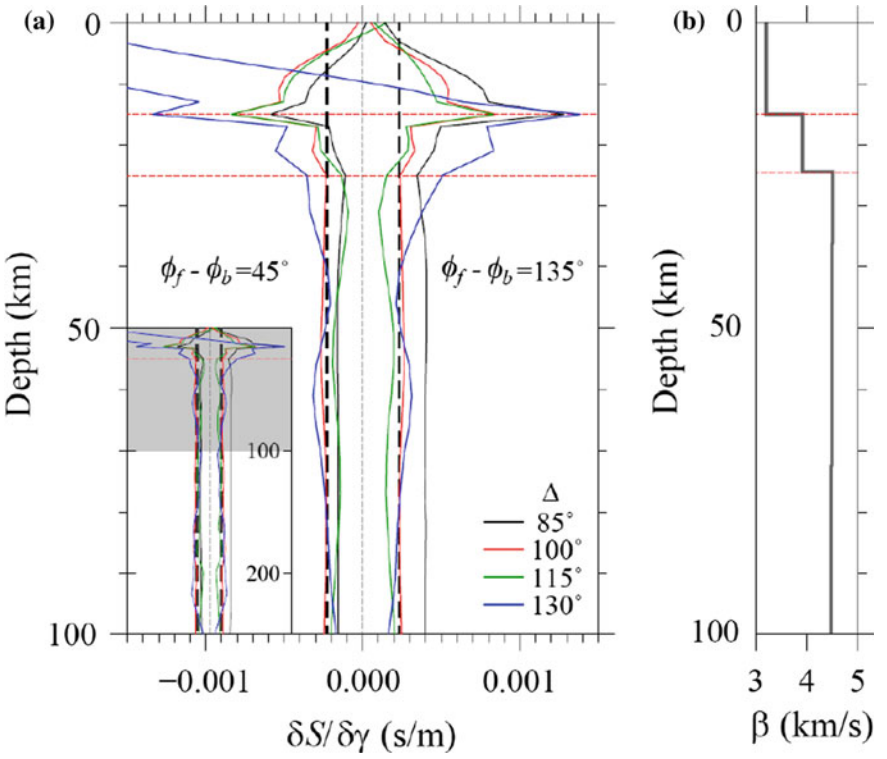

Fig. 4.4 **a** Depth variations of horizontally integrated 3D splitting intensity kernels. Kernels for different epicentral distances are depicted by lines of different colors (*black*: 85°; *red*: 100°; *green*: 115°; *blue*: 130°). All kernels are calculated using two values of the differential angle $\phi_f - \phi_b$. The kernels having negative amplitudes in the mantle correspond to $\phi_f - \phi_b = 45°$, whereas those having positive amplitudes in the mantle correspond to $\phi_f - \phi_b = 135°$. The two black vertical dashed lines show the uniform sensitivity under the assumption of a single vertically incident plane SKS wave, i.e. the SI predicted by $\delta t \sin 2(\phi_f - \phi_b)$. **b** Shear-wave speed in the topmost 100 km in model PREM. The two red horizontal dashed lines in (**a**) and (**b**) depict the mid-crust and Moho discontinuities in PREM. Reprinted from Lin et al. (2014a) with permission Geophysical Research Letters

than the ray-theoretical one in the crust. This results in the ~ 0.3 s discrepancy in the estimation of δt as seen in Fig. 4.3a. Thus, even when SKS wave is well-isolated or dominant relative to its neighboring phases, near-field effect can still have significant contribution to the shear-wave splitting intensity. The asymmetry in the 1D kernels with respect to the vertical axis of $S = 0$ is also consistent with the vertical shifts of the sinusoidal curves in Fig. 4.3a.

4.4 Conclusion

Using the full-wave sensitivity kernels of SKS splitting intensity to elastic anisotropic parameters calculated by normal-mode theory, we have demonstrated that the interference of SKS with other phases of similar arrival times, the near-field effect, and the multiple reflections in the crust can lead to strong dependence of the splitting intensity on the epicentral distance. The full-wave effects are neglected in the common practices of shear-wave splitting analysis which explicitly assumes that the observed SKS or SKKS phase is composed of a single vertically incident plane wave. The adoption of such an assumption simplifies the interpretation of shear-wave splitting in terms of the strength of anisotropy and the direction of the fast axis of symmetry. However, this assumption not only imposes a strong restriction on the source-receiver geometry in the application of SKS splitting analysis, but also allows only for the characterization of an average (uniform) anisotropic structure in the crust and mantle. The full-wave sensitivity kernels account for the effects of all possible wave interferences involved in shear-wave splitting and therefore loosen the restrictions on source-receiver geometry amenable to shear-wave splitting analysis. Furthermore, the 3D Fréchet kernels also afford us the capability to resolve the vertical and lateral variations in seismic anisotropy and obtain 3D images of the Earth's anisotropic structure.

References

Ando M (1984) ScS polarization anisotropy around the Pacific Ocean. J Phys Earth 32:179–195

Babuška V, Cara M (1991) Seismic Anisotropy in the Earth. Kluwer Academic Publishers, The Netherlands

Becker TW, Chevrot S, Schulte-Pelkum V, Blackman DK (2006) Statistical properties of seismic anisotropy predicted by upper mantle geodynamic models. J Geophys Res 111:B08309. doi:10.1029/2005JB004095

Browaeys J, Chevrot S (2004) Decomposition of the elastic tensor and geophysical applications. Geophys J Int 159:667–678

Chapman CH, Chu J-Y, Lyness DG (1988) The WKBJ seismogram algorithm. In: Doornbos DJ (ed) Seismological Algorithms. Academic Press, London, pp 47–74

Chevrot S (2000) Multichannel analysis of shear wave splitting. J Geophys Res 105:21 579–21 590.

Chevrot S (2006) Finite frequency vectorial tomography: a new method for high resolution imaging of upper mantle anisotropy. Geophys J Int 165:641–657
Crotwell HP, Owens TJ, Ritsema J (1999) The TauP Toolkit: Flexible seismic travel-time and ray-path utilities. Seismol Res Lett 70:154–160
Dahlen FA, Hung S-H, Nolet G (2000) Fréchet kernels for finite-frequency traveltimes—I. Theory. Geophys J Int 141:157–174
Dziewonski AM, Anderson DL (1981) Preliminary reference Earth model. Phys Earth Planet Int 25:297–356
Favier N, Chevrot S (2003) Sensitivity kernels for shear wave splitting in transverse isotropic media. Geophys J Int 153:213–228
Favier N, Chevrot S, Komatitsch D (2004) Near-field influences on shear wave splitting and traveltime sensitivity kernels. Geophys J Int 156:467–482
Lin Y-P, Zhao L, Hung S-H (2014a) Full-wave effects on shear wave splitting. Geophys Res Lett 41(3):799–804. doi: 10.1002/2013GL058742
Liu Q, Tromp J (2006) Finite-frequency kernels based upon adjoint methods. Bull seism Soc Am 96:2383–2397
Long MD (2009) Complex anisotropy in D" beneath the eastern Pacific from SKS–SKKS splitting discrepancies. Earth Planet Sci Lett 283:181–189
Mensch T, Rasolofosaon P (1997) Elastic-wave velocities in anisotropic media of arbitrary symmetry-generalization of Thomsen's parameters ε, δ and γ. Geophys J Int 128:43–64. doi:10.1111/j.1365-246X.1997.tb04070.x
Monteiller V, Chevrot S (2011) High-resolution imaging of the deep anisotropic structure of the San Andreas Fault system beneath southern California. Geophys J Int 186:418–446
Savage MK (1999) Seismic anisotropy and mantle deformation: what have we learned from shear wave splitting? Rev Geophys 37:65–106
Sieminski A, Paulssen H, Trampert J, Tromp J (2008) Finite-frequency SKS splitting: measurement and sensitivity kernels. Bull seism Soc Am 98:1797–1810
Silver PG (1996) Seismic anisotropy beneath the continents: probing the depths of geology. Ann Rev Earth Planet Sci 24:385–432
Silver PG, Chan WW (1988) Implications for continental structure and evolution from seismic anisotropy. Nature 335:34–39
Tromp J, Tape C, Liu Q (2005) Seismic tomography, adjoint methods, time reversal and banana-doughnut kernels. Geophys J Int 160:195–216
Vinnik L, Kosarev GL, Makeyeva LI (1984) Anisotropy of the lithosphere from the observation of SKS and SKKS. Proc Acad Sci USSR 278:1335–1339
Wessel P, Smith WHF (1995) New version of generic mapping tools released. EOS Transactions, AGU 76:329
Wüstefeld A, Bokelmann G, Zaroli C, Barruol G (2008) SplitLab: a shear-wave splitting environment in Matlab. Comput Geosci 34:515–528
Zhao L, Chevrot S (2011a) An efficient and flexible approach to the calculation of three-dimensional full-wave Fréchet kernels for seismic tomography: I-Theory. Geophys J Int 185:922–938
Zhao L, Chevrot S (2011b) An efficient and flexible approach to the calculation of three-dimensional full-wave Fréchet kernels for seismic tomography: II–Numerical results. Geophys J Int 185:939–954
Zhao L, Jordan TH (1998) Sensitivity of frequency-dependent traveltimes to laterally heterogeneous, anisotropic earth structure. Geophys J Int 133:683–704
Zhao L, Jordan TH, Chapman CH (2000) Three-dimensional Fréchet differential kernels for seismic delay times. Geophys J Int 141:558–576

Chapter 5
Full-Wave Multiscale Anisotropy Tomography in Southern California

The Southern California Earthquake Data Center (SCEDC) operates a densely distributed seismic network in Southern California. The high-quality seismic data it provides have enabled seismologists to obtain high-resolution 3D isotropic velocity models for this region. Owing to the limitations of ray-theory assumption used in anisotropy analysis, the 3D anisotropic structure in Southern California is still poorly understood. In this chapter, we apply our full-wave tomography method to the seismically densely covered Southern California to obtain a 3D anisotropic model of this region. Reliable 3D anisotropic model can help us understand the processes of the upper mantle flow and the crustal deformation.

5.1 Introduction

The San Andreas Fault (SAF), the boundary between the Pacific and North American plates, involves a complex system of faults accommodating ~23–37 mm/yr of slip and ~75% of the relative motion between the two plates (Molnar and Dayem 2010). The pattern of lithospheric deformation and the dynamics of the lithosphere–asthenosphere interaction have persistently been a hot topic of investigation. Seismic anisotropy provides key structural information for studying the mechanics of the SAF system, including the deformations and relative motions of the tectonic blocks, which is critically important for a better understanding of the seismic risks for the entire California coastal region.

There have been numerous studies devoted to isotropic seismic structures of Southern California using body-wave travel times (Kohler et al. 2003; Plesch et al. 2007), surface wave phase and/or group velocities (Press 1956; Polet and Kanamori

Originally published in [Geophysical Research Letters Dec 2014 vol. 41 8809–8817]. Published with kind permission of © 2014. American Geophysical Union. All Rights Reserved.

Y.-P. Lin, *Isotropic and Anisotropic Seismic Tomography Using Active Source and Earthquake Records*, Springer Theses, DOI 10.1007/978-981-10-5068-8_5

1997; Tanimoto and Prindle Sheldrake 2002; Yang and Forsyth 2006), ambient noise (Shapiro et al. 2005; Yang et al. 2008), and full waveforms (Chen et al. 2007; Tape et al. 2009; Lee et al. 2014). In contrast, less attention has been paid to the seismic anisotropic structures in Southern California. A rare exception was the finite-frequency anisotropy tomography of Monteiller and Chevrot (2011), although some of recent surface-wave azimuthal anisotropy models in the western United States (Yuan and Romanowicz 2010; Yuan et al. 2011; Lin et al. 2011) provided a glimpse of gross anisotropy in the region with limited lateral and vertical resolutions down to $\sim$70 km only.

Characterizing the anisotropic structure can help us understand the deformation and dynamic processes in the Earth's interior, and shear-wave splitting has been one of the primary observables in the investigation of elastic anisotropy in the crust and upper mantle. However, until recently the interpretation of shear-wave splitting in terms of anisotropy has been largely dependent on the ray-theory modelling of a single vertically incident plane shear wave, under which the shear-wave splitting measurements at a given station are related to the symmetry axis and strength of seismic anisotropy by a sinusoidal relation:

$$S_i = \delta t \, \sin 2(\phi_f - \phi_b^i), \tag{5.1}$$

where S_i is the shear-wave splitting intensity (SI) at the i-th station whose back-azimuth is ϕ_b^i, and ϕ_f and δt are respectively the azimuth of the fast axis (the polarization of the fast quasi-shear wave) and the splitting time between fast and slow quasi-shear waves. The pair of the apparent anisotropy parameters, δt and ϕ_f, then prescribes a uniform layer of anisotropy beneath the station, and the amount of splitting of an individual shear wave varies with the differential angle $\phi_f - \phi_b^i$ only. The harsh assumption of a single incident plane wave in ray theory limits the range of source-station geometry useful for shear-wave splitting measurements and reduces our ability to resolve the spatial variations in anisotropy. In this study, we apply a new approach to the inversion of three-dimensional (3D) anisotropy structure based on the full-wave sensitivity (Fréchet) kernels of the splitting data (Zhao and Chevrot 2011a, b; Lin et al. 2014a). With the help of strain Green tensor (SGT) databases calculated by normal-mode summation in one-dimensional (1D) reference models, the 3D sensitivity kernels of shear wave splitting data to anisotropy model parameters can be calculated efficiently. These full-wave kernels accurately account for all the wave interactions that are neglected in ray theory, including near-field effect and interferences of multiple arrivals (Lin et al. 2014a). Favier et al. (2004) also used the horizontally integrated depth-dependent 1D kernels in a homogeneous reference model to illustrate the near- and middle-field terms missing in ray theory. Our full-wave approach uses realistic reference models and accounts for the multiple reflections at the internal discontinuities. The resulting depth-dependent sensitivities, as shown in Lin et al. (2014a), have drastic fluctuations near the surface, especially around the midcrust and Moho discontinuities as

a consequence of the combined effects of near-field complexity and multiple reflections in the two crustal layers.

In this study, we use the broadband records at stations in Southern California from globally distributed earthquakes and measure the splitting intensity from horizontal records of SKS waves. We then calculate the full-wave sensitivity kernels for the obtained splitting data and carry out a multiscale inversion of the anisotropic structure using a wavelet-based model parameterization (Chiao and Kuo 2001; Chiao and Liang 2003; Chiao et al. 2010, 2014). In addition, we appraise our anisotropy tomography inversion through a rigorous resolution analysis based on the statistical resolution matrix method of An (2012), which provides an effective means to estimate the resolution lengths of the inversion without explicitly calculating the resolution matrix. We also provide an interpretation of our anisotropic model for the Southern California region in terms of geodynamic and geological implications.

5.2 Splitting Intensity Measurements and Full-Wave Sensitivity Kernels

We measure the splitting intensities of the SKS waves from events during the time period of 2000–2013 with epicentral distances between 90° and 130°. Considering a wide range of azimuthal distribution and with redundancy removed, a total of 175 events with magnitudes larger than 6.0 are used in this study (red dots in Fig. 5.1a). The high-quality records from 223 stations concentrated in the Southern California region (blue triangles in the inset panel of Fig. 5.1a) are all downloaded from the Southern California Earthquake Data Center.

Chevrot (2000) demonstrated that the optimal measurement of the shear-wave splitting in Eq. (5.1) is the so-called splitting intensity, and that it can be derived from the integral of the product of the SKS signal on the transverse-component $u_T(t)$ and the time derivative of the SKS on the radial-component $\dot{u}_R(t)$, i.e. (e.g. Favier and Chevrot 2003, 2006)

$$S = -2\frac{\int_{t_1}^{t_2} \dot{u}_R(t)u_T(t)dt}{\int_{t_1}^{t_2} [\dot{u}_R(t)]^2 dt}, \tag{5.2}$$

where the integrals are taken over the time window $[t_1, t_2]$ selected for each shear-wave phase of interest. Considering the dominant periods of the SKS signals and to minimize the interference with neighboring phases, we bandpass all the waveforms between 0.02 and 0.12 Hz ($\sim$50–8 s). In order to ensure the data quality, we manually select the SKS window in each record with a high signal to noise ratio (black lines in Fig. 5.1b) and a high similarity between recorded and synthetic waveforms (red lines in Fig. 5.1b) calculated by normal-mode summation for Earth model PREM (Dziewonski and Anderson 1981). Following Eq. (5.2), we compute the splitting intensity S from the SKS signals on both radial and transverse components. An example of the measurement is shown in Fig. 5.1b for the record

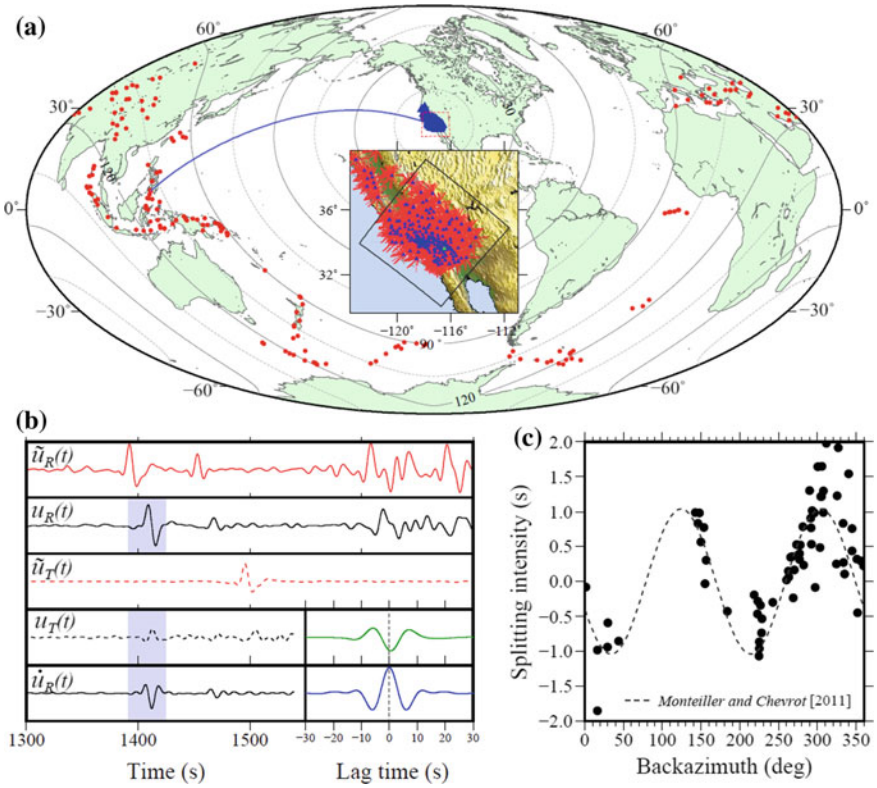

Fig. 5.1 **a** Distribution of stations (*blue triangles*) and events (*red dots*) used in this study. The *red bars* in the inset panel shows the surface projections of the SKS ray paths in the topmost 350 km of the earth beneath the receivers (*blue triangles*). **b** An example of shear-wave splitting measurement. *Black and red lines* are the recorded and synthetic seismograms on radial (solid) and transverse (dashed) components, respectively. Synthetics are calculated by normal-mode summation in the reference model PREM. *Shaded zones* are the time windows $[t_1, t_2]$ selected for splitting intensity measurements. The panel in the *bottom-right corner* shows the cross correlation between $u_T(t)$ and $\dot{u}_R(t)$ (*green line*) and the auto correlation of $\dot{u}_R(t)$ (*blue line*), while the amplitudes at zero lag time marked by *dashed vertical lines* give respectively the values of the numerator and denominator in Eq. (5.2). **c** Individual splitting intensity measurements (*black dots*) varying with backazimuth at station PFO obtained in this study. The *dashed curve* is the *sinusoidal curve* that best fits the bin-averaged splitting measurements at PFO from the previous study of Monteiller and Chevrot (2011). Reprinted from Lin et al. (2014b) with permission Geophysical Research Letters

from a deep event to station PFO with an epicentral distance of 110.7° (blue great-circle path in Fig. 5.1a). Following a set of strict criteria for data selection, we obtain 5954 splitting intensity measurements. The surface projections of the 5954 SKS ray paths in the topmost 350 km of the earth beneath the receivers (red bars in the inset panel of Fig. 5.1a) manifest an excellent azimuthal coverage, which is essential for obtaining high-resolution images of the 3D anisotropy structure in the study region.

In the conventional SKS splitting analysis assuming a single incident plane wave, the splitting measurements at a given station would vary with back Azimuthin a sinusoidal fashion as shown in Eq. (5.1). Monteiller and Chevrot (2011) implicitly adopted this assumption by first averaging individual splitting intensity measurements in given azimuthal bins to improve the fit of the theoretical sinusoidal curve and using the bin-averaged values for the subsequent inversion of the anisotropic structure (dashed curve in Fig. 5.1c). However, from the full-wave point of view, the SKS phase often interferes with neighboring phases which can lead to a significant contribution to the splitting measurements (Lin et al. 2014a). As a result, the azimuthal variation of the splitting intensity measurements at a given station is no longer simply a sinusoidal function, but rather complex depending on the epicentral distance and even on the earthquake source mechanism (Lin et al. 2014a). In the meantime, the full-wave approach, which accounts for all the interferences between SKS and neighboring phases as well as the near-field effect in the close proximity of the station, allows for the calculation of the sensitivity kernels of individual splitting measurement to the anisotropic structural model parameters. Therefore, the individual splitting measurements can be used directly to invert for the anisotropic structure without the need to fit them first by a sinusoidal curve.

As demonstrated in Zhao and Chevrot (2011b) and Lin et al. (2014a), shear-wave splitting is mostly sensitive to the anisotropic model parameter $\gamma = (C_{66} - C_{44})/2\rho\beta^2$, where ρ is density, β is the background isotropic S-wave velocity, and C_{ij} are the elements of the elasticity tensor in the Voigt notation (Babuška and Cara 1991; Browaeys and Chevrot 2004). Lin et al. (2014a) also showed that the contributions to shear-wave splitting intensity from the other two anisotropy parameters $\varepsilon = (C_{11} - C_{33})/2\rho\alpha^2$ and $\delta = (C_{13} - C_{33} + 2C_{44})/\rho\alpha^2$, where α is the background isotropic P-wave speed, are less than 10% of that from γ. The model parameters for shear-wave anisotropy thus involves γ, a dimensionless parameter prescribing the strength of shear-wave anisotropy (Mensch and Rasolofosaon 1997; Becker et al. 2006; Chevrot 2006), and the azimuth of the fast axis ϕ_f. The dependence of the splitting intensity S on ϕ_f is, however, clearly non-linear. To achieve a linearized inversion, Favier and Chevrot (2003) defined an alternative set of two independent parameters, $\gamma_c = \gamma \cos 2\phi_f$ and $\gamma_s = \gamma \sin 2\phi_f$, which can be linearly related to the splitting intensity S:

$$S = \iiint \left[K^S_{\gamma_c}(r,\theta,\varphi)\gamma_c(r,\theta,\varphi) + K^S_{\gamma_s}(r,\theta,\varphi)\gamma_s(r,\theta,\varphi) \right] dr d\theta d\varphi, \tag{5.3}$$

where $K^S_{\gamma_c}$ and $K^S_{\gamma_s}$ are the sensitivity kernels of splitting intensity S to γ_c and γ_s, respectively. The obtained γ_c and γ_s from the inversion are combined to calculate the fast direction and strength of anisotropy through the relations of $\phi_f = 0.5 \tan^{-1}(\gamma_c/\gamma_s)$ and $\gamma = -\sqrt{\gamma_c^2 + \gamma_s^2}$. Examples of the 3D sensitivity kernels of S to γ_c and γ_s are shown in Fig. 5.2a and b, respectively, with the same source-receiver configuration as in Fig. 5.1b for the reference model PREM. For the incoming SKS

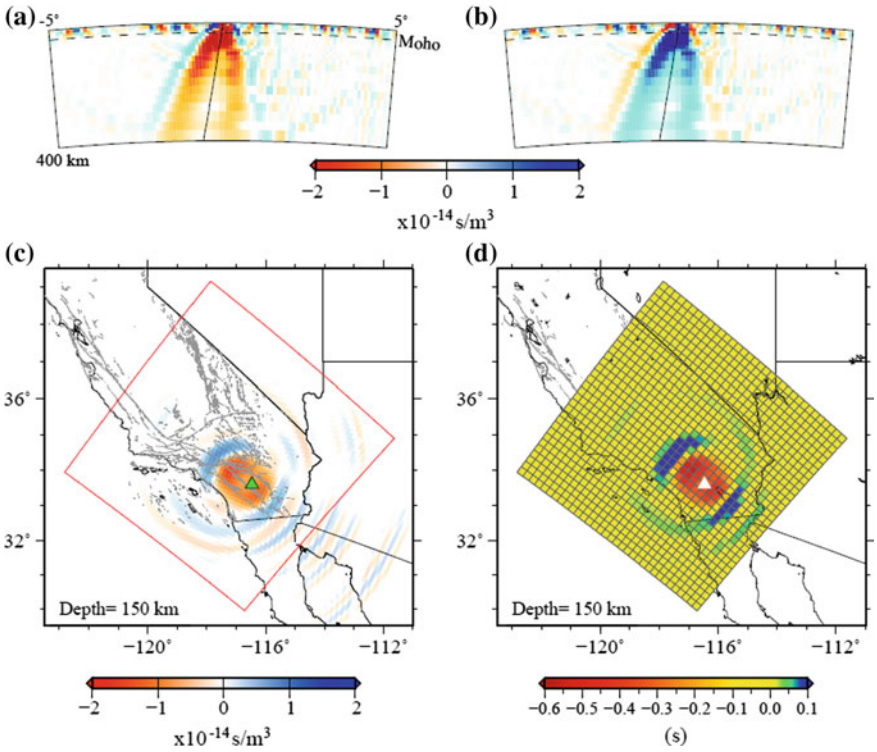

Fig. 5.2 Example of 3D Full-wave Fréchet kernels of the splitting intensity for shear-wave anisotropy parameters γ_c (**a**) and γ_s (**b**), shown on the source-receiver great-circle plane near the station. **c** Map view of the same γ_c kernel in **a** at the depth of 150 km. The *red box* depicts the *horizontal extent* of the anisotropic model to be inverted for. **d** The same kernel in **c** after taking the volumetric integration over individual voxels bounded by the regularly-spaced mesh (*black lines*) which subdivide the continuous anisotropic model by 33 discrete nodes in each spatial dimension. Each voxel-integral value comprises a fraction of a particular element of the **G** matrix in Eq. (5.4), and the *horizontal slice* shown in **d** represents a segment of a particular row of **G** corresponding to a splitting intensity measurement obtained at the station shown by the *triangle*. Reprinted from Lin et al. (2014b) with permission Geophysical Research Letters

wave from a backazimuth of 293°, both kernels display relatively simple banana-doughnut shapes with red and blue "skins" delineating the regions of strong sensitivity.

5.3 Multiscale Inversion

In order to make the tomography inversion adaptable to the spatially varying resolution due to uneven path coverage, we adopt a multiscale, wavelet-based approach for model parameterization (Chiao and Kuo 2001; Chiao and Liang 2003;

Chiao et al. 2010, 2014). With such scale-adaptive parameterization, our tomography inverse problem can be expressed in a matrix form:

$$(\mathbf{G}\mathbf{W}^{-1})(\mathbf{W}\mathbf{m}) = \mathbf{d}, \tag{5.4}$$

where **m** is the vector comprising the model parameters at nodes in space discretized by a regularly-spaced mesh, **d** is the data vector of individual splitting measurements, and **G** is the data kernel or Gram matrix. Each element of the Gram matrix **G** is associated with a node and contains the weighted sum of the volumetric integrals of the sensitivity kernel over all the voxels surrounding the node (Fig. 5.2d). Matrix **W** represents a 3D primary wavelet transformation operator. In practice, we first parameterize the model by a 3D uniform mesh, and apply a transpose of the inverse wavelet operator $(\mathbf{W}^{-1})^{\mathrm{T}}$ on each row of the data kernel **G**. The final model can be obtained by an inverse wavelet transform from the wavelet domain to the spatial domain. Details of the implementation of the multiscale parameterization are well documented in Hung et al. (2011). The wavelet approach preserves both the finer spatial resolution in regions of better data coverage and the coarser resolution in less well-sampled regions, thus resolving the structure with an objective and data-driven multiscale resolution.

Our model has a horizontal dimension of 640 km × 640 km (rotated black box in the inset panel of Fig. 5.1a) and a vertical dimension from the surface down to 350-km depth. We parameterize our study region by a uniform mesh, with 33 nodes in each dimension spaced by 20 km horizontally and 10.9 km vertically. We run inversion experiments using both the wavelet-based model parameterization and the simple uniform mesh without applying the wavelet transformation, solving the linear system of Eq. (5.4) for either **Wm** or **m** by the iterative least-squares QR-factorization (LSQR) algorithm (Paige and Saunders 1982a, b). A standard choice is the damped least-squares solution in which an optimal damping is selected by exploring the tradeoff between the model norm and the data variance reduction. We choose the optimal damping factors of 10 and 100 corresponding respectively to the maximum curvatures of the tradeoff curves in the inversions using simple uniform-mesh and wavelet-based model parameterizations (Fig. 5.3). These damping factors in the inversions are dimensionless. They act differently in the inversions using uniform-mesh and wavelet-based model parameterizations. In the conventional uniform-mesh parameterization, the damping factor is a threshold for removing the small singular values of the Gram matrix during the inversion. So the damping acts on the entire model uniformly. For the wavelet parameterization, on the other hand, the damping is imposed on the wavelet coefficients. Larger-scale features are better constrained by the data and their corresponding wavelet coefficients also have larger singular values than those for smaller-scale features. Furthermore, in regions with better path coverage, more singular values for small-scale wavelet coefficients are above the threshold and retained, while in sparsely sampled regions more singular values for small-scale wavelet coefficients will be damped out. Therefore, the damping affects different regions of the model differently according to the data coverage.

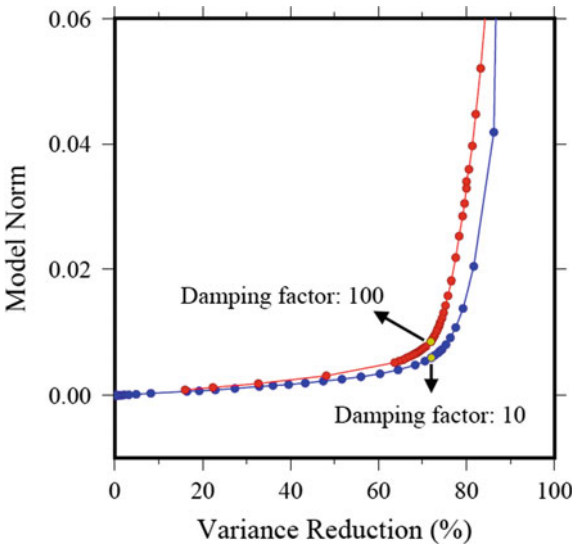

Fig. 5.3 Tradeoff curves between model norm and data variance reduction for the inversions with simple uniform-mesh (*blue curve*) and wavelet-based (*red curve*) model parameterizations. The model norm is the root-mean-square magnitude of the model parameters, defined as $\sqrt{\frac{1}{M}\sum_{i=1}^{M} m_i^2}$, where M is the number of model nodes. The data variance reduction quantifies the level of data fit, defined as $\left[1 - \sum_{i=1}^{N} (\hat{d}_i - d_i)^2 \Big/ \sum_{i=1}^{N} d_i^2\right] \times 100\%$, where N is the number of data, $\hat{d}_i$ and d_i are the model prediction and data, respectively. We select the optimal damping factors of 100 and 10 for the models obtained with wavelet-based and simple uniform-mesh parameterizations, respectively, which correspond to the points (*yellow dots*) of maximum curvatures on the *tradeoff curves*. Reprinted from Lin et al. (2014b) with permission Geophysical Research Letters

Although the LSQR method provides an efficient means to solve large-scale inverse problems, it proves difficult for obtaining the resolution matrix directly to assess the spatial resolution of the model. Instead of conducting common recovery tests of synthetic models with a few prescribed checkerboards or other forms of structures, here we adopt the statistical resolution matrix method of An (2012) to estimate the variation of the resolution lengths of individual model parameters in 3D. Since the resolution matrix does not rely on the data or the model parameters, but on the properties of the data kernel $\mathbf{G}$, it can be probed by a limited set of random synthetic models and their recoveries from inversions. As each inverted model parameter can be treated as the weighted average of the neighboring true model parameters, the resolution matrix comprising these weights is presumed to be a 3D Gaussian function whose unknown width at half of its peak value in each dimension is defined as the resolution length. A finite set of random synthetic models are generated to explore their recoveries obtained by two different means:

one from the damped least-squares inversion of individual model-synthesized data using the same model parameterization and regularization applied to real splitting data, and the other from the projection of individual random models via the Gaussian resolution matrix. The resolution length is then estimated by a grid search for the optimal width which minimizes the sum of the absolute difference between the two kinds of recoveries for individual random models. The statistical resolution matrix approach does not require any matrix operation, and is therefore very suitable for estimating resolution lengths of large linear inverse problems.

The efficiency and accuracy of the obtained statistical resolution length hinge upon the number of input random models and their inverse solutions. We determine

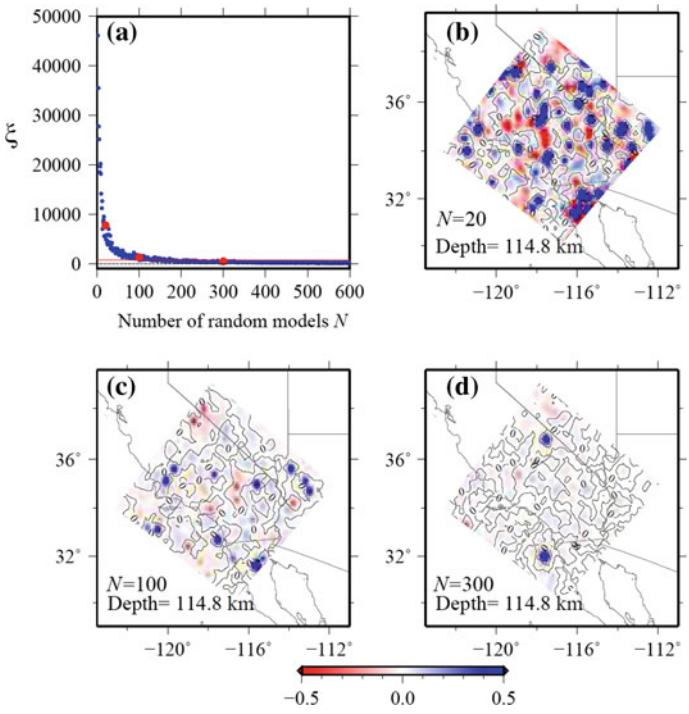

Fig. 5.4 **a** Sum of the absolute normalized differences in the resolution lengths of all the model parameters, $\xi = \sum_{i=1}^{M} \left| \frac{w_i^N - w_i^{N-1}}{w_i^{N-1}} \right|$, between two consecutive grid searches for the optimal half width of the Gaussian resolution function using N and N-1 random input models. Here w_i is the resolution length at ith model node. The *red dots* show the values of ξ with N = 20, 100 and 300. The *red line* marks the average of the absolute normalized differential resolution length per node (ξ/M) reducing to 2%. The final resolution lengths are obtained with N = 300 while the value of ξ/M reaches $\sim$1%. As seen in the plot, ξ decreases rapidly as N increases for the cases of N < 50 and reaches a stable level afterwards. **b–d** Map views of the normalized differential resolution length, $\frac{w_i^N - w_i^{N-1}}{w_i^{N-1}}$, of individual model parameters at the depth of 114.8 km, obtained with N = 20, 100, and 300. Reprinted from Lin et al. (2014b) with permission Geophysical Research Letters

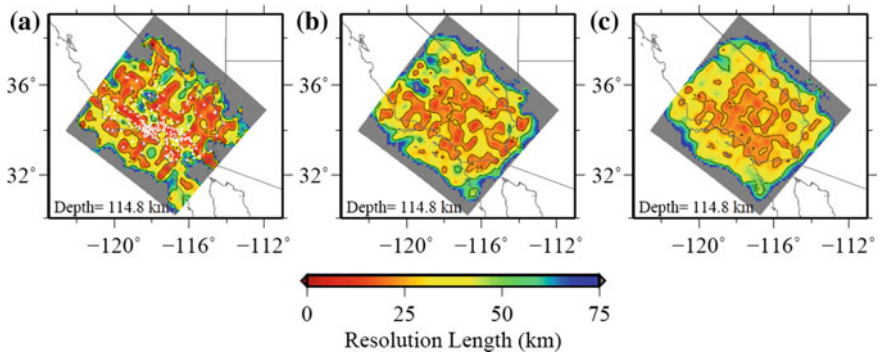

Fig. 5.5 Lateral variations of resolution lengths at 114.8-km depth obtained from **a** $N = 20$, **b** $N = 100$, and **c** $N = 300$ random synthetic models. The stations providing the splitting data are denoted by *white triangles* in **a**. The pattern of the spatially-varying resolution lengths becomes smooth and stabilized with the increase of N. Reprinted from Lin et al. (2014b) with permission Geophysical Research Letters

the optimal number of random synthetic models by examining the average difference in the resolution lengths of all model nodes ($33 \times 33 \times 33$ nodes) derived from two consecutive grid searches for resolution lengths with N and N-1 random input models. The average differential resolution length reaches $\sim 1\%$ with 300 and 299 random models (Figs. 5.4 and 5.5). We therefore choose $N = 300$ in all statistical resolution matrix calculations.

Displayed in Fig. 5.6 are the lateral resolution lengths for γ_c at depths of 60.2, 114.8, 169.5, and 235.2 km achieved by the inversion of the ~ 6000 splitting data obtained in this study. The resolution-length maps shown in Fig. 5.6a–d are solved with 300 pairs of random models and their recoveries using the simple uniform-mesh parameterization with the optimal damping factor 10. The resloution-length maps by wavelet-based inversion with damping factor 100 are shown in Fig. 5.6e–h. Notwithstanding the lengths of 25–50 km in the interior of the study region covered by densely-distributed stations, the multiscale wavelet-based inversion in general yields better and more uniform resolution. These consequences confirm that the wavelet approach preserves a higher spatial resolution in regions of better data coverage and the long-wavelength features in relatively less-constrained regions. Therefore, our following discussion on the anisotropic structure of Southern California will be based on the model obtained by the multiscale inversion. In addition, a bootstrap test is conducted to further validate our inversion result (Fig. 5.7). A comparison of the observed apparent splitting parameters, i.e. the fast axis ϕ_f and splitting time δt in Eq. (5.1), with predictions by our 3D anisotropic model displays highly consistent patterns (Fig. 5.8). Our following discussion on the anisotropic structure of Southern California will be based on the model obtained by the multiscale inversion.

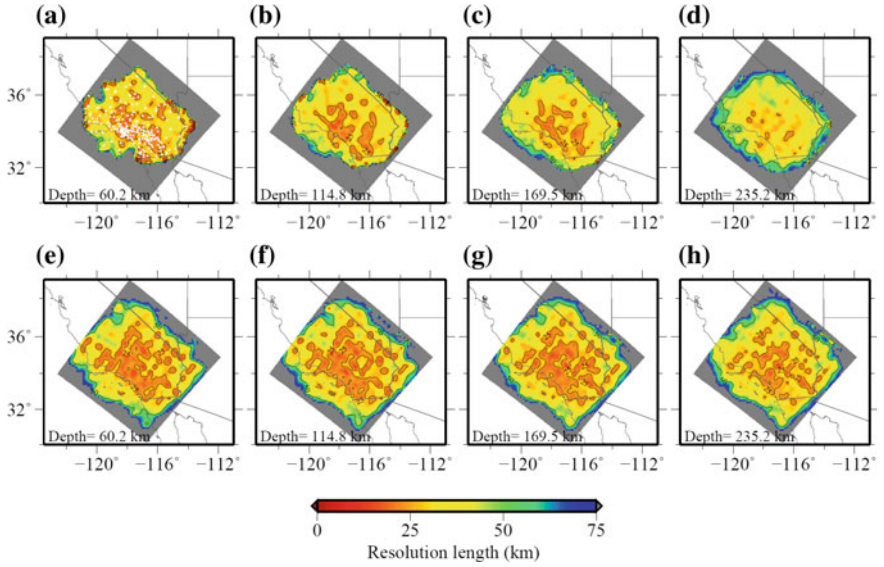

Fig. 5.6 Lateral resolution lengths for the anisotropy parameter γ_c at the depths of 60.2 km (**a** and **e**), 114.8 km (**b** and **f**), 169.5 km (**c** and **g**), and 235.2 km (**d** and **h**), estimated by the statistical resolution matrix method for the 3D anisotropy model parameterized at ~20 km spaced nodes and inverted from ~6000 splitting data. The γ_c model obtained with wavelet-based multiscale parameterization has shorter resolution lengths and larger resolvable extent (**e**–**h**), compared to those with simple uniform-mesh parameterization (**a**–**d**). The resolution lengths are all derived with 300 random input models of γ_c and their recoveries. The stations contributing to the splitting measurements are denoted by *white triangles* in **a**. The resolution lengths for γ_s are very similar to those for γ_c shown here. Reprinted from Lin et al. (2014b) with permission Geophysical Research Letters

5.4 Result and Discussion

Considering the average lithospheric thickness of 70–90 km in Southern California (Yang and Forsyth 2006; Ford et al. 2014) and our vertical resolution length of ~50 km (Fig. 5.9), we display our 3D anisotropic model at four depths in Fig. 5.10: one in the lithosphere (60.2 km) and three in the asthenosphere (114.8, 169.5, and 235.2 km). The resulting strength of anisotropy (indicated by the background color) varies between −0.01 and −0.03 (1–3% anisotropy) in this region, and slightly decreases with depth. The direction of fast axis varies more dramatically in the lithosphere than in the asthenosphere.

For the long-wavelength features, the fast axis exhibits a counter-clockwise rotation from WNW-ESE in the southwest quadrant located on the Pacific Plate (PP) to NE-SW in the northeast quadrant inside the North American Plate (NAP). Some regions in the lithosphere display a more complex pattern of the fast axis that can be linked to surface geologic signatures (Fig. 5.10a). To the west of the Salton

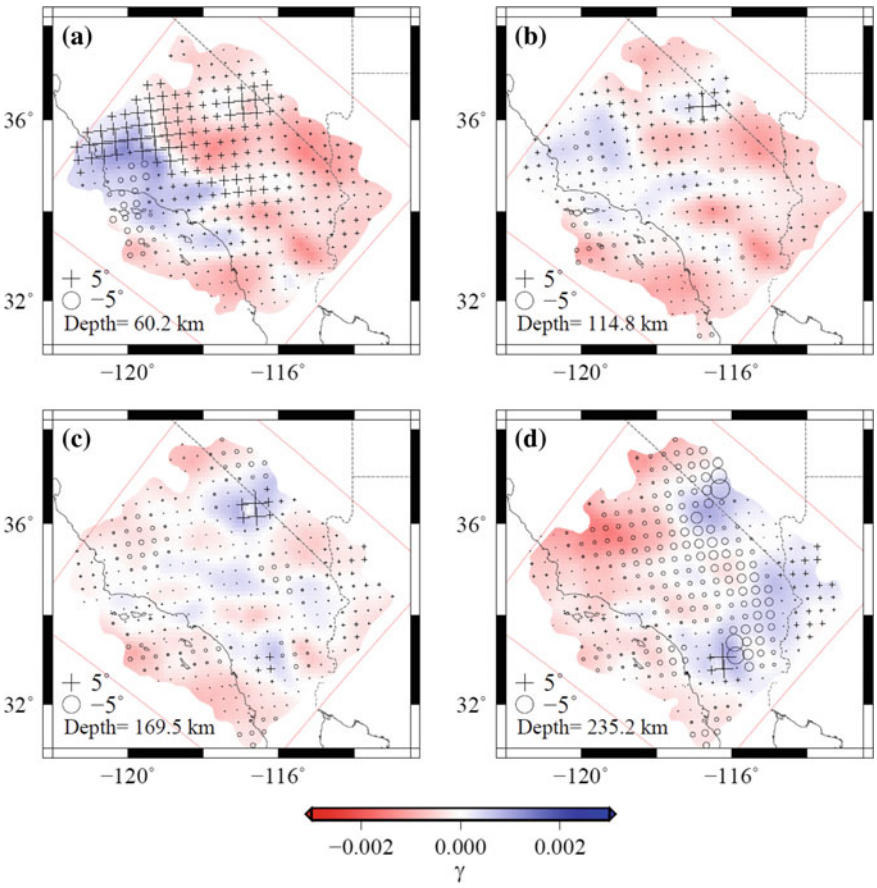

Fig. 5.7 Bootstrap test of the inversion result. Map views of the differences between the optimal damped least *squares solution* of the anisotropic model beneath Southern California (Fig. 5.10) and the bootstrap model inverted from a subset of the splitting data at the depths of **a** 60.2 km, **b** 114.8 km, **c** 169.5 km, and **d** 235.2 km. *Background colors* show the differences of γ between the two models, while crosses and *open circles* represent the differences in the azimuths of fast axes. The bootstrap model is derived by averaging the models obtained from 2000 inversions, each of which only uses a subset of 5000 splitting data randomly selected from the entire set of 5954 data. Overall, the difference in the azimuths of fast axes and γ between our final model and the bootstrap model are less than 7° and 0.003, respectively. The bootstrap test shows that the inversion result is stable and robust. Reprinted from Lin et al. (2014b) with permission Geophysical Research Letters

Trough, the fast axis follows a NE-SW orientation. Across the Salton Trough where the anisotropy is weaker, the fast axis turns slightly to NW-SE direction east of the Salton Trough. This variation seems to persist down to the asthenosphere, coincident with the low-velocity anomaly which has been imaged in previous isotropic tomography models and interpreted as upwelling beneath the Salton Trough

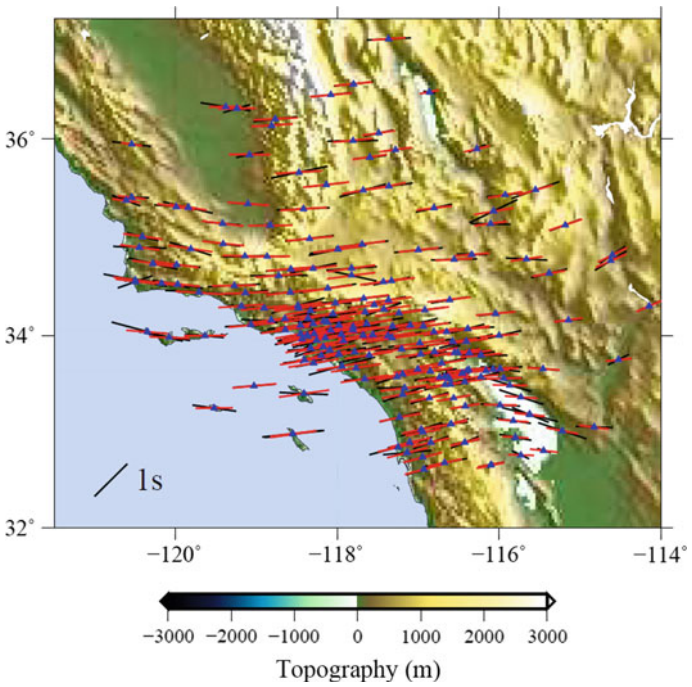

Fig. 5.8 Plot of the apparent splitting parameters (fast axis ϕ_f and splitting time δt in Eq. 5.1) at all stations (*blue triangles*) used in this study. The *black bars* depict the observed splitting parameters obtained by fitting measurements at each station to a sinusoidal curve; whereas the red bars represent predictions obtained by integrating the full-wave kernels through our 3D anisotropic model and then fitting the sinusoidal curves. The lengths of the *bars* are proportional to the splitting time δt. The predicted fast directions (*red bars*) show very similar patterns to the observations but with slightly reduced splitting times as a result of damping in the inversion. Reprinted from Lin et al. (2014b) with permission Geophysical Research Letters

(Humphreys and Clayton 1990; Yang and Forsyth 2006). A strong E-W fast polarization is observed beneath the Transverse Ranges undergoing active orogenic processes. In the westernmost part of the model, the fast axis is oriented more WNW-ESE, subparallel to the strike of the San Andreas Fault, and with a decreased strength in the lithosphere.

In the asthenosphere, the fast axis in regions more distant from the plate boundary (SAF) is well-correlated with the absolute plate motion (APM) calculated by the model NNR-MORVEL56 (Argus et al. 2011) as shown by the arrows in Fig. 5.9. In the easternmost part of our model under the NAP, the fast axes are mostly NE-SW, grossly consistent with the APM of the NAP ($\sim$223° clockwise from the north, red arrow in Fig. 5.9). In the westernmost part under the PP, the anisotropy becomes stronger with increasing depth and the fast axis turns to WNW-ESE, subparallel to the APM of the PP ($\sim$300° clockwise from the north,

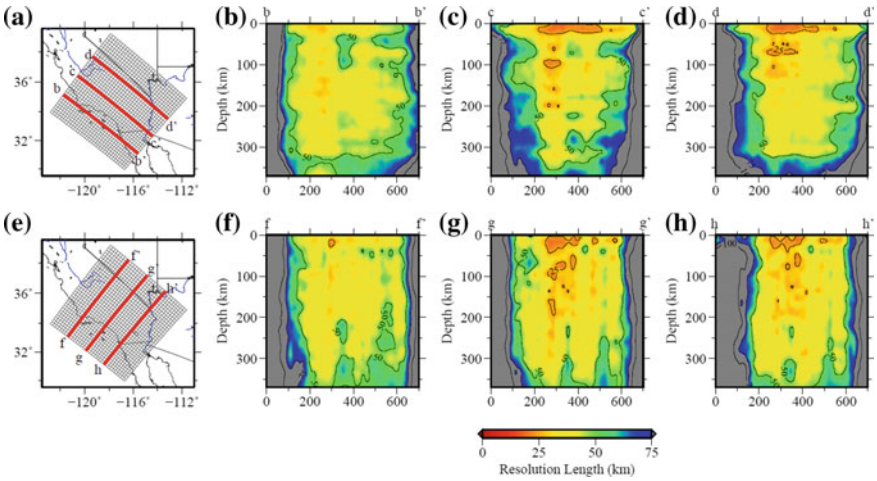

Fig. 5.9 Cross-sectional views of vertical resolution lengths estimated by the statistical resolution matrix method along the profiles marked in *red* in **a** and **e**. All the resolution lengths are calculated by 300 random synthetic models and their recoveries obtained with the multiscale inversion and the damping factor of 100. The vertical resolution length is about 50 km in the region covered by densely-distributed stations. Although the inversion of SKS splitting intensity data yields lower depth resolution than the lateral resolution discussed in the article, we still achieve decent depth resolution in comparison to the conventional SKS splitting analysis which assumes a layer of uniform anisotropy and provides almost no depth resolution. Reprinted from Lin et al. (2014b) with permission Geophysical Research Letters

green arrow in Fig. 5.10). The correlation between the fast axis and APM was also observed in surface-wave azimuthal anisotropy (Yuan et al. 2011; Kosarian et al. 2011). The persistent E-W fast axes in the asthenosphere across the plate boundary close to the central region of our model are neither parallel to the APM of the NAP nor the PP, but somewhat between these two orientations, implying the influence of the transitional variation in the APM of the two plates. A small circular region of weak anisotropy centered around (117° W, 36° N) is resolved throughout all the depths, indicative of the presence of a vertical flow there. A possible explanation is that the density-driven mantle flow becomes more vertical beneath the NAP (Fay et al. 2008). Overall, we do not observe particularly different patterns in the orientation of fast axis and anisotropy strength at different depths, whilst some of the features are persistent throughout the resolvable depths. Therefore, we do not observe a notable decoupling between the lithosphere and the underlying asthenosphere as reported by a few of the previous studies (Silver and Holt 2002; Monteiller and Chevrot 2011).

The 3D anisotropic model obtained with the full-wave approach in this study exhibits the variations in the fast-axis direction and strength of anisotropy which are in general similar to those in Monteiller and Chevrot (2011), except that in the

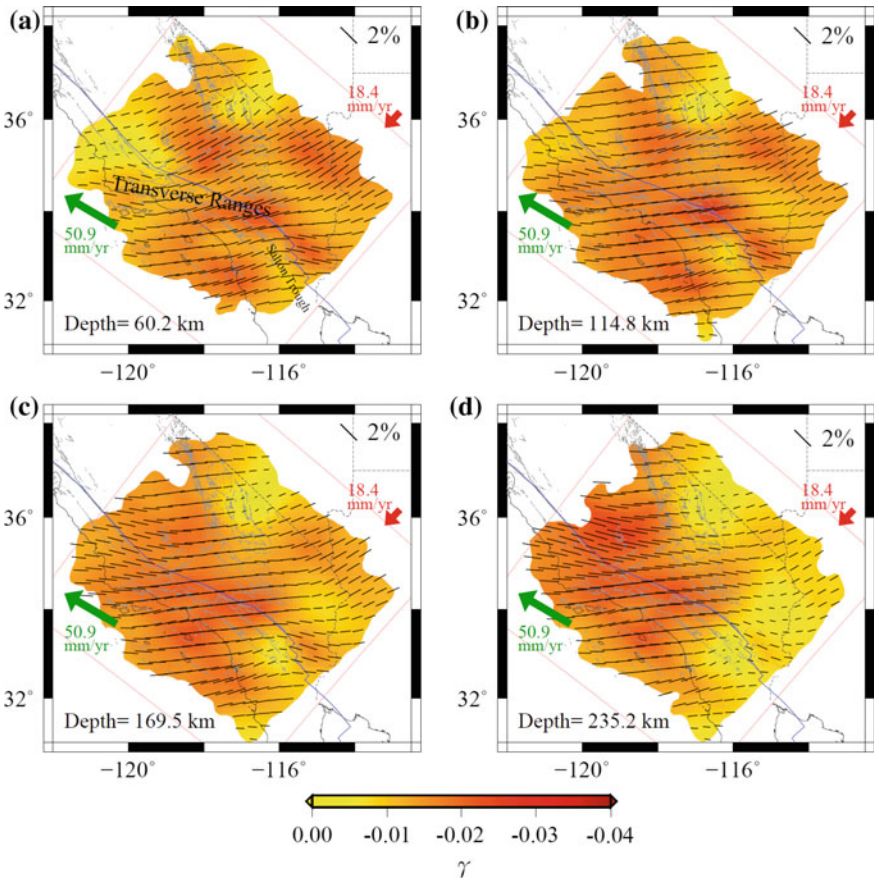

Fig. 5.10 3D anisotropy model for Southern California at the depths of **a** 60.2 km, **b** 114.8 km, **c** 169.5 km and **d** 235.2 km. The *background colors* indicate the strength of the shear-wave anisotropy γ, whereas the *black bars* depict the directions of the fast axes at every two nodes and their lengths are proportional to the anisotropy strength. The absolute plate motions (APM) of the Pacific and North America plates, marked respectively by the green and *red arrows* with the lengths proportional to the rates of motion, are calculated by the model NNR-MORVEL56 (Argus et al. 2011). The plate boundary and fault branches of the SAF system are shown in the *blue* and *gray lines*, respectively. Reprinted from Lin et al. (2014b) with permission Geophysical Research Letters

lithosphere our model has a weaker anisotropy in contrast to the strongest in their result. This discrepancy may be explained by the characteristic difference in the sensitivity kernels used for the two studies. In Monteiller and Chevrot (2011) the kernels calculated in a homogeneous background model have sensitivities close to zero near the surface and increasing with depth. However, Lin et al. (2014a) demonstrated that the near-field and multiple reflections between crustal discontinuities drastically change the pattern of the sensitivity, which can be very large

around the discontinuities and within the crust. The stronger sensitivities in our full-wave approach thus lead to the weaker strength of the anisotropy at shallower depth. Yuan et al. (2011) utilized the joint inversion of surface waves and station-averaged apparent splitting data to obtain a 3D azimuthal anisotropic model of the North American upper mantle. Their result exhibits comparable patterns to our model, with the fast axes oriented E-W around the plate boundary and rotated to NE-SW beneath the NAP above 150-km depth. Another anisotropic model for western United States obtained by surface wave Eikonal tomography (Lin et al. 2011) also shows the E-W fast axis in the uppermost mantle beneath Southern California. In comparison to those models predominantly relying on surface wave information, our inversion of non-averaged individual SKS splitting data yields similar long-wavelength features, and at the same time reveals regional details of the anisotropic structure with higher lateral resolution.

5.5 Conclusion

The 3D seismic anisotropic model provides the pattern of spatial variation in the strength and fast-axis orientation of elastic anisotropy, a useful probe to infer the state of the stress and strain in the lithosphere and the dynamics of the asthenospheric mantle flow for further understanding of the strength and deformation in the upper mantle beneath the SAF system. In this regional-scale anisotropy tomography study, we have employed the state-of-the-art approach to preserve both the inversion efficiency and accuracy of the resolved anisotropic structure. The full-wave derivation of the 3D sensitivity kernels for individual splitting data takes into account all the interactions between SKS and other interfering phases for a wider range of source-receiver geometry. The multiscale inversion through a hierarchical wavelet-based spatial parameterization of the model achieves naturally data-adaptive spatial resolutions. We have also made a more complete appraisal of the inversion result by estimating the spatial resolution lengths using the computationally efficient statistical resolution matrix method. The resolution length of 25–50 km achievable in our 3D anisotropy model for Southern California provides reliable images revealing detailed variations of the strength and fast-axis orientation of anisotropy. Locally small-scale anisotropic fabrics may be associated with surface geologic features, for instance, the possible upwelling beneath the Salton Trough and the ongoing orogeny in the Transverse Ranges. The more or less consistent patterns of anisotropy over different depths in our model do not support the notion that the lithosphere is decoupled from the underlying mechanically weaker asthenosphere under Southern California. The longer-wavelength anisotropic structure suggests that the fast axes in both the PP and NAP are aligned with the absolute plate motion, whereas in the vicinity of the major plate boundary or the SAF system the anisotropy tends to be affected by the motion of both plates.

References

An M (2012) A simple method for determining the spatial resolution of a general inverse problem. Geophys J Int 191:849–864

Argus DF, Gordon RG, DeMets C (2011) Geologically current motion of 56 plates relative to the no-net-rotation reference frame. Geochem, Geophys, Geosyst 12:Q11001. doi:10.1029/2011GC003751

Babuška V, Cara M (1991) Seismic Anisotropy in the Earth. Kluwer Academic Publishers, The Netherlands

Becker TW, Chevrot S, Schulte-Pelkum V, Blackman DK (2006) Statistical properties of seismic anisotropy predicted by upper mantle geodynamic models. J Geophys Res 111:B08309. doi:10.1029/2005JB004095

Browaeys J, Chevrot S (2004) Decomposition of the elastic tensor and geophysical applications. Geophys J Int 159:667–678

Chen P, Zhao L, Jordan TH (2007) Full 3D Tomography for the crustal structure of the Los Angeles region. Bull seism Soc Am 97:1094–1120

Chevrot S (2000) Multichannel analysis of shear wave splitting. J Geophys Res 105:21579–21590

Chevrot S (2006) Finite frequency vectorial tomography: a new method for high resolution imaging of upper mantle anisotropy. Geophys J Int 165:641–657

Chiao L-Y, Chen Y-N, Gung Y-C (2014) Constructing empirical resolution diagnostics for kriging and minimum curvature gridding. J Geophys Res 119:3939–3954. doi:10.1002/2013JB0010364

Chiao L-Y, Fang H-Y, Gung Y-C, Chang Y-H, Hung S-H (2010) Comparative appraisal of linear inverse models constructed via distinctive parameterizations (comparing distinctly inverted models). J Geophys Res 115:B07305. doi:10.1029/2009JB006867

Chiao L-Y, Kuo B-Y (2001) Multiscale seismic tomography. Geophys J Int 145:517–527. doi:10.1046/j.0956-540x.2001.01403.x

Chiao L-Y, Liang W-Z (2003) Multiresolution parameterization for geophysical inverse problems. Geophysics 68:199–209. doi:10.1190/1.1543207

Dziewonski AM, Anderson DL (1981) Preliminary reference Earth model. Phys Earth Planet Int 25:297–356

Favier N, Chevrot S (2003) Sensitivity kernels for shear wave splitting in transverse isotropic media. Geophys J Int 153:213–228

Favier N, Chevrot S, Komatitsch D (2004) Near-field influences on shear wave splitting and traveltime sensitivity kernels. Geophys J Int 156:467–482

Fay NP, Bennett RA, Spinler JC, Humphreys ED (2008) Small-scale upper mantle convection and crustal dynamics in southern California. Geochem, Geophys, Geosyst 9:Q08006. doi:10.1029/2008GC001988

Ford Heather A, Fischer KM, Lekic V (2014) Localized shear in the deep lithosphere beneath the San Andreas fault system. Geology 42:295–298. doi:10.1130/G35128.1

Humphreys ED, Clayton RW (1990) Tomographic image of the southern California mantle J Geophys Res 95:19,725–19,746

Hung S-H, Chen W-P, Chiao L-Y (2011) A data-adaptive, multiscale approach of finite-frequency traveltime tomography with special reference to P and S wave data from central Tibet. J Geophys Res 116, B06307. doi: 10.1029/2010JB008190

Kohler MD, Magistrale H, Clayton RW (2003) Mantle heterogeneities and the SCEC reference three-dimensional Seismic Velocity Model Version 3. Bull seism Soc Am 93:757–774

Kosarian M, Davis PM, Tanimoto T, Clayton RW (2011) The relationship between upper mantle anisotropic structures beneath California, transpression, and absolute plate motions. J Geophys Res 116:B08307. doi:10.1029/2010JB007742

Lee E-J, Chen P, Jordan TH, Maechling PB, Denolle MAM, Beroza GC (2014) Full-3-D tomography for crustal structure in Southern California based on the scattering-integral and the

adjoint-wave field methods. J Geophys Res Solid Earth 119:6421–6451. doi: 10.1002/2014JB011346

Lin F-C, Ritzwoller MH, Yang Y, Moschetti MP, Fouch MJ (2011) Complex and variable crustal and uppermost mantle seismic anisotropy in the western United States. Nat Geosci 4:55–61

Lin Y-P, Zhao L, Hung S-H (2014a) Full-wave effects on shear wave splitting. Geophys Res Lett 41:799–804. doi: 10.1002/2013GL058742

Lin Y-P, Zhao L, Hung S-H (2014b) Full-wave multiscale anisotropy tomography in Southern California. Geophys Res Lett 41. doi: 10.1002/2014GL061855

Mensch T, Rasolofosaon P (1997) Elastic-wave velocities in anisotropic media of arbitrary symmetry-generalization of Thomsen's parameters ε, δ and γ. Geophys J Int 128:43–64. doi:10.1111/j.1365-246X.1997.tb04070.x

Molnar P, Dayem KE (2010) Major intracontinental strike-slip faults and contrasts in lithospheric strength. Geosphere 6:444–467

Monteiller V, Chevrot S (2011) High-resolution imaging of the deep anisotropic structure of the San Andreas Fault system beneath southern California. Geophys J Int 186:418–446

Paige CC, Saunders MA (1982a) Algorithm 583, LSQR: sparse linear equations and least squares problems. ACM Trans Math Softw 8(2):195–209

Paige CC, Saunders MA (1982b) LSQR: an algorithm for sparse linear equations and sparse least squares. ACM Trans Math Softw 8(2):43–71

Plesch A, Shaw JH, Benson C (2007) Community Fault Model (CFM) for Southern California. Bull seism Soc Am 97:1793–1802

Polet J, Kanamori H (1997) Upper-mantle shear velocities beneath Southern California determined from Long-period surface waves. Bull seism Soc Am 87:200–209

Press F (1956) Determination of crustal structure from phase velocity of Rayleigh waves part I: southern California. Bull Geol Soc Am 67:1647

Shapiro NM, Campillo M, Stehly L, Ritzwoller MH (2005) High-resolution surface-wave tomography from ambient seismic noise. Science 307:16151618

Silver PG, Holt WE (2002) The mantle flow field beneath Western North America. Science 295:1054–1057

Tanimoto T, Prindle K (2002) Three-dimensional S-wave velocity structure in Southern California. Geophys Res Lett 29(8):1–4. doi:1029/2001GL013486

Tape C, Liu Q, Maggi A, Tromp J (2009) Adjoint tomography of the Southern California crust. Science 325:988–991. doi:10.1126/science.1175298

Yang Y, Forsyth DW (2006) Rayleigh wave phase velocities, small-scale convection, and azimuthal anisotropy beneath southern California. J Geophys Res 111:B07306. doi:10.1029/2005JB004180

Yang Y, Ritzwoller MH, Lin F-C, Moschetti MP, Shapiro NM (2008) Structure of the crust and uppermost mantle beneath the western United States revealed by ambient noise and earthquake tomography. J Geophys Res 113:B12310. doi:10.1029/2008JB005833

Yuan H, Romanowicz B (2010) Depth dependent azimuthal anisotropy in the western US upper mantle. Earth planet Sci Lett 300:385–394. doi:10.1016/j.epsl.2010.10.020

Yuan H, Romanowicz B, Fischer KM, Abt D (2011) 3-D shear wave radially and azimuthally anisotropic velocity model of the North American upper mantle. Geophys J Int 184:1237–1260

Zhao L, Chevrot S (2011a) An efficient and flexible approach to the calculation of three-dimensional full-wave Fréchet kernels for seismic tomography: I-Theory. Geophys J Int 185:922–938

Zhao L, Chevrot S (2011b) An efficient and flexible approach to the calculation of three-dimensional full-wave Fréchet kernels for seismic tomography: II–Numerical results. Geophys J Int 185:939–954

Chapter 6
Concluding Remarks

In this dissertation, we conducted investigations on the Earth's seismic structure using both active-source and natural earthquake records. In studying the isotropic P-wave velocity structure of Taiwan, the ground-truth dataset of P-wave travel times from the active-source experiment in the TAiwan Integrated GEodynamics Research (TAIGER) project provides the most reliable criterion against which all tomography models in the Taiwan region can and should be tested. Comparisons of the differences between the observed and model-predicted first-arrival times demonstrate that the 3D tomography models R95 (Rau and Wu 1995), K05 (Kim et al. 2005) and W07 (Wu et al. 2007) all yield smaller travel time residuals than the 1D model and overall correct distributions of high and low wave-speed regions, but actually underestimate the amplitudes of lateral velocity heterogeneities which leaves plenty of rooms for further improvement in the 3D structural images beneath Taiwan. Statistical analysis of the residuals calculated by subtracting the model-predicted first-arrival times from the observed ones shows that the 3D model W07 provides the best fit to the ground-truth travel times. The velocity structures resolved in Model K05 are on average biased to be too slow, but provide potentially the best fit to the observed first-arrival times in the western foothills and coastal plain regions.

With the advancement in computational technology as well as in numerical algorithms for modelling seismic wave propagation, more regional and global tomography models will be produced. There is clearly a need for objective and reliable approach to evaluate the efficacy of the increasing number of tomography models. In this study, we have only analyzed the first-arrival times from the TAIGER explosion records, which represents the most accurate ground-truth dataset for this purpose. However, the active-source records undoubtedly possess additional waveforms of both body and surface waves that contain much more information which can be exploited in future efforts of tomography model assessments as well as Earth structural investigations.

The ground-truth data obtained from the TAIGER active-source experiments provide excellent and unique constraints on shallow crustal structures beneath Taiwan. We used them to derive 2D seismic profiles along four transects across the

Y.-P. Lin, *Isotropic and Anisotropic Seismic Tomography Using Active Source and Earthquake Records*, Springer Theses, DOI 10.1007/978-981-10-5068-8_6

island of Taiwan and 22 shorter profiles in northern Taiwan using forward modelling and maximizing the fit to these highly accurate first-arrival times. The resulting seismic structures along these 2D profiles display clear lateral variations with more realistic amplitudes of velocity perturbation and a spatial pattern consistent with geological zonations of Taiwan. The profiles across northern Taiwan shows strong lateral velocity contrast of nearly $\pm 30\%$ between the western tablelands and eastern ranges, also in good agreement with the near-surface geologic expressions. Taking advantage of the densely-distributed crisscrossing 2D velocity profiles in northern Taiwan, we construct a smooth and robust 3D model with sufficient resolution based on the partition modelling approach. The velocity anomalies in the resulting partitioned modelling 3D model (PM3D) exhibit remarkable consistency with the geological features at the surface. An important utility of our 3D model PM3D is to serve as a more effective starting model is a high-resolution regularized multiscale tomography inversion using either active- or passive-source observations or both.

In contrast to the ray-theory treatment of the high-frequency first-arrival times from active-source records, we adopted the full-wave approach in analyzing the shear-wave splitting measurements to study the anisotropic structure of Southern California. The full-wave effects are neglected in conventional practices of shear-wave splitting analysis which explicitly assumes that the observed SKS or SKKS phase is composed of a single vertically incident plane wave. However, the interference of SKS with other phases of similar arrival times, the near-field effect, and the multiple reflections in the crust can lead to strong dependence of the splitting intensity on the epicentral distance. The full-wave sensitivity kernels account for the effects of all possible wave interferences involved in shear-wave splitting and therefore loosen the restrictions on source-receiver geometry amenable to shear-wave splitting analysis. The 3D Fréchet kernels, moreover, enable us to resolve the vertical and lateral variations in seismic anisotropy and obtain 3D images of the Earth's anisotropic structure. We then practice our full-wave kernels to probe the anisotropy beneath the Southern California which affords us to infer the state of the stress and strain in the lithosphere and the dynamics of the asthenospheric mantle flow for further understanding of the strength and deformation in the upper mantle beneath the SAF system. The multiscale inversion through a wavelet-based spatial model parameterization achieves naturally data-adaptive spatial resolutions. We have also made a more complete appraisal of the inversion result by estimating the spatial resolution lengths using the statistical resolution method without any matrix operation. The resolution length of 25–50 km achievable in our 3D anisotropy model for Southern California provides reliable images revealing detailed variations of the strength and fast-axis orientation of anisotropy. Locally small-scale fast directions may be correlated with surface geologic features, for instance, the possible upwelling beneath the Salton Trough and the ongoing orogeny in the Transverse Ranges. The most consistent patterns of anisotropy over different depths in our model do not support the notion that the lithosphere is decoupled from the asthenosphere in this region. The longer-wavelength anisotropic structure suggests that the fast axes in both the Pacific Plate (PP) and North

American Plate (NAP) are aligned with the absolute plate motion, whereas in the vicinity of the major plate boundary the anisotropy tends to be affected by the motion of both plates. Our approach represents an early step in imaging the detailed 3D variation of anisotropy. Further developments are needed to adopt numerical wavefield modelling tools such as the spectral-element method (e.g. Sieminski et al. 2007) so that more complex 3D reference models can be used and anisotropic models can be iteratively updated.

References

Kim KH, Chiu JM, Pujol J, Chen K-C, Huang B-S, Yeh Y-H, Shen P (2005) Three-dimensional *Vp* and *Vs* structural model associated with the active subduction and collision tectonics in the Taiwan region. Geophys J Int 162:204–220

Rau R-J, Wu FT (1995) Tomographic imaging of lithospheric structures under Taiwan. Earth Planet Sci Lett 133:517–532

Sieminski A, Liu Q, Trampert J, Tromp J (2007) Finite-frequency sensitivity of body waves to anisotropy based upon adjoint methods. Geophys J Int 171:368–389

Wu Y-M, Chang C-H, Zhao L, Shyu JBH, Chen Y-G, Sieh K, Avouac J-P (2007) Seismic tomography of Taiwan: improved constraints from a dense network of strong motion stations. J Geophys Res 112:B08312. doi:10.1029/2007JB004983